Dynamic global vegetation model: The variability in terrestrial carbon storage over the last 500 years

Diplomarbeit

der Philosophisch–naturwissenschaftlichen Fakultät
der Universität Bern

vorgelegt von
Philippe Brügger
2000

Leiter der Arbeit:
Prof. Dr. T. Stocker, PD. Dr. F. Joos

Abteilung für Klima– und Umweltphysik
Physikalisches Institut der Universität Bern

Everything should be made as simple as possible,
but not simpler.

Albert Einstein, 1879–1955

Contents

1 Introduction **7**

2 LPJ-DGVM **9**

2.1 Vegetation 9

2.1.1 Plant functional types 9

2.1.2 Bioclimatic limits 12

2.1.3 Vegetation distribution 13

2.2 Hydrology 16

2.3 Carbon pools and fluxes 18

2.4 Photosynthesis 21

2.5 Fire 23

2.6 Model spinup and input data 24

3 Model sensitivity analyses **29**

3.1 CO_2 variations 29

3.1.1 Plant functional types 34

3.1.2 Grid cell analyses 39

3.2 Temperature variations 44

3.2.1 Changes in seasonality 55

3.3 Precipitation variations 59

4 Terrestrial carbon storage over the last 500 years **65**

4.1 Data 66

4.1.1 CO_2 data 66

4.1.2 Temperature data 68

4.2 Results 77
4.2.1 Simulations with varying CO_2 77
4.2.2 Simulations with varying temperatures 79
4.2.3 Simulations with varying CO_2 and temperatures 82

5 Conclusions and discussion **87**
5.1 Model sensitivity analyses 87
5.2 "Little ice age" hypothesis 88

6 Acknowledgments **91**

A Major world biomes **93**

B Empirical orthogonal function analysis **95**

C Cubic smoothing splines **97**

Tables **99**

Figures **103**

Bibliography **105**

Chapter 1

Introduction

The terrestrial biosphere plays an active role in shaping the environmental system of the Earth. In particular, terrestrial vegetation and soils are essential in determining the state of the global climate system and the carbon cycle. Therefore, it is essential that we improve our understanding of the terrestrial biosphere in terms of the interactive role biospheric processes play in the functioning of the Earth system as a whole.

A large number of numerical models have been developed in the last decade in an attempt to examine global biospheric processes. Those models can be divided into the following classes: *Land surface models*, coupled to atmospheric general circulation models, to simulate interactions between land surface and the atmosphere (neglecting potential changes in vegetation cover), *equilibrium vegetation models* examining the geographic distribution of vegetation communities and their relationship to climate, and *terrestrial biogeochemistry models* representing the carbon cycle and fluxes of mineral nutrients [*Foley and Prentice*, 1996]. An important limitation of those model types is that they assume the terrestrial ecosystems to be time-independent. But because vegetation and soils are essential in determining the state of the global climate system and the carbon cycle, it is important to be able to simulate vegetation dynamics. Dynamic vegetation models have been developed in order to examine the transient response of terrestrial ecosystems to variations in climate and increasing atmospheric CO_2 concentrations in the last few years.

With the Lund-Potsdam-Jena dynamic global vegetation model (LPJ-DGVM) [*Sitch et al.*, 2000], we especially examine the terrestrial carbon uptake over the last 500 years. Law Dome records of atmospheric CO_2 concentrations reconstructed from air bubbles entrapped in ice cores show that the level of CO_2 decreased around 1550 A.D., and stayed low until about 1850. This period around the time of reported low temperatures in Europe is often referred to as "little ice age" (LIA) [*Grove*, 1988].

Increased $\delta^{13}C$ values during the seventeenth and eighteenth centuries [*Trudinger et al.*, 1999] indicate that the relatively low atmospheric CO_2 level during this time period was caused by an enhanced terrestrial storage. By solving the atmospheric budget equations for CO_2 and $\delta^{13}C$ for the unknown global fluxes into the terrestrial biosphere, the additional terrestrial storage is assumed to be 40 GtC [*Joos et al.*, 1999].

The major purpose of this study is to examine the hypothesis that the relatively low atmospheric CO_2 level during this time period was caused by an enhanced terrestrial storage using the LPJ-DGVM.

In chapter 2, the basic concepts of the LPJ-DGVM are explained. Our explanations are concentrated on the simulation of vegetation dynamics, hydrology, carbon fluxes and pools, and the calculation of photosynthesis and fire events. Additionally, a description of the model spinup and of input data is presented.

Detailed model sensitivity studies are performed in chapter 3. Changes in terrestrial carbon storage and in vegetation distribution resulting from step-like perturbations in atmospheric CO_2 concentrations, air temperatures, and precipitation are analyzed.

Chapter 4 is the main part of this thesis. The terrestrial carbon uptake between 1550 and 1850 A.D. is examined by forcing the LPJ model with atmospheric CO_2 data by (*Etheridge et al.* [1996], *Barnola et al.* [1995], *Neftel et al.* [1982], *Neftel et al.* [1994], *Siegenthaler et al.* [1988]) and reconstructed temperature anomalies by *Mann et al.* [1998].

The major results of the sensitivity simulations and the analyzes of the terrestrial carbon storage over the last 500 years are recapitulated and discussed in chapter 5.

Chapter 2

The Lund-Potsdam-Jena dynamic global vegetation model

In this chapter, the basic concepts of the Lund-Potsdam-Jena dynamic global vegetation model (LPJ-DGVM) developed by *Sitch et al.* [2000] are explained. The model is built in a modular framework simulating vegetation dynamics, hydrology, and soil organic matter dynamics on an area-averaged grid cell basis with a resolution of 2.5×3.75 degrees. This implies a field of 1631 grid elements over the land area of the world.

2.1 Vegetation

A non trivial task is to define an optimal set of plant functional types (PFTs) which best represents the enormous variety in distribution and functioning of plants around the world. The exact choice of PFTs is somewhat subjective reflecting the level of model complexity, itself governed by the temporal and spatial resolution of the study and those structural features and processes deemed to be essential in correctly modeling vegetation and population dynamics. In this section, the nine plant functional types differentiated in the LPJ-DGVM, their bioclimatic limits, and the geographical distribution of major world biomes are explained.

2.1.1 Plant functional types

The nine plant functional types distinguished in the LPJ model are differentiated by physiological, morphological, and phenological attributes. Trees in tropical regions are distinguished according to their seasonalities into evergreen and raingreen plants. Temperate plants are divided into needleleaved and broadleaved types, whereas there

are evergreen and summergreen broadleaved trees. The remaining two types of trees are situated in boreal regions. In the model, summergreen plants and evergreen conifers are distinguished. In addition to those seven tree types, two kinds of grasses are subdivided according to their photosynthetic pathway, C_3 and C_4 respectively (see section 2.4).

Evergreen PFTs maintain a constant leaf coverage over the year, and are assigned leaf turnover times τ_l greater than one year (see table 2.1). Plants with a summergreen phenology begin leaf growth when daily temperature T_d exceeds 5° C, following the approach of *Haxeltine and Prentice* [1996]. Daily phenology is calculated from the current accumulated growing degree days GDD_5 (equation 2.3) divided by the PFT specific value $GDD_{5,ind}$ (see table 2.2), with a maximum value equal to one. Maximum leaf coverage for raingreen plants is maintained whilst the specific water stress factor W_{min} remains equal or above a threshold of 35% (section 2.1.2). Grasses behave as evergreen plants under ideal conditions, and they can adopt a raingreen or summergreen phenology respectively under water or temperature limited conditions.

PFT	f_r	$g_{p,min}$	α_f	τ_l	τ_s	τ_r	$T_{CO_2,min}$	$T_{CO_2,max}$	$T_{P,min}$	$T_{P,max}$
	[%]	[mm/s]	[1]	[1/yr]	[1/yr]	[1/yr]	[° C]	[° C]	[° C]	[° C]
(a)	85	0.5	0.12	2	20	2	2	55	25	30
(b)	70	0.5	0.50	1	20	1	2	55	25	30
(c)	70	0.3	0.12	2	20	2	-4	42	20	30
(d)	70	0.5	0.50	1	20	1	-4	38	20	30
(e)	80	0.5	0.12	1	20	1	-4	38	20	25
(f)	90	0.3	0.12	2	20	2	-4	38	15	25
(g)	90	0.3	0.12	1	20	1	-4	38	15	25
(h)	90	0.5	1	1	1	2	-4	45	10	30
(i)	90	0.5	1	1	1	2	6	55	20	45

Table 2.1: PFT specific parameters. (a) are tropical broadleaved evergreen trees, (b) tropical broadleaved raingreen trees, (c) temperate needleleaved evergreen trees, (d) temperate broadleaved evergreen trees, (e) temperate broadleaved summergreen trees, (f) boreal needleleaved evergreen trees, (g) boreal summergreen trees, (h) cool grass (C_3), and (i) warm grass (C_4). f_r is the fraction of roots in the upper soil layer, $g_{p,min}$ the minimal canopy conductance component for water not associated with photosynthesis, α_f the fire resistance index, τ_l the leaf turnover period, τ_s the sapwood turnover period (sapwood converting to heartwood), τ_r the root turnover period, $T_{CO_2,min}$ and $T_{CO_2,max}$ the low and high temperature limit for CO_2 uptake respectively, and $T_{P,min}$ and $T_{P,max}$ the lower and upper range of temperature optimum for photosynthesis.

An important factor in order to deal with vegetation dynamics is to know the proportion of the different PFTs within a grid cell. The appropriate measure is the individual foliar projective cover (FPC_{ind}), the area of ground covered by foliage

directly above it. The grid cell PFT fractional coverage FPC_{grid} is calculated as follows:

$$FPC_{grid} = A_{c,ind} \cdot \rho_{ind} \cdot FPC_{ind} \tag{2.1}$$

where $A_{c,ind}$ is the individual crown area (m^2), and ρ_{ind} the PFT density ($1/m^2$).

Grid cell properties are recalculated on an annual time step. The sum of all grid cell FPCs is constrained to a value of one. If it exceeds this limit, woody PFTs are favored over grass due to their advantage in light competition. Owing to the effect of self thinning, the number of PFT individuals is reduced if the total fractional coverage of woody vegetation exceeds 0.95. Additional mortality is calculated based on vegetation growth efficiency, heat stress, negative production, and depending on whether the climate lies within the appropriate bioclimatic limits (section 2.1.2).

The establishment of new plants is performed annually by the LPJ-DGVM. The fraction of the grid cell available for new woody establishment is the proportion of the area not currently occupied by trees, representing the illuminated understory. Grasses can only establish in such areas. Development of seedlings and saplings are not explicitly modeled through the course of the year. The additional carbon associated with sapling establishment is therefore simply added to the annual NPP, maintaining a closed carbon cycle. A major simplification in the model with the average individual concept is that only one age-height class for each woody PFT is defined. By updating average individual properties, the saplings in effect become average individuals, surpassing potentially critical stages in their life cycle.

The average PFT individual is the smallest vegetation unit. It is defined in terms of its crown area, the height, and four tissue pools: leaves, sapwood, heartwood, and fine roots. Height h_{ind} and crown area c_{ind} of a plant are related to the appropriate stem diameter sd_{ind} based on the following relationships:

$$\begin{aligned} h_{ind} &= \alpha_1 \cdot {sd_{ind}}^{\alpha_2} \\ c_{ind} &= \alpha_1 \cdot {sd_{ind}}^{\alpha_3} \end{aligned} \tag{2.2}$$

with the parameters $\alpha_1 = 40$, $\alpha_2 = 0.5$, and $\alpha_3 = 0.3$. The stem diameter is calculated as a function of the PFT specific heartwood and sapwood mass in units gC and the wood density in units gC/m^3. Sapwood lies in the outer part of the stem, between the inner bark and the heartwood, containing living cells and reserve materials. Sapwood conducts and stores water and nutrients, whereas the dead inner core of the stem, called heartwood, is responsible for the plant structure and for the storage of waste products.

2.1.2 Bioclimatic limits

To determine which PFT may potentially exist within each grid cell, the model applies a set of climatic constraints (table 2.2). If the average temperature of the coldest month of the year falls below a PFT specific threshold $T_{c,min}$, the PFT individual can not survive. If the average temperature of the coldest or warmest month exceeds $T_{c,max}$ or $T_{w,max}$ respectively, plants survive but are unable to regenerate. In addition to those temperature limits, vegetation requires a sufficiently long growing season. A measure of this constraint is the amount of minimum growing degree days GDD_5, defined as

$$GDD_5 = \sum_{d=1}^{365} (T_d - 5) \tag{2.3}$$

for days where the mean temperature T_d is greater than 5° C. An additional constraint for certain PFTs is the water stress factor W, given as the ratio of the supply and potential demand functions (equation 2.7 on page 17). The water stress factor has to be equal or above the PFT specific minimal water scalar W_{min} for successful sapling regeneration. The consequence of this is that raingreen plants are able to shed their leaves in order to reduce water respiration if W is lower than 35%, which makes them able to survive under drought conditions for a certain time period. In contrast to this, evergreen trees are specialized for non-water-stressed conditions.

PFT	$T_{c,min}$ [° C]	$T_{c,max}$ [° C]	$T_{w,min}$ [° C]	$GDD_{5,ind}$ [° C]	W_{min} [%]
tropical broadleaved evergreen	15.5				
tropical broadleaved raingreen	15.5				35
temperate needleleaved evergreen	-2.0	22.0		900.0	
temperate broadleaved evergreen	3.0	18.8		1200.0	
temperate broadleaved summergreen	-17.0	15.5		1200.0	
boreal needleleaved evergreen	-32.5	-2.0	23.0	600.0	
boreal summergreen		-2.0	23.0	350.0	
cool grass (C_3)		15.5			35
warm grass (C_4)	15.5				35

Table 2.2: PFT bioclimatic limits: $T_{c,min}$ is the minimal, $T_{c,max}$ the maximal temperature of the coldest month, $T_{w,min}$ the minimal temperature of the warmest month, $GDD_{5,ind}$ is the individual minimum growing degree days, and W_{min} is the water scalar at which leaves shed. Missing values signify that there is no appropriate limitation in the LPJ model.

2.1.3 Vegetation distribution

In order to examine whether the potential PFT distribution calculated by LPJ-DGVM is realistic, it is compared with a vegetation map derived from satellite data (figure 2.1). A major problem in comparing those vegetation patterns is that the model distinguishes different plant types, whereas the satellite map shows the major world biomes. In addition to this, the LPJ model as used here does not consider land use such as cultivation or deforestation.

The upper map in figure 2.1 shows a cylindrical projection of the world's vegetation distribution as calculated by the LPJ model with the atmospheric carbon dioxide concentration of the year 1987 of approximately 355 ppmv [*Keeling and Whorf*, 1999] in order to be comparable with the satellite map. Only the PFT with the biggest FPC is plotted for each grid cell (whereby bare ground is handled as a PFT as well). This simplification is necessary so as to give a global overview of the vegetation patterns of the world, although some information is lost, especially in biomes with several different PFTs, and in border regions of two vegetation types.

The global vegetation pattern derived from satellite data is plotted as a stereographic projection of the world map (lower part of figure 2.1). This map and a documentation are published in the Internet (*www.geog.umd.edu/landcover/1d-map.html*). The data set was based on advanced very high resolution radiometer (AVHRR) measurements of seasonal changes in vegetative cover as displayed in temporal variations of a spectral vegetation index known as the normalized difference vegetation index (NDVI) [*DeFries and Townshend*, 1994]. This index gives an indication of the photosynthetic activity of the vegetation during the different climatic seasons in order to distinguish different plant types. The NDVI values are the maximum monthly composites for 1987 at approximately 8 km resolution, averaged to a spatial resolution of one by one degree. The eleven vegetation types are defined in terms of their functional characteristics including height of vegetation, percentage of ground surface covered by vegetation, seasonality, and leaf type. Those cover types were selected primarily to conform with the vegetation classes required as input to climate models, and although they are not exactly the same as the PFTs of LPJ-DGVM, those two classifications are similar enough to be reasonably compared.

The first two plant functional types of the LPJ model, tropical broadleaved evergreen and raingreen trees, can directly be compared with broadleaved evergreen trees (A) of *DeFries and Townshend* [1994]. It is obvious that the area covered by tropical PFTs according to the LPJ model is larger than the measured extents. In South America, simulated rainforests almost cover whole Brazil, whereas according to satellite data, wooded grassland is spread over the southern part of the country. In Africa, tropical plants only cover regions between latitudes of about 6° N and 6° S according to measurements, but the model data show a tropical rainforest with

an extent from 12° N to 15° S. Some of these discrepancies may be explained by anthropogenic deforestation, which is not considered by the LPJ-DGVM. Another region of bad correlation caused by the neglected human influence in the simulated vegetation distribution can be found in eastern India, where the LPJ model predicts a tropical rainforest instead of grassland and cultivated crops.

The three simulated temperate PFTs (needleleaved evergreen, broadleaved evergreen, and broadleaved summergreen trees) can be compared to the observed vegetation types (E) and (F) (mixed deciduous and evergreen forest and woodland, and broadleaved deciduous forest and woodland). The tendency in temperate regions is that trees cover a larger area on the LPJ map than according to measurements (southern Brazil and Uruguay, eastern USA, Central Europe, and eastern China). The main reason for this difference is the land use in those areas.

If we examine the boreal vegetation types (6), (7), (B), and (C), we also determine a tendency of overestimated extents. Simulated geographical patterns of conifers are quite realistic, but distinctions can be found in Mongolia and northern China, where grasses are measured to be dominating due to cultivation. Deciduous trees generally cover bigger parts of Russia according to the LPJ-DGVM than in reality, and in northern Canada, large tundra areas are predicted to be boreal forests.

The comparison between the diverse grass types is more difficult than between woody PFTs, because grasses are distinguished considering different properties in the two maps. The LPJ model divides them according to their photosynthetic pathway, C_3 and C_4 respectively, into so called cool and warm grass (see section 2.4 for a description of photosynthesis). In the classification of *DeFries and Townshend* [1994], three different grass types are distinguished, namely tundra (D), wooded grassland (G), and grassland (H). In this definition, tundra only consists of grasses, mosses, and lichens, whereas in the grassland biome, up to 10% of the area is covered by broadleaved trees, and even between 10 and 40% in wooded grassland regions. The most significant discrepancy between satellite derived data and LPJ results is the fact that large areas of grassland and tundra such as in the western United States, Greenland, southern Africa, and Australia are predicted not to be vegetated by the LPJ-DGVM. An explanation for this is that according to the biome definitions of *DeFries and Townshend* [1994], tundra and shrublands can be dominated by bare ground. Sparsely distributed plants are neglected in the LPJ map, because only major PFTs are considered, and such areas are plotted as grid cells with bare ground. Another big discrepancy in grass distribution has already been mentioned before: Because of the overestimated extent of tropical rainforests due to the neglected anthropogenic impact, grasslands are mainly supplanted by forests in South America, Africa, and India according to our model simulations.

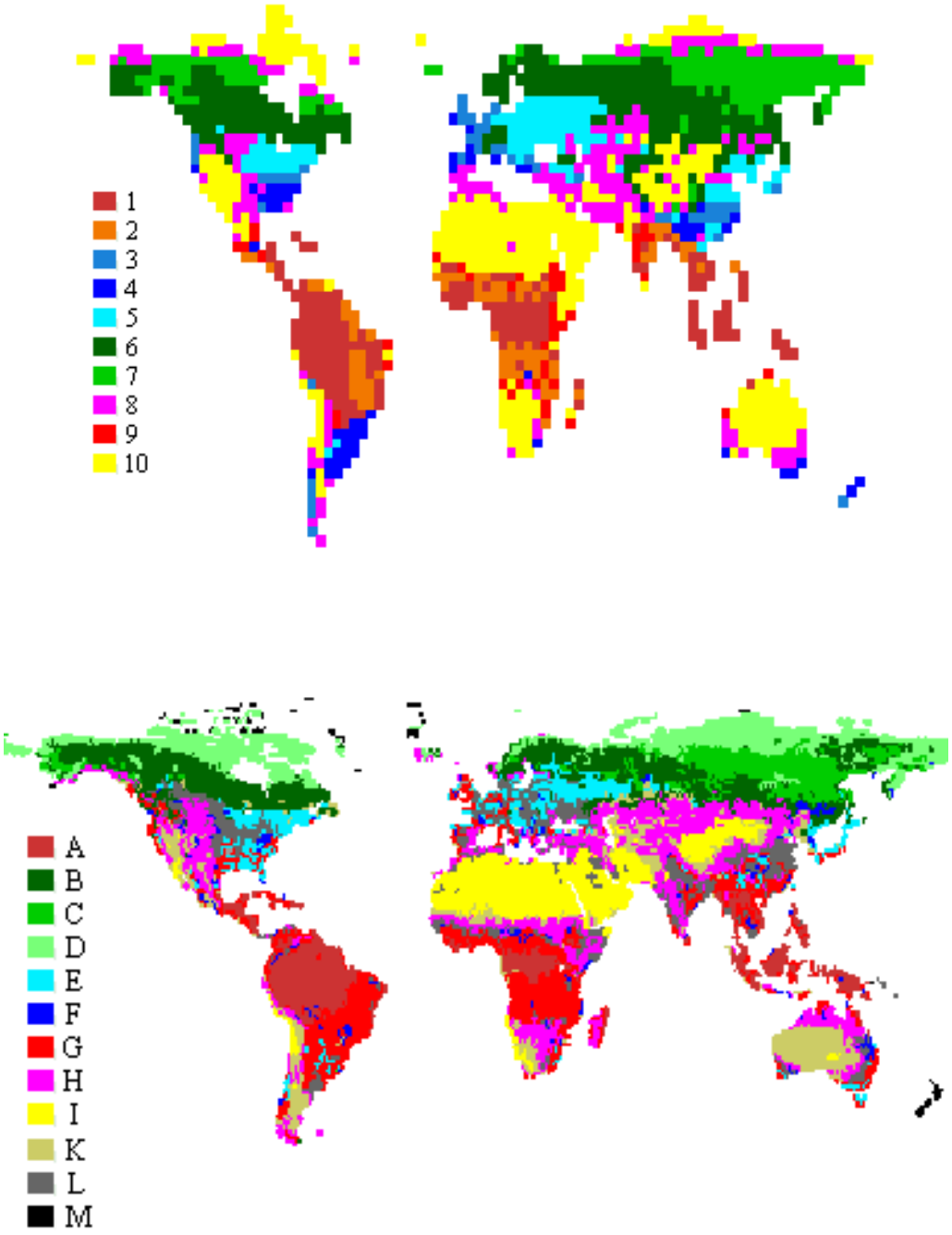

Figure 2.1: Upper map: Major PFT of each grid cell calculated by LPJ with the atmospheric CO_2 concentration of 355 ppmv (1987). Number (1) are tropical broadleaved evergreen trees, (2) tropical broadleaved raingreen trees, (3) temperate needleleaved evergreen trees, (4) temperate broadleaved evergreen trees, (5) temperate broadleaved summergreen trees, (6) boreal needleleaved evergreen trees, (7) boreal summergreen trees, (8) cool grass, (9) warm grass, and (10) bare ground.
Lower map: Vegetation distribution in 1987, reflected in temporal variations of the normalized difference vegetation index (NDVI) derived from satellite data [*DeFries and Townshend*, 1994]. (A) are broadleaved evergreen trees, (B) coniferous evergreen forest and woodland, (C) high latitude deciduous forest and woodland, (D) tundra, (E) mixed deciduous and evergreen forest and woodland, (F) broadleaved deciduous forest and woodland, (G) wooded grassland, (H) grassland, (I) bare ground, (K) shrubs and bare ground, (L) cultivated crops, and (M) are missing data.

Simulated extents of woody plant functional types are generally too large in comparison with the measured vegetation map, because the LPJ model does not consider deforestation and cultivation. In addition, grasses are predicted to be partially ruled out by forests, deserts or ice shields, respectively. It is important to mention again that the LPJ map is colored only according to the plant functional type with the biggest FPC of each grid cell. As we can see in figures 3.5, 3.6, and 3.7 (pages 36ff) showing detailed geographical distributions of the LPJ-DGVM plant types, it is somehow misleading to neglect PFTs with smaller coverages, especially in border regions of plant type areas or in mixed biomes. In Australia for example, the model predicts a significant coverage of cool grass and temperate trees in the southern half of the country, but according to the map in figure 2.1, nearly whole Australia is deserted, because bare ground is still the major PFT. A similar effect can be observed in southern Africa and in the western USA. In general, all borders between different PFTs are shown too sharp on the LPJ-DGVM biome map in figure 2.1, and minor PFTs are neglected.

Summarizing these observations, the major distinctions between calculated potential vegetation patterns and satellite observations can be explained by the neglect of the anthropogenic impact by the model or by the restriction to major PFTs in the LPJ map.

2.2 Hydrology

The soil is divided into two layers, an upper region from 0 to 0.5 m and a lower layer at depth 0.5-1.5 m, following the approach of BIOME 3 [*Haxeltine and Prentice*, 1996]. The soil texture of each grid cell is derived from the FAO (food and agriculture organization of the United Nations) global soil map [*FAO*, 1991], and the texture dependent percolation and water holding capacities are based on the texture classes of *Zobler* [1986]. The actual evapotranspiration AET (mm/day) is calculated as the minimum of a supply function S and a demand function D for each PFT:

$$AET = min\,(S, D) \tag{2.4}$$

S is dependent on the maximum daily transpiration rate possible under well watered conditions, $E_{max} = 5\,\mathrm{mm/day}$, and the soil moisture in the rooting zone, W_r:

$$S = E_{max} W_r \tag{2.5}$$

The daily demand D is calculated as follows:

$$D = E_q \alpha_m \left[1 - exp\left(\frac{-g_{p,ind} L_{d,ind}}{g_m}\right)\right] \tag{2.6}$$

E_q is the potential evapotranspiration rate (mm/day), calculated as a function of the appropriate latitude, the air temperature, and the sunshine hours, $g_{p,ind}$ is the non-water-stressed potential canopy conductance (mm/s), and $L_{d,ind}$ stands for the leaf-on fraction of the actual day. The parameters α_m and g_m are empirical parameters with $\alpha_m = 1.4$ and $g_m = 5\,\mathrm{mm/s}$, following *Monteith* [1995].

The daily water stress factor W is the ratio of the supply and demand functions:

$$W = min\left(\frac{S}{D}, 1\right) \tag{2.7}$$

This is an important value in order to decide whether the water supply is high enough for a specific PFT to grow normally. If the water stress factor W falls below the PFT specific water scalar W_{min}, leaf senescence occurs. In the LPJ model, this is the case for raingreen trees and grasses if W falls below a threshold of 35% (see table 2.2).

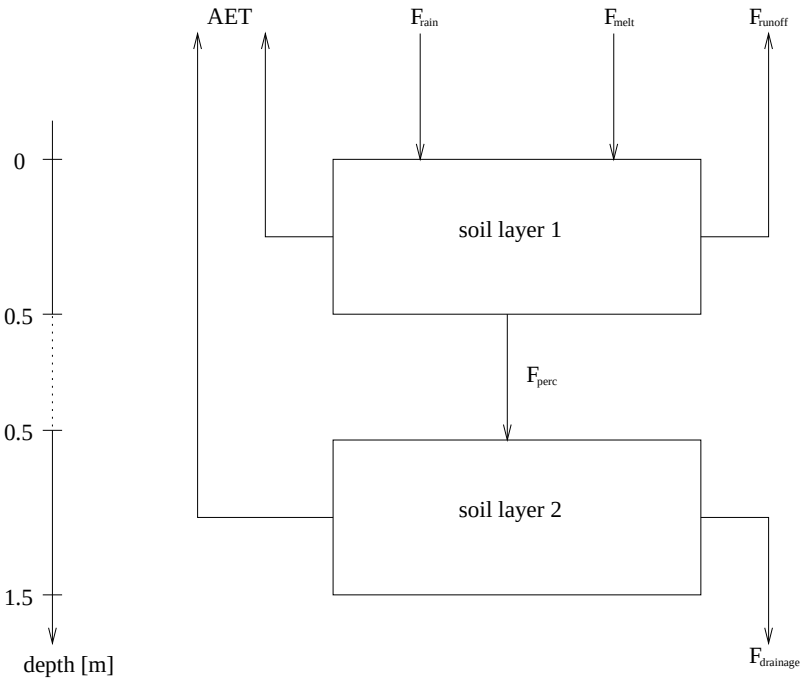

Figure 2.2: Water fluxes between the two soil layers and the atmosphere. *AET* is the actual evapotranspiration, F_{rain} the water flux due to rainfall, F_{melt} the water coming from snow melt, F_{runoff} the surface runoff, F_{perc} the percolation from the upper to the lower soil layer, and $F_{drainage}$ the drainage. All water fluxes are calculated in units mm/yr.

The water contents of both layers are updated daily, and they depend on daily rainfall F_{rain}, snow melt F_{melt}, percolation F_{perc}, and evapotranspiration AET (all

fluxes are calculated in mm/day) as follows:

$$\begin{aligned}
\Delta W_1 &= (F_{rain} + F_{melt} - F_{perc} - \sum_{PFT} \beta_1 AET)/AWC_1 \\
\Delta W_2 &= (F_{Perc} - \sum_{PFT} \beta_2 AET)/AWC_2 \\
\beta_1 &= z \cdot W_1/W_r \\
\beta_2 &= (1-z)\, W_2/W_r \\
W_r &= z \cdot W_1 + (1-z)\, W_2
\end{aligned} \tag{2.8}$$

where W_1 and W_2 are the soil water contents for the previous day (expressed as a fraction of the AWC in that layer), ΔW_1 and ΔW_2 are the daily changes in W_1 and W_2, respectively. AWC_1 and AWC_2 in units mm are the corresponding water holding capacities. They are defined as the difference between field capacity (fractional soil wetness at which water runoff occurs) and wilting point for the relevant soil texture. The parameters β_1 and β_2 give the rates of extraction of transpired water from the upper and lower soil layers, respectively. The PFT specific parameter z defines the fraction of the plant roots which are in the top soil layer [*Jackson and Canadell*, 1996]. W_r is the available soil moisture in the rooting zone.

2.3 Carbon pools and fluxes

The biogeochemistry of the model is based on eight well-mixed boxes for each plant functional type (figure 2.3). The vegetation is divided into four different tissue pools: leaves, sapwood, heartwood and fine roots. The litter is divided into an above-ground and a below-ground compartment, and there are two soil organic matter pools. LPJ simulations start with empty carbon pools, and they are brought to a pre-industrial equilibrium state during the model spinup (see section 2.6). The slow soil organic matter pool with a turnover time of 1000 years at 10° C (see table 2.3) is calculated analytically after 400 years in order to save computation time (see equation 2.18 on page 25).

The carbon input into the vegetation pools comes from the net primary production NPP, which is the carbon that remains stored in a plant after it has taken up CO_2 from the atmosphere and respired some back (autotrophic respiration R_a). Carbon is then transferred to the above-ground litter pool by fallen leaves and to the lower litter pool by dead roots. Rapidly decomposable tissue is respired as CO_2 directly into the atmosphere (about 70% of the carbon in the litter compartments), the remainder is divided between the fast and slow soil organic matter pools. The majority goes into the fast pool (98.5%), while the slow compartment only consists of relatively non-decomposable material such as lignin. Decomposition is dependent

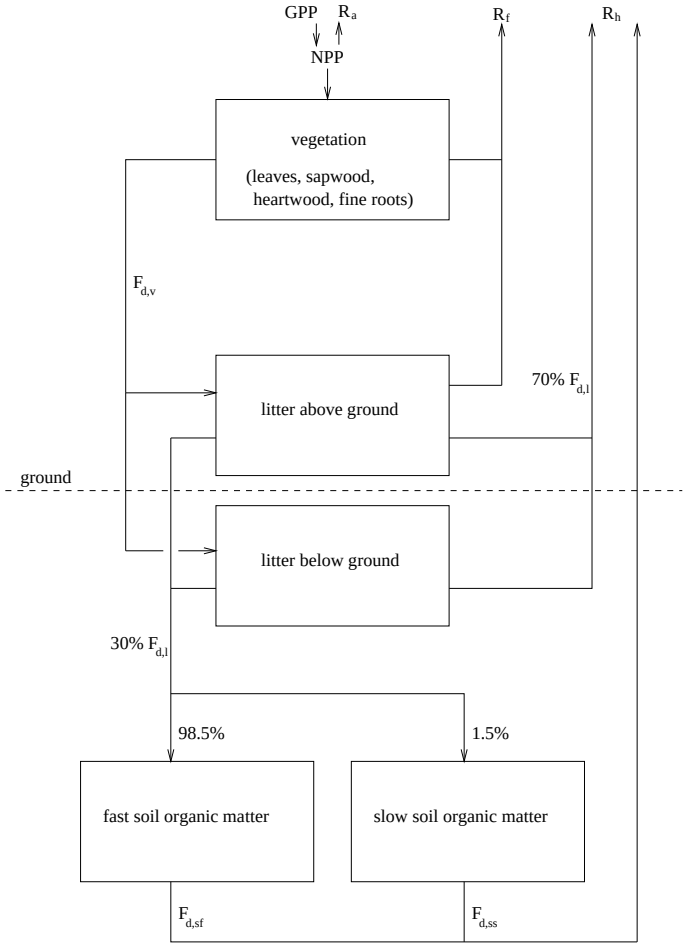

Figure 2.3: Carbon fluxes between model compartments and the atmosphere. GPP is the gross primary production, NPP the net primary production, R_a autotrophic respiration, R_h heterotrophic respiration, R_f is the flux to the atmosphere due to fires, $F_{d,v}$ is the carbon decomposition flux of the vegetation pool, $F_{d,l}$ the decomposition flux of both litter pools, and $F_{d,sf}$ and $F_{d,ss}$ are the carbon fluxes of the fast and slow soil pool, respectively.

upon soil texture, temperature and moisture. Adding the carbon emissions to the atmosphere from the litter pools, the fast and slow soil pools respectively, gives the overall heterotrophic respiration R_h. Fire affects the vegetation and the litter above ground (see section 2.5).

Table 2.3 shows the most important carbon pool properties. Carbon decomposition rates k_{10} of litter and soil pools at 10° C are used according to *Foley* [1995]. In order to take into account that those rates are dependent on temperature and moisture,

monthly decomposition rates k are calculated as follows:

$$\begin{aligned} k &= k_{10} \cdot r_{temp} \cdot r_{moist} \\ r_{temp} &= exp\left(308.56\left(\frac{1}{56.02} - \frac{1}{T_s - 45.87}\right)\right) \\ r_{moist} &= 0.25 + (0.75 \cdot W_1) \end{aligned} \tag{2.9}$$

where r_{temp} is a temperature response function dependent upon soil temperature T_s in units $^\circ$C [*Lloyd and Taylor*, 1994], and r_{moist} a moisture response based on the upper soil layer moisture content W_1 (as a fraction of the water holding capacity) [*Foley*, 1995]. Both response functions are shown in figure 2.4.

Turnover times τ_{10} of litter and soil carbon pools are reciprocal to decomposition rates k_{10}: $\tau_{10} = 1/k_{10}$. Global carbon inventories in the equilibrium after the model spinup are plotted in table 2.3. The vegetation pool contains 869 GtC, 195 GtC can be found in litter pools, whereas the biggest fraction of carbon is in soil pools (1452 GtC). In equilibrium, decomposition fluxes F_d can be calculated from pool inventories C and rates k_{10}:

$$F_d = C \cdot k_{10} \tag{2.10}$$

This equation can also be used to calculate the global mean carbon turnover time of the vegetation pool. If we take into account that $NPP = 68$ GtC/yr and the fire flux $R_f = 6.8$ GtC/yr, the decomposition flux $F_{d,v} = 65$ GtC/yr (assuming that approximately half of R_f is coming from the vegetation). Using equation 2.10, the global mean turnover time of the vegetation pool is approximately 13 years.

carbon pool	k_{10} [1/yr]	τ_{10} [yr]	C_{spinup} [GtC]	F_d [GtC/yr]
vegetation	0.08	13	869	65
litter above ground	0.5	2	113	56.5
litter below ground	0.5	2	82	41
fast soil organic matter	0.03	33.3	1002	30.06
slow soil organic matter	0.001	1000	450	0.45

Table 2.3: Carbon pool properties. k_{10} are carbon decomposition rates at 10° C according to *Foley* [1995], $\tau_{10} = 1/k_{10}$ are the turnover times of the appropriate carbon pools, C_{spinup} are the carbon inventories in the equilibrium after the model spinup, and $F_d = C_{spinup} \cdot k_{10}$ the resulting decomposition fluxes. Decomposition rates and global mean turnover times of the vegetation pool are derived from the appropriate carbon inventory and the decomposition flux.

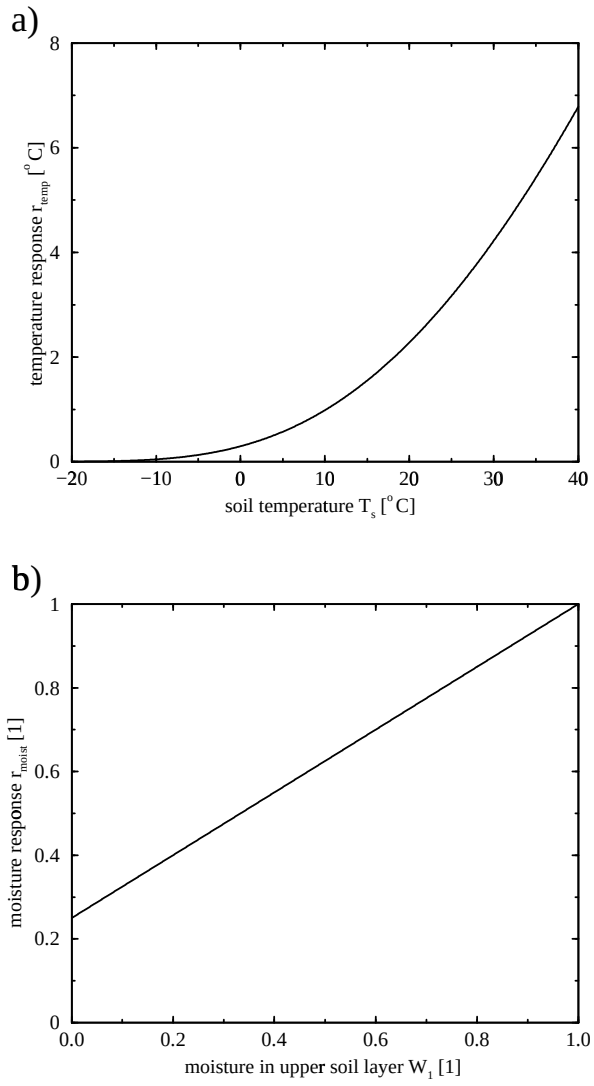

Figure 2.4: (a) Temperature response r_{temp} as a function of soil temperature T_s [*Lloyd and Taylor*, 1994]. (b) Moisture response r_{moist} as a function of moisture content in upper soil layer W_1 as a fraction of the water holding capacity [*Foley*, 1995].

2.4 Photosynthesis

Photosynthesis is calculated as a function of absorbed photosynthetically active radiation ($APAR$), temperature, atmospheric CO_2 concentration, day length, and canopy conductance, following *Farquhar et al.* [1980] and *Collatz et al.* [1992]. Calculations are performed for an averaged mid-month day and multiplied by the number of days in the month. The absorbed radiation $APAR$ is calculated for each PFT individual from the net photosynthetically active radiation PAR multiplied by the

fraction of incoming radiation intercepted by green vegetation:

$$APAR_{ind} = PAR \cdot FPC_{ind} \cdot L_{m,ind} \tag{2.11}$$

where FPC_{ind} is the PFT specific foliar projective cover, and $L_{m,ind}$ is the individual monthly averaged fraction of leaf coverage.

Daily net photosynthesis $A_{n,d}$ (gC/(m^{2}day)) is calculated using a standard non-rectangular hyperbola formulation, which gives a gradual transition between two limiting rates: J_E (molC/(m^{2}h)), describing the response of photosynthesis to $APAR$, and J_C (molC/(m^{2}h)), describing the Rubisco limited rate of photosynthesis [*Haxeltine and Prentice*, 1996].

$$A_{n,d} = \frac{J_E + J_C - \sqrt{(J_E + J_C)^2 - 4J_E J_C}}{2\Theta} \cdot t_d - R_d \tag{2.12}$$

where t_d is the day length in hours, R_d the daily leaf respiration rate (gC/(m^{2}day)), and $\Theta = 0.7$ a limiting parameter according to [*McMurtrie and Wang*, 1993]. The light limited (J_E) and the Rubisco limited rate of photosynthesis (J_C) are calculated differently for the two photosynthetic pathways distinguished by the LPJ model. Some rapidly growing plants such as tropical grasses, agricultural crops, and corn possess an unusual organization of the photosynthetic tissues in their leaves, and they utilize the so called C_4 photosynthetic pathway. Those plants fix CO_2 into four-carbon carboxylic acid, and so the effective concentration of CO_2 within the leaf is reduced, creating a steeper gradient for CO_2 into the leaf compared to the gradient for H_2O out from the leaf. The result of this is a higher water use efficiency in comparison to C_3 plants (up to twice as much CO_2 can be fixed with the same amount of water transpired). This is a big advantage for C_4 plants under drought conditions, but this metabolism is inefficient in shady places or under cool temperatures. In the LPJ model, when water is not a limiting factor, C_4 photosynthesis rates are lower than C_3 rates at temperatures below 20° C, and higher above this temperature. Water stress tends to have a greater effect on the modeled C_3 photosynthesis rate than on the C_4 rate. Thus water stress lowers the temperature at which the C_4 photosynthesis rate exceeds the C_3 rate.

The PFT specific canopy conductance for water, $g_{p,ind}$ (mm/s), is related to the photosynthesis rate as follows:

$$g_{p,ind} = g_{p,min} + \frac{1.6A_{dt}}{[C_a(1-\lambda)]} \tag{2.13}$$

where A_{dt} is the total daytime net photosynthesis (gC/(m^{2}day)), C_a the atmospheric CO_2 concentration in mole fraction, and $g_{p,min}$ stands for a PFT specific minimum canopy conductance (mm/s), which accounts for plant water loss not directly associated with photosynthesis. λ, the optimal ratio of intercellular and ambient CO_2

concentrations, is found by solving the following optimization problem numerically:

$$A_{n,d} + (1 - t_d/24)R_d - (g_{p,ind} - g_{p,min})\frac{C_a(1-\lambda)}{1.6} = 0 \tag{2.14}$$

2.5 Fire

The LPJ model simulates fire as a combination of fire occurrence and its effects on vegetation. Fire regimes are calculated annually. In order to save computation time and to allow a global simulation of the effect, we assume fire occurrence to be dependent only upon fuel load and litter moisture (amount of dry material available). Another assumption is that fire effects are only driven by the length of the fire season and the PFT specific fire resistances.

To start a fire the fuel has to reach a minimum temperature at which it ignites, and combustion will start if sufficient fuel is present at the site. A maximum fuel moisture is defined above which a fire would not spread, and an exponential power function is used to approximate the probability of the occurrence of at least one fire per day in a certain grid cell:

$$p(W_{1,d}) = exp\left[-\frac{\pi}{4}\left(\frac{W_{1,d}}{m_e}\right)^2\right] \tag{2.15}$$

where $W_{1,d}$ is the daily water content in the upper soil layer, used as a surrogate for litter moisture, and m_e is the moisture extinction threshold. The sum of the fire probabilities over a whole year equals the annual length of the fire season. The fraction of days with particular fire conditions, called fire index λ_f, is calculated as follows:

$$\lambda_f = \frac{1}{365}\sum_{d=1}^{365} p(W_{1,d}) \tag{2.16}$$

The proportion of a grid cell affected by fire Λ_g is a function of the fire index λ_f:

$$\Lambda_g(\lambda_f) = \lambda_f \cdot exp\left[\frac{\lambda_f - 1}{-0.13(\lambda_f - 1)^3 + 0.6(\lambda_f - 1)^2 + 0.8(\lambda_f - 1) + 0.45}\right] \tag{2.17}$$

This formulation is based on the hypothesis that the annual fractional area burnt first increases slowly, when the amount of days with particular fire conditions is relatively small, but increases more rapidly, when the length of the fire season approach the entire year (see figure 2.5). The fraction of individuals killed within the fractional area burnt depends upon the PFT specific fire resistance index α_f (table 2.1). Tropical raingreen and temperate broadleaved evergreen trees have greater resistances reflecting adaptive traits to fire conditions in many seasonally dry regions in Africa and Australia. Grasses, litter above ground, and dead woody tissue are fully consumed in the fractional area burnt, and released to the atmosphere as CO_2.

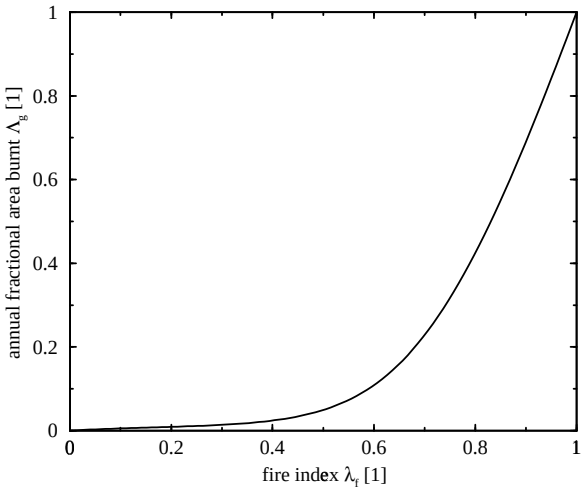

Figure 2.5: Proportion of a specific grid cell affected by fire as a function of the fire index, which is the annual fraction of days with particular fire conditions.

2.6 Model spinup and input data

The LPJ model is driven by monthly mean air temperatures (figure 2.6), monthly precipitation (figure 2.7) and monthly mean cloud cover (figure 2.8) according to *Leemans and Cramer* [1991], and annual atmospheric CO_2 concentrations. Soil texture classes according to *Zobler* [1986] are assigned to every grid cell. Since vegetation dynamics is strongly dependent upon interannual climate variations (e.g. wildfires only occur in years with extremely low precipitation), the use of a single average climatology will lead to an incorrect simulation of PFT distribution. Therefore the LPJ model is additionally forced with perturbations in annual climate data from 1856 to 1886 A.D. from a simulation by the Hadley Centre climate model HadCM2-SUL (*Johns et al.* [1997], *Mitchell et al.* [1995]). The data of this randomly selected time period of 31 years are repeated in order to preserve interannual climate variability. This combination of climate data results in temperatures T_{spinup}, precipitation P_{spinup}, and cloud coverage Cl_{spinup}.

The simulations in this study start from bare ground, and the model is run for 2000 years in order to reach an equilibrium state. Because the long term soil carbon pool with a turnover time of approximately 1000 years (table 2.3) would require many thousands of years to build up, its size is calculated analytically in order to save computation time. After 400 years, when litter carbon pool sizes are approximately constant (which means that vegetation is in equilibrium with climate), the slow soil

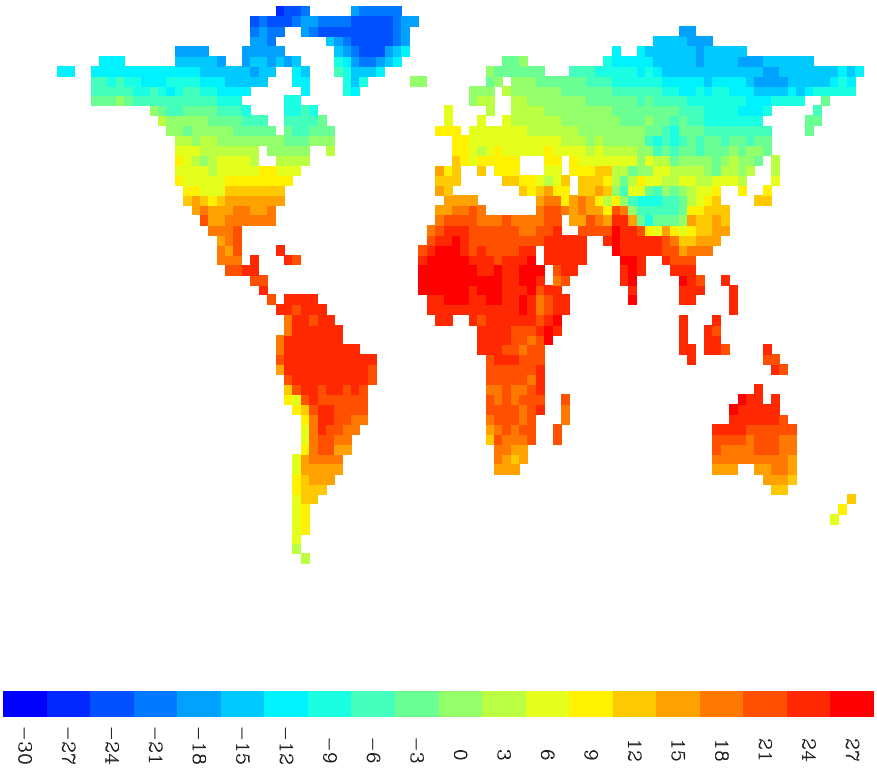

Figure 2.6: Geographical pattern of continental air temperatures [*Leemans and Cramer*, 1991]. Monthly mean values are averaged to annual mean temperatures in this figure. Temperatures are divided into 20 classes, and the legend shows the lowest value of each class in units °C.

organic matter pool size C_{ss} is calculated as follows:

$$\frac{dC_{ss}}{dt} = F_{d,lss} - k_{ss}C_{ss} \approx 0 \Rightarrow C_{ss} \approx \frac{F_{d,lss}}{k_{ss}} \tag{2.18}$$

where $F_{d,lss}$ in units gC/yr is the carbon flux to the slow soil pool due to litter decomposition, k_{ss} (1/yr) is the annual mean of the monthly decomposition rates of the slow soil pool, and t the time in years.

After this, the model is run another 1600 years until the global NEP on average is less than $1 \cdot 10^{-2}$ GtC/yr. This truncation condition ensures that vegetation distribution and carbon pools and fluxes are in an equilibrium state. During the model spinup, the atmospheric CO_2 level is set to a constant value of 280 ppmv (pre-industrial concentration).

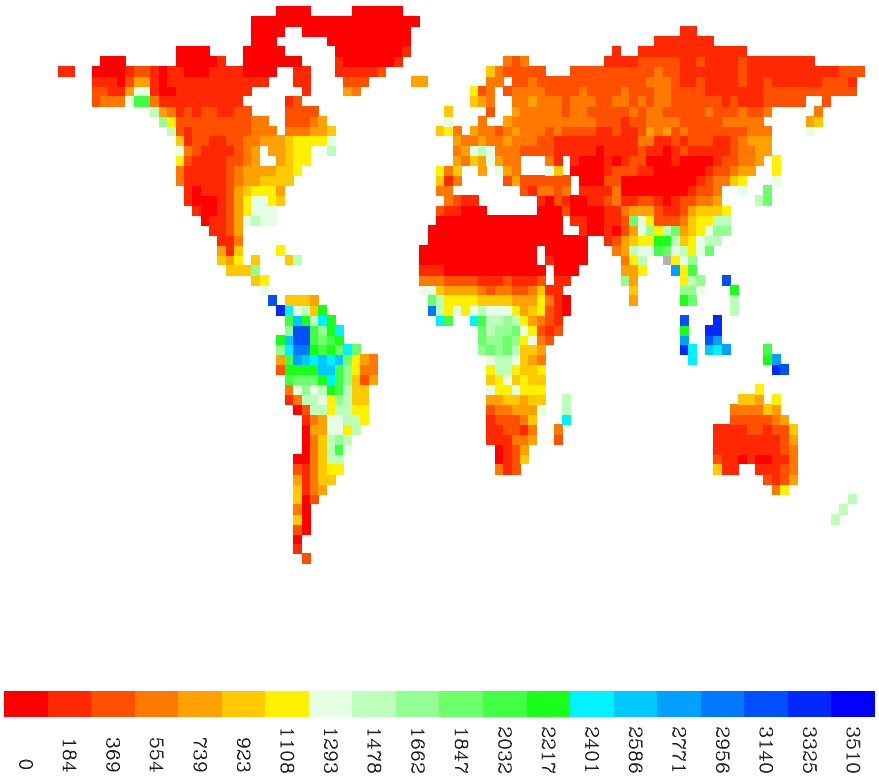

Figure 2.7: Geographical pattern of continental precipitation in units mm/yr [*Leemans and Cramer*, 1991].

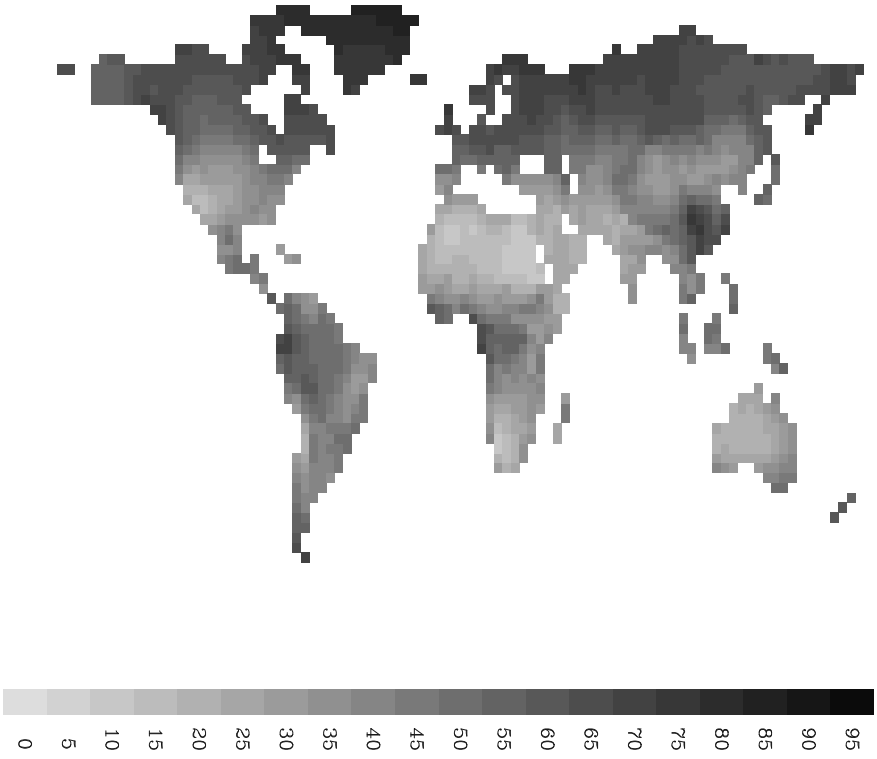

Figure 2.8: Geographical pattern of cloud cover (fraction of full cover) [*Leemans and Cramer*, 1991]. Monthly mean values are averaged to annual mean cloud covers in this figure.

Chapter 3

Model sensitivity analyses

3.1 CO_2 variations

The sensitivity of the LPJ model to variations in CO_2 is examined by forcing the model with different atmospheric CO_2 concentrations. The model spinup of 2000 years is performed as described in chapter 2.6. In order to be able to examine only effects caused by CO_2 perturbations, a baseline simulation is performed, forcing the LPJ-DGVM with the same data as during the model spinup (monthly climatology by *Leemans and Cramer* [1991], interannually variable climate data, and a constant atmospheric CO_2 level of 280 ppmv). For the step experiments, the atmospheric carbon level is instantaneously increased from the pre-industrial concentration of 280 ppmv to a higher value in the first year after the model spinup, and is then kept constant for 4000 years. In this study, we examine CO_2 step heights of 250, 500, 1000, and 2000 ppmv, resulting in atmospheric CO_2 concentrations of 530, 780, 1280, and 2280 ppmv, respectively.

The two plots in figure 3.1 show perturbations in terrestrial carbon inventories in response to our step experiments. The carbon stock resulting from the baseline run is removed, and only the terrestrial carbon due to CO_2 anomalies is plotted for the first five centuries after the carbon dioxide increase. The top panel (a) shows additional terrestrial carbon inventories in units GtC, in panel (b), the C stocks are normalized so that they equal one in the new equilibrium after 4000 years of increased CO_2 concentration. After the increase by 250 ppmv to an atmospheric concentration of 530 ppmv, 770 GtC are additionally absorbed by the terrestrial biosphere in the new equilibrium. For the step of 500 ppmv, the change in carbon stock is 1220 GtC, with a perturbation by 1000 ppmv, the additional carbon inventory is 1740 GtC, and with the highest step of 2000 ppmv, the additional terrestrial uptake is 2280 GtC. The baseline carbon stock is 2516 GtC. Therefore, a doubling of atmospheric concentrations results in an increase in terrestrial carbon inventory of approximately one third, and when the CO_2 concentration is tripled, the carbon stock is increased by

50% if the climate is kept constant. The atmospheric CO_2 step height as a function of the terrestrial carbon uptake is shown in figure 3.2. The values simulated by the LPJ are spline fitted, and the appropriate curve indicates that the appropriate relation is not linear. The more the CO_2 step height increases the less additional carbon is taken up by the biosphere, which points out that the carbon storage capacity of the terrestrial biosphere is limited.

After an atmospheric CO_2 increase by 500 ppmv, half of the whole carbon increment enters the vegetation pool, which is increased by 70% compared to its baseline content C_{spinup} (table 3.1). The slow organic matter pool takes up one third of the additional carbon, and the rest of ΔC enters the slow soil pool and the litter pools. The reason for the big amount of carbon entering the vegetation pool is an increased plant growth rate resulting from elevated atmospheric CO_2 concentrations, which is a positive feedback to terrestrial carbon uptake. This so called carbon fertilization effect is described in section 3.1.1.

carbon pool	C_{spinup} [GtC]	C_{500} [GtC]	ΔC [GtC]	$\Delta C/C_{spinup}$ [1]
vegetation	869	1478	609	0.70
litter above ground	113	173	60	0.53
litter below ground	82	99.5	17.5	0.21
fast soil organic matter	1002	1392	390	0.39
slow soil organic matter	450	593.5	143.5	0.32
sum of all pools	2516	3736	1220	0.48

Table 3.1: Carbon uptake of the C pools after an instantaneous atmospheric CO_2 increase by 500 ppmv. C_{spinup} are the carbon inventories in the equilibrium after the model spinup (see table 2.3), C_{500} are the C stocks in the new equilibrium 4000 years after the step event, and the differences between C_{500} and C_{spinup} are plotted as ΔC in units GtC or as a fraction of the baseline inventory.

An interesting measure is the typical timescale on which the LPJ reacts to the CO_2 perturbations. The terrestrial carbon uptake relative to the C inventory in the new equilibrium increases faster for higher atmospheric CO_2 steps (panel (b) in figure 3.1). For the increase by 2000 ppmv, 90% of the carbon is taken up by the terrestrial biosphere after 304 years, whereas with a CO_2 increase by 250 ppmv, this level is not reached until 477 years after the step-like increase. This effect can be explained by a stronger carbon fertilization effect (see section 3.1.1) and bigger changes in the vegetation distribution for higher atmospheric CO_2 perturbations (already in the first years after the CO_2 increase).

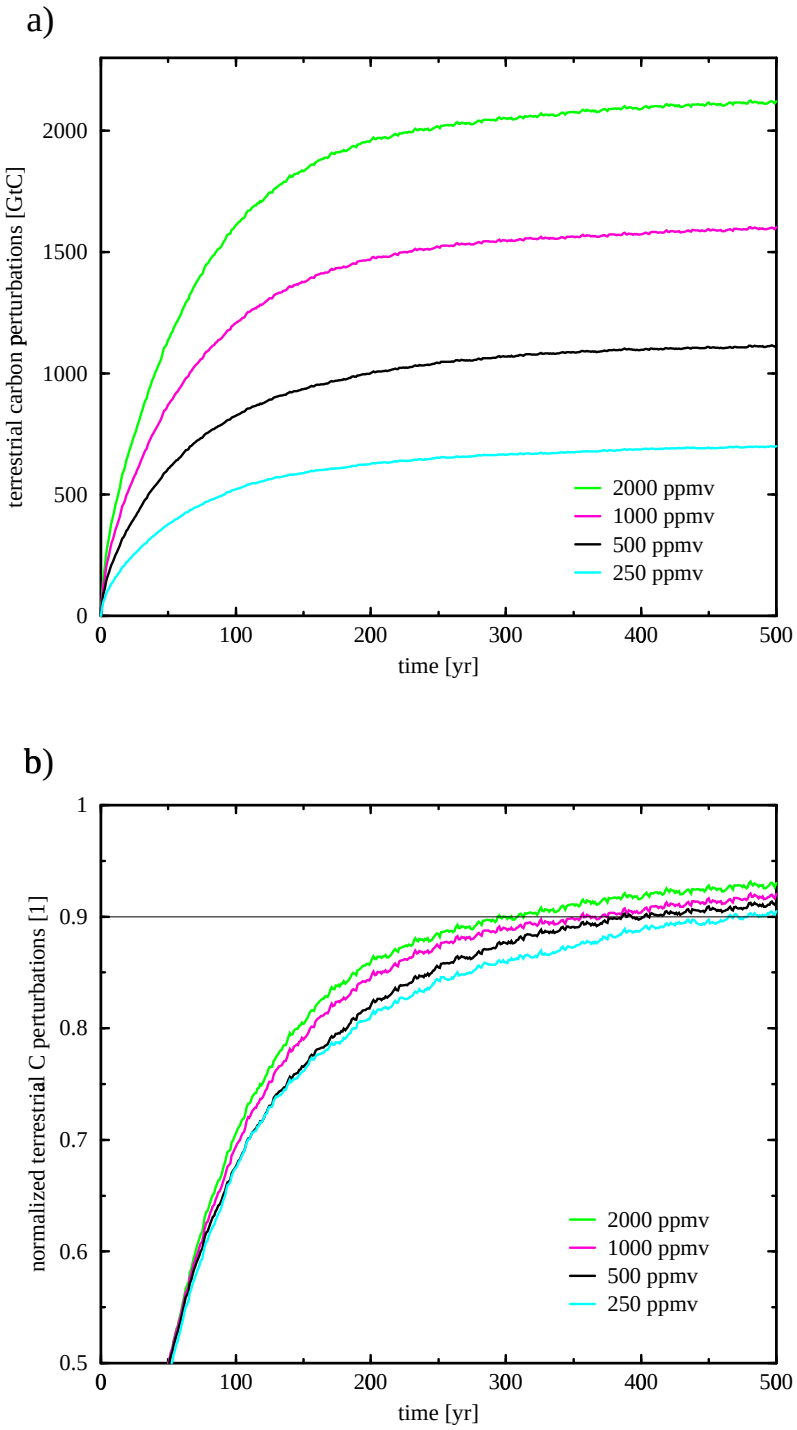

Figure 3.1: Perturbations in terrestrial carbon inventory due step-like increases of atmospheric CO_2 concentrations by 250, 500, 1000, and 2000 ppmv, respectively. (a) Terrestrial carbon stock anomalies in units GtC. (b) Normalized perturbations in terrestrial C inventory so that the stock in the new equilibrium after the CO_2 increases equals to one in all three cases.

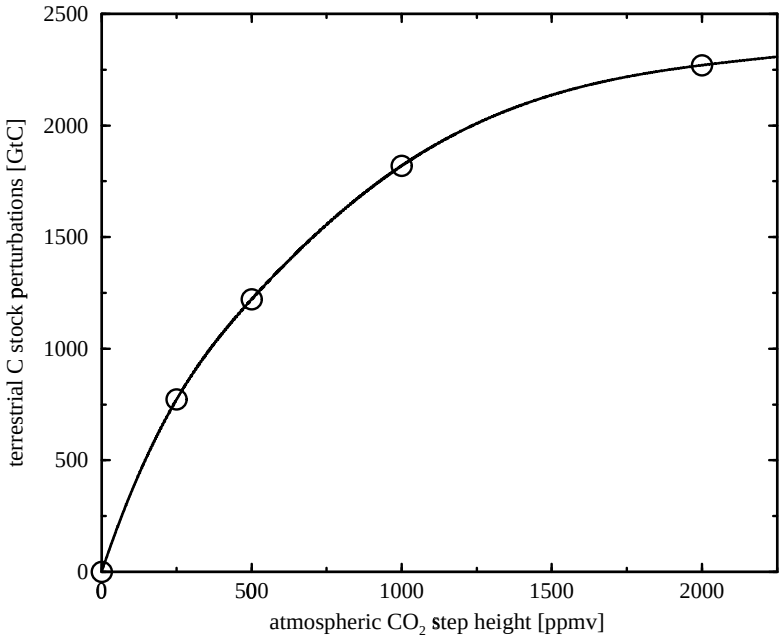

Figure 3.2: Relation between perturbations in terrestrial carbon stock (GtC) and heights of step-like atmospheric CO_2 increases. Circles indicate values from model simulations, the curve is a spline fitted function representing the model values.

As a representative of all different CO_2 change simulations, we focus on the step-like increase by 500 ppmv, and examine the behavior of the related carbon fluxes (figure 3.3).

The perturbation in net primary production ΔNPP increases by 58 GtC/yr in the first years with a higher CO_2 concentration and then stabilizes at 46 GtC/yr in the new equilibrium (pre-industrial NPP is approximately 68 GtC/yr). The reaction to this is an increased heterotrophic respiration ΔR_h of up to 40 GtC/yr (pre-industrial R_h: 60 GtC/yr). Together with the additional carbon flux ΔR_f of 6 GtC/yr into the atmosphere due to fire (pre-industrial R_f: 7 GtC/yr), the net ecosystem production ΔNEP tends to zero, which indicates that the carbon fluxes are in a new equilibrium. In the year 1000 after the step-like increase, ΔNEP is at a value of 0.06 GtC/yr, and approximately 4000 years after the CO_2 increase, the net production is below 0.01 GtC/yr. The reason for the transient fluctuations of all the four curves with a repetition time of 31 years is the interannually variable climate.

As expected, the biggest carbon increase is in regions with the largest baseline stock such as the mid-latitudes and the tropics (figure 3.4), but surprisingly, a huge uptake

of up to $6{\cdot}10^4$ gC/m^2 can be observed in South America (Bolivia, Paraguay, southern Brazil) and in Africa (Tanzania, Kenya, Ethiopia). This big amount of additional carbon entering the terrestrial biosphere is caused by a fundamental change in the vegetation pattern in those regions. It is demonstrated in figure 3.5 on page 36 that the biggest change in those areas is the displacement of tropical raingreen trees by tropical evergreen plants under higher CO_2 concentrations.

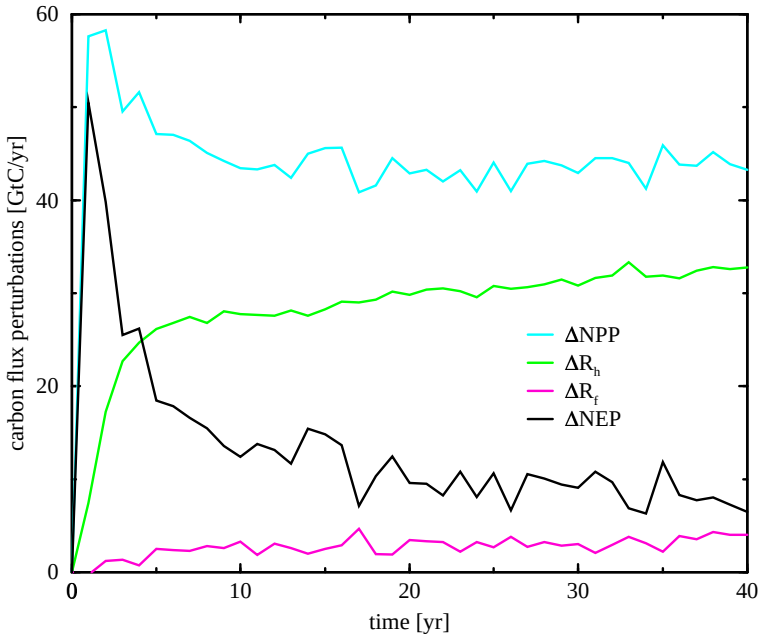

Figure 3.3: Carbon flux perturbations resulting from a step-like increase by 500 ppmv in atmospheric CO_2 concentration in the year zero. The blue curve is the net primary production ΔNPP, the green line is the heterotrophic respiration ΔR_h, the red curve stands for the carbon flux due to fire (ΔR_f), and the black curve is the resulting net ecosystem production ΔNEP.

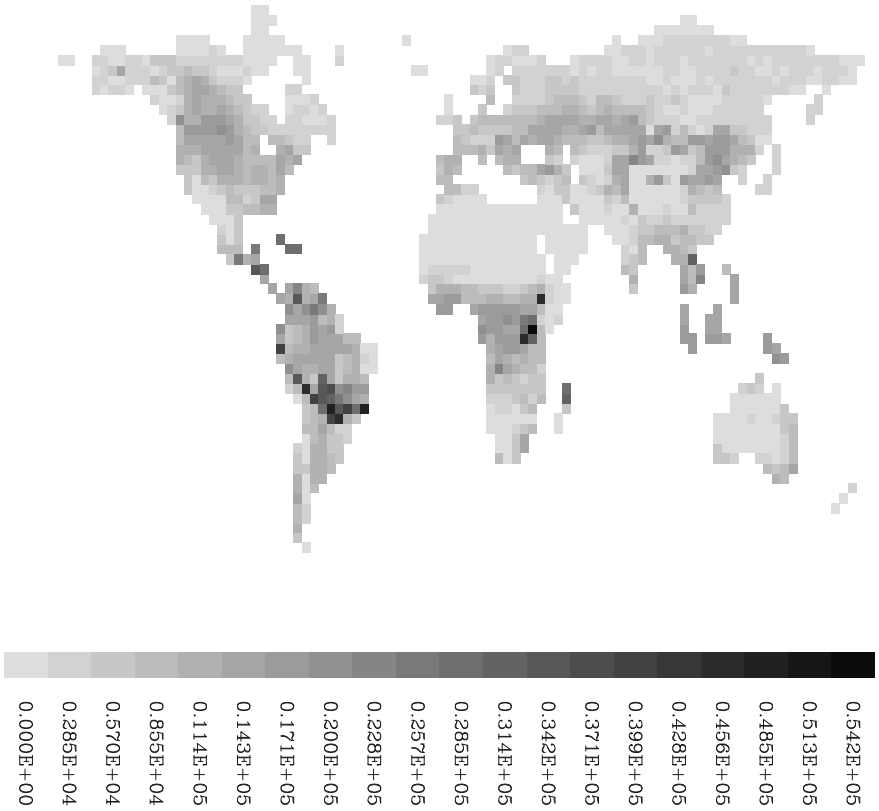

Figure 3.4: Perturbations in the terrestrial carbon inventory due to a step-like atmospheric CO_2 increase by 500 ppmv. Carbon stock anomalies in the new equilibrium are divided into 20 classes, and the legend shows the lowest value of each class in units gC/m^2.

3.1.1 Plant functional types

For a better understanding of vegetation dynamics under different atmospheric CO_2 levels and of the carbon uptake of different plant functional types, the foliar projective coverages of the nine PFTs distinguished by the LPJ model are examined for atmospheric CO_2 concentrations of 280 and 780 ppmv, respectively (figures 3.5, 3.6, and 3.7). First of all, it can be observed that most of the PFTs grow better with higher atmospheric carbon dioxide concentrations. The foliar projective cover averaged over all gridcells with a CO_2 concentration of 280 ppmv is 74.8%, whereas in the case of 780 ppmv, mean FPC is 81.8%. The effect of increased growth under elevated CO_2 conditions is known as the CO_2 fertilization effect. It has been confirmed by numerous field and laboratory studies that the productivity of individual plants is increased due to the stimulations of photosynthesis by higher atmospheric concentrations of CO_2. However, it is less clear whether elevated CO_2 levels also result in increased carbon storage at an ecosystem level [*Kicklighter et al.*, 1999].

In the LPJ model, photosynthesis is simulated according to the BIOME 3 model of *Haxeltine and Prentice* [1996] (section 2.4), and the CO_2 fertilization effect is mainly considered by the CO_2 dependence of the canopy conductance (equation 2.13). With enhanced atmospheric concentrations, plants tend to close their stomatas in order not to loose too much moisture, while the CO_2 maintenance is still sufficient for photosynthesis with a smaller canopy conductance. The increased water supply results in a growth enhancement of vegetation, and plants are also able to grow under drier conditions.

If we examine the global coverage of the first two plant functional types (tropical broadleaved evergreen and raingreen trees) under low and high CO_2 concentrations, we can identify an interesting effect briefly mentioned above. With a CO_2 concentration of 280 ppmv, the water stress factor W temporarily falls below 35% in certain regions of tropical rainforests. The ability of raingreen trees to shed their leaves under such conditions is an advantage over evergreen trees. Therefore, both phenologies coexist in most parts of the tropics. In the equilibrium with high carbon dioxide levels, the soil water content is increased because of reduced evapotranspiration. The properties of evergreen plants (a) are specialized for non-water-stressed conditions. The fraction of roots in the upper soil layer f_r is bigger for evergreen trees than for raingreen trees (table 2.1), which means that more water is available for them, because in tropical forests, the soil layer containing water and nutrients is only shallow. Turnover times of leaves (τ_l), sapwood (τ_s), and roots (τ_r) are bigger for evergreen trees as compared to raingreen trees, which is another advantage for this phenology because the loss of carbon for reproduction is reduced. Therefore, tropical raingreen trees only survive in borderlands and they are displaced by evergreen trees everywhere else under increased CO_2 concentrations.

The three temperate PFTs (from (*c*) to (*e*)) do not significantly change their pattern of coverage due to the carbon dioxide increase. The only difference is a slightly increased FPC due to CO_2 fertilization, which is also the case for boreal needleleaved evergreen and for boreal summergreen trees. Those PFTs occupy almost exactly the same grid fields for both CO_2 levels with a generally higher FPC in the case of enhanced atmospheric carbon dioxide concentrations.

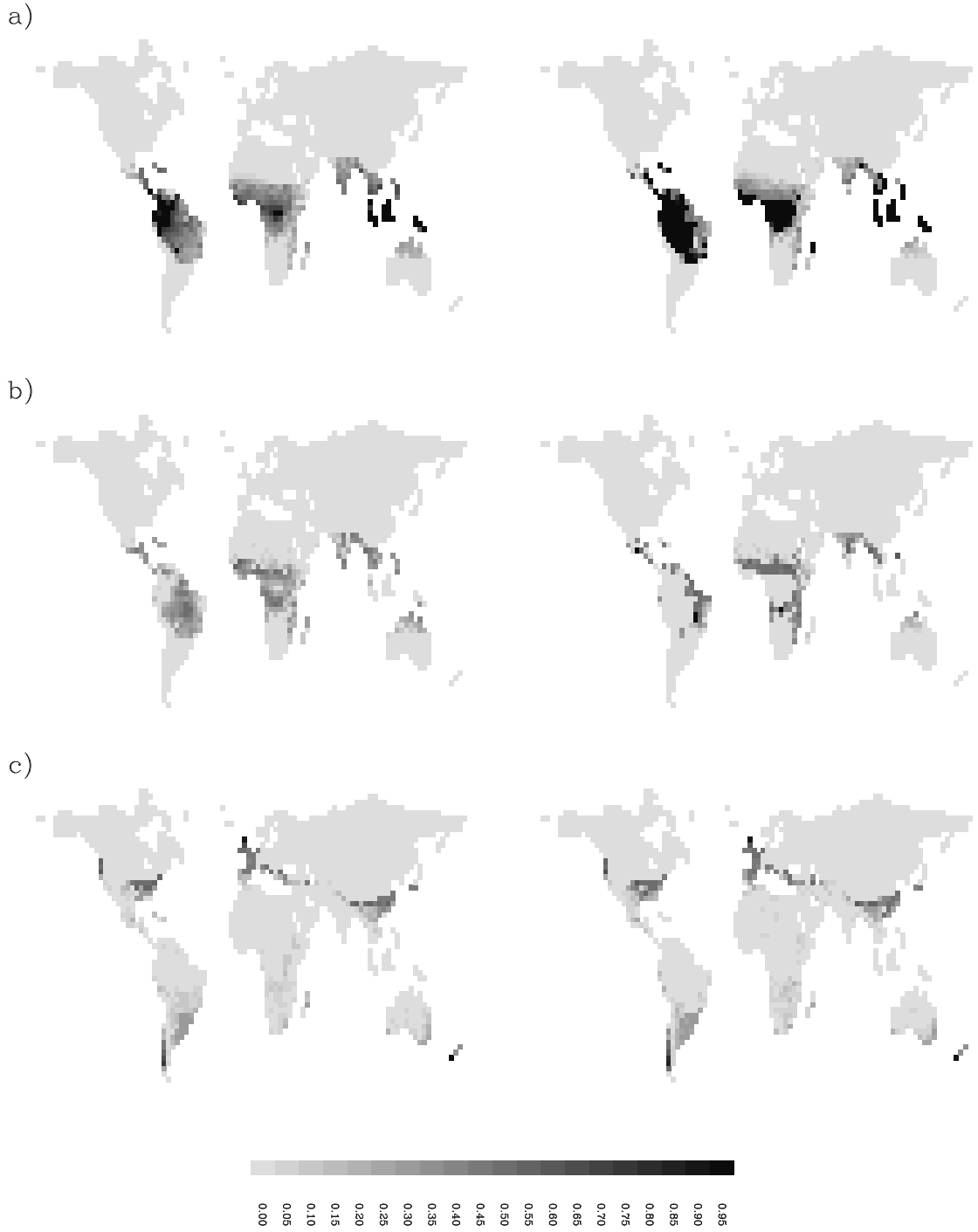

Figure 3.5: Foliar projective cover (grid cell fraction) of the following plant functional types: (a) tropical broadleaved evergreen trees, (b) tropical broadleaved raingreen trees, (c) temperate needle-leaved evergreen trees. The maps on the left side are showing pre-industrial conditions (280 ppmv), in the right column the atmospheric CO_2 concentration is 780 ppmv.

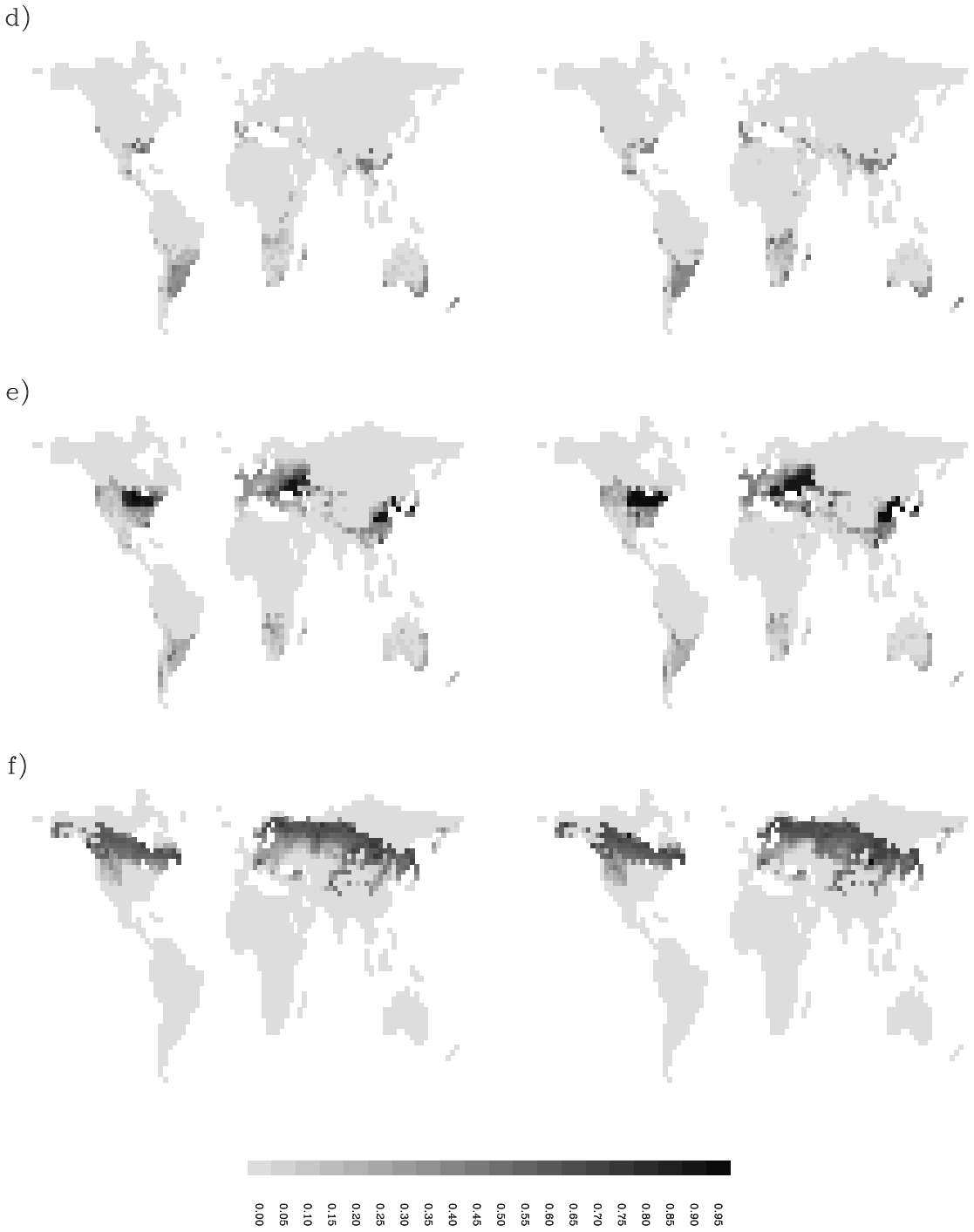

Figure 3.6: Foliar projective cover (grid cell fraction) of the following plant functional types: (d) temperate broadleaved evergreen trees, (e) temperate broadleaved summergreen trees, (f) boreal needleleaved evergreen trees. The maps on the left side are showing pre-industrial conditions (280 ppmv), in the right column the atmospheric CO_2 concentration is 780 ppmv.

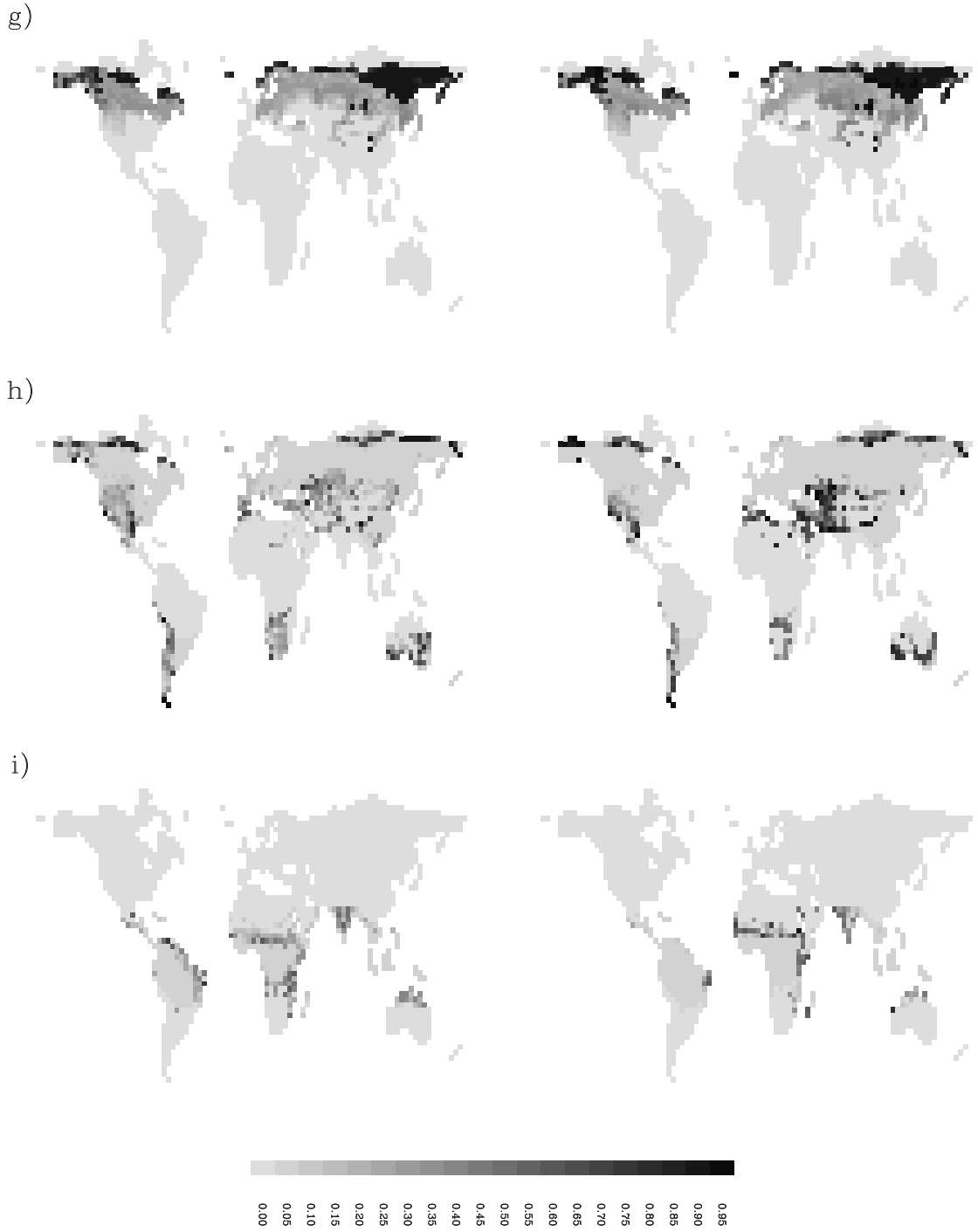

Figure 3.7: Foliar projective cover (grid cell fraction) of the following plant functional types: (g) boreal summergreen trees, (h) cool perennial grass (C_3), (i) C_4 warm perennial grass (C_4). The maps on the left side are showing pre-industrial conditions (280 ppmv), in the right column the atmospheric CO_2 concentration is 780 ppmv.

The global mean FPC of cool grass (C_3 photosynthetic pathway) is slightly higher with increased atmospheric CO_2 levels, but the changes in distribution have to be discussed locally. In North and South America, the extent of C_3 grass is generally smaller under conditions with a higher CO_2 concentration because of the stronger appearance of temperate and boreal trees, which are favored over grass due to their dominant position in the canopy with competitive advantage for light over understory vegetation. Additionally, trees are in advantage for water competition (when water is not a limiting factor) because their roots are deeper. In southern Africa and in Australia, we can observe decreased grass extents under elevated CO_2 levels. In regions all over the world where cool grass is already dominating with low atmospheric CO_2 levels, it even increases with higher carbon dioxide concentrations due to the CO_2 fertilization effect, especially in Alaska, from Kazakhstan to Iran, and between the Sahara and the Mediterranean.

In contrast to C_3 grass, warm grass (C_4 photosynthetic pathway) is generally slightly decreasing under high CO_2 conditions. In South America and south of the African rainforest, C_4 grass is almost completely ruled out by tropical trees. Between the Sahara desert and the African rainforest, warm grasslands are vegetated more densely, because there is no competition with woody PFTs.

Summarizing those observations, we conclude that the effects of variations in atmospheric CO_2 on vegetation structure are relatively minor, with an increased plant growth due to the CO_2 fertilization effect under elevated atmospheric CO_2 concentrations, whereas trees tend to rule out grass PFTs because of their dominant position in light and water competition. Another effect of a higher atmospheric carbon dioxide level is an internal change of vegetation in the tropics because of an increased soil water availability.

3.1.2 Grid cell analyses

In most cases, several plant functional types are cohabiting in a certain region, forming a biome. In order to understand the vegetation resource competition of the LPJ model, it is interesting to examine changes in plant compositions and carbon fluxes within different biological communities. The major world biomes are called tundra, taiga, temperate forest, temperate grassland, desert, savannah, and tropical rainforest (see appendix A). In order to analyze vegetation dynamics within those ecosystems, we have chosen six specific grid cells in regions dominated by different plant functional types (figure 3.8). Grid cell (A), alternately dominated by cool grass and boreal summergreen trees respectively (representing tundra), is situated in Central Canada, north west of Hudson Bay. Location (B), where boreal conifers and deciduous trees are situated (taiga), is examined in Central Russia, whereas in Switzerland (C), vegetation is a composition of boreal and temperate trees (temperate forest). Grid cell (D) is located in Texas, USA, north west of the Gulf of Mexico,

and this region is dominated by cool grass (temperate grassland biome). So as to examine a location with warm grass and tropical trees (savannah), we concentrate on the coast of Tanzania in Central Africa (E), and grid cell (F) within the tropical rainforest lies in western Brazil.

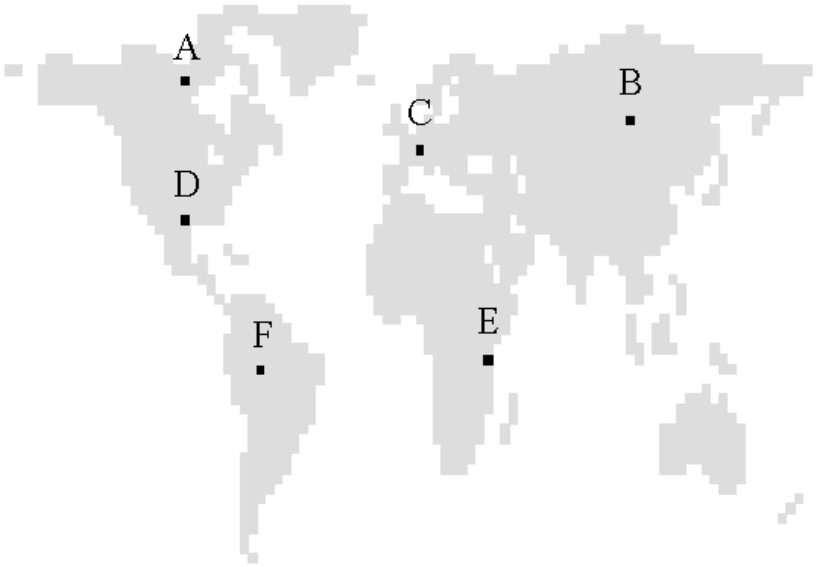

Figure 3.8: Location of six chosen grid cells representing different biomes. (A) represents the tundra, (B) the taiga, (C) temperate forests, (D) temperate grasslands, (E) savannah, and (F) tropical rainforests.

Perturbations in carbon fluxes and plant compositions of the six biome grid cells are examined for an instantaneous increase of atmospheric CO_2 by 500 ppmv (from 280 to 780 ppmv) in the year zero (figures 3.9 and 3.10). The two panels in (a) are the results for the grid cell representing tundra, (b) represents the taiga, (c) is the temperate location in Switzerland, (d) the temperate grassland grid cell, (e) stands for the the savannah, and (f) for the tropical rainforest. The plots in the left column show an 31-year average of carbon flux anomalies during the first 200 years after the CO_2 increase. The fluxes are plotted in units $gC/(yr \cdot m^2)$, so that the six grid cells with different expanses can directly be compared. The curves are averaged over 31 years in order to neglect rapid fluctuations caused by the interannually variable climate data, which are necessary to drive fire events (see section 2.6). In the right column, foliar projective covers (as fractions of the appropriate grid cell areas) of all present plant functional types are plotted for a certain time period before and after the step-like atmospheric CO_2 increase.

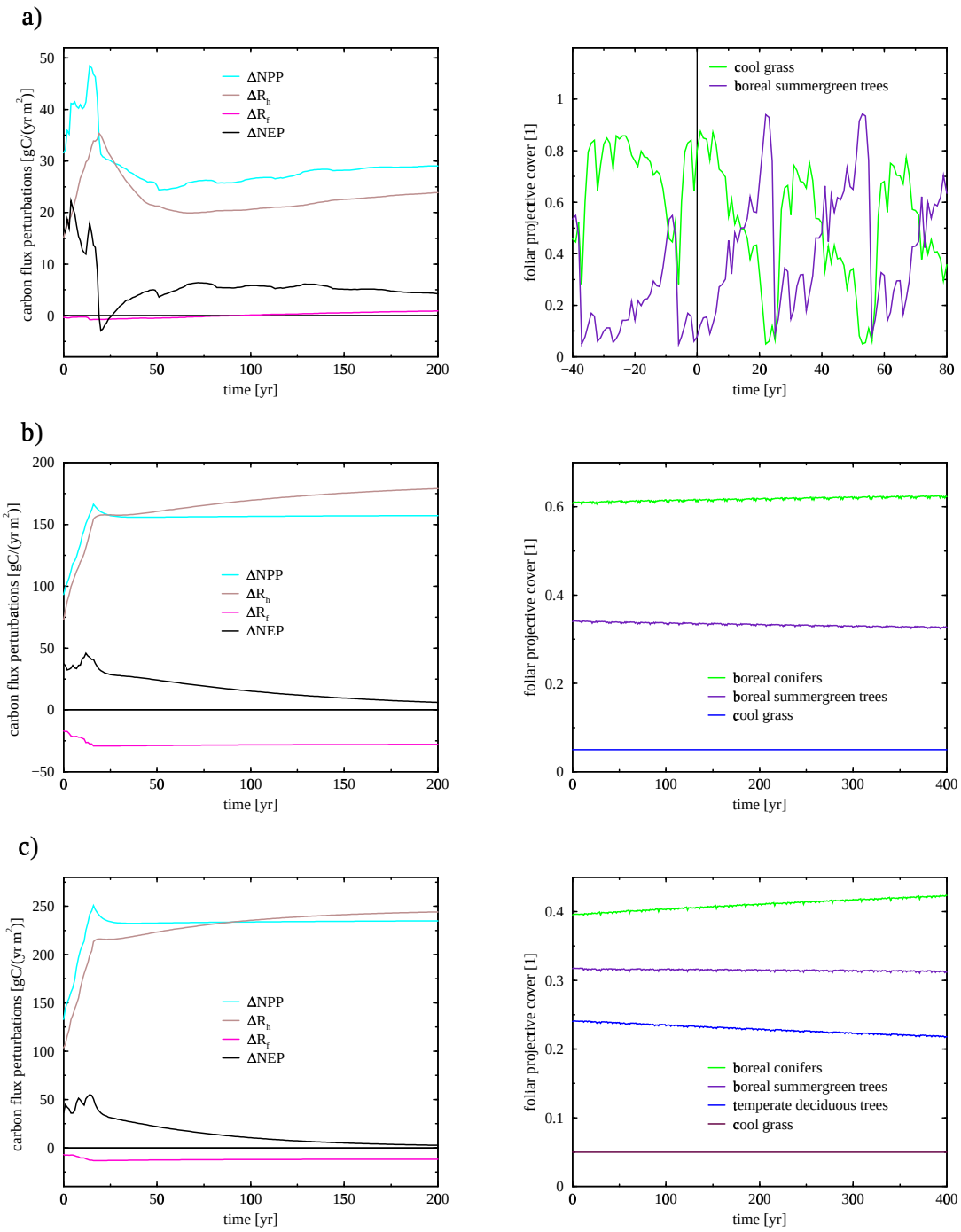

Figure 3.9: Perturbations in carbon fluxes and foliar projective covers of different biomes after an instantaneous atmospheric CO_2 increase by 500 ppmv in the year zero. In (a), results for the grid cell representing tundra are plotted, (b) stands for the taiga location, and (c) is the temperate forest grid cell. In the left column, 31-year averages of perturbations in carbon fluxes are plotted in units $gC/(yr \cdot m^2)$. The curves are averaged with a period of 31 years in order to neglect rapid fluctuations caused by the interannually variable climate data. In the right column, FPCs of all present plant types are plotted in spatial fractions of the current grid cell. Different time scales are chosen to provide better clarity.

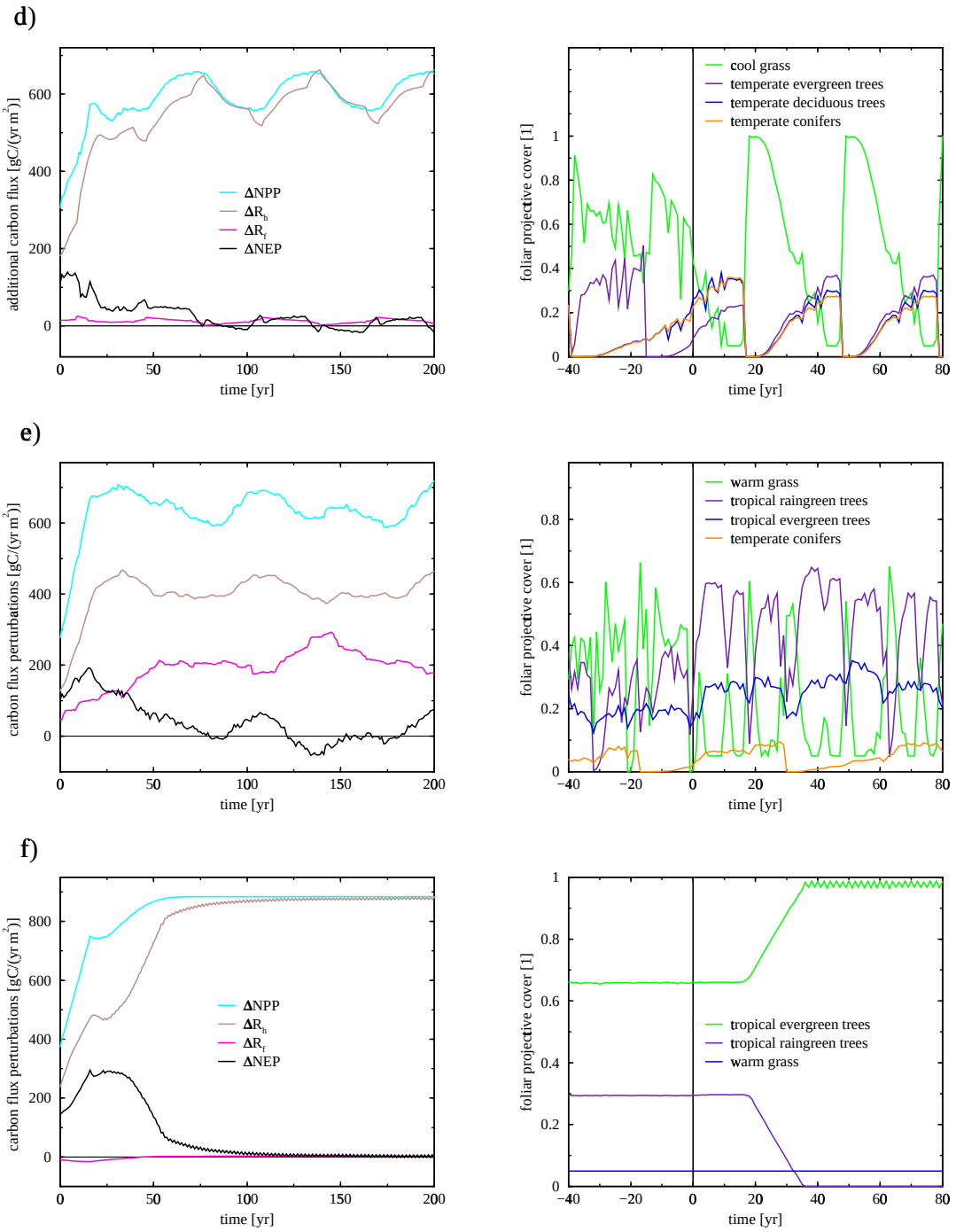

Figure 3.10: Perturbations in carbon fluxes and foliar projective covers of different biomes after an instantaneous atmospheric CO_2 increase by 500 ppmv in the year zero. In (d), results for the grid cell representing temperate grasslands are plotted, (e) stands for the savannah location, and (f) is the tropical rainforest grid cell. In the left column, 31-year averages of carbon flux perturbations are plotted in units $gC/(yr \cdot m^2)$. The curves are averaged with a period of 31 years in order to neglect rapid fluctuations caused by the interannually variable climate data. In the right column, FPCs of all present plant types are plotted in spatial fractions of the current grid cell.

Because the net ecosystem production NEP is highly dependent on vegetation density, properties of present plants, and on climatic variables, we can examine that this flux is significantly bigger the closer a biome is to the equator. So, ΔNEP in the tundra of Canada is only up to $22\,\mathrm{gC/(yr{\cdot}m^2)}$ after the CO_2 increase, whereas in the tropical rainforest, ΔNEP reaches a value of $295\,\mathrm{gC/(yr{\cdot}m^2)}$.

The temporal behavior of perturbations in carbon fluxes of the three grid cells at mid- to high latitudes (a), (b), and (c) are qualitatively similar. After an overshooting in the first years with high CO_2 concentrations, the ΔNPP values tend to an equilibrium state, and the plant respirations ΔR_h behave similarly. Examining the evolution of ΔNEP shows the time scales for reaching the new equilibrium after the CO_2 increase: 200 years after the step-like increase, ΔNEP of (a) is $4\,\mathrm{GtC/(yr{\cdot}m^2)}$ (which is 18% of the maximal ΔNEP value), for (b), it is $6\,\mathrm{GtC/(yr{\cdot}m^2)}$ (13%), and for (c), the change in net production is $2.5\,\mathrm{GtC/(yr{\cdot}m^2)}$ (5%). After 400 years of high CO_2 concentrations, all ΔNEP values are only approximately $1\,\mathrm{GtC/(yr{\cdot}m^2)}$, and the new equilibrium is almost reached. Carbon fluxes of the two grassland biomes (d) and (e) show significant short term perturbations because of large fluctuations in vegetation compositions. The high number of fire events in the savannah results in a high carbon release ΔR_f, which reaches a maximal value of almost $300\,\mathrm{gC/(yr{\cdot}m^2)}$. Carbon fluxes in tropical rainforest show an interesting evolution. Resulting from a fast change in vegetation composition, the carbon fluxes switch to a new equilibrium between 20 and 100 years after the atmospheric increase. In the year 100, ΔNEP is $2.7\,\mathrm{GtC/(yr{\cdot}m^2)}$, which corresponds to approximately 1% of the maximal ΔNEP value. The importance of tropical rainforests in the carbon cycle is pointed out by the very high net primary production of $885\,\mathrm{gC/(yr{\cdot}m^2)}$.

In the taiga and the temperate forest, plant compositions only change smoothly over several hundred years, with a slight advantage of conifers over broadleaved trees under increased CO_2 concentrations in both locations. The tundra grid cell shows short term vegetation dynamics. With a period of exactly 31 years (which corresponds to the added interannually variable climate data, boreal summergreen trees and C_3 grass alternately cover the appropriate grid cell. This unstable equilibrium is mainly caused by fire events which occur with the same period due to the repeated climate data. After trees have reached a certain coverage due to their advantage in light and water competition over grass, there is a year with a long fire season, and nearly all woody PFTs are burnt. Immediately after these events, grass is growing fast, because enough light and water is available, and after having dominated the landscape for several years, it is partly ruled out by recovering boreal trees. After the atmospheric CO_2 increase, trees are favored over to grass due to the CO_2 fertilization effect (see section 3.1.1), and they almost reach full spatial coverage every 31 years.

For the two grass biome grid cells (temperate grassland and savannah), we observe large transient fluctuations in vegetation composition as well. In the grassland of

Texas, there are only few single years with long fire seasons during one period of the repeated climate data, and vegetation dynamics clearly reflects the repetition time of 31 years. The burning of trees and the following increase of grass can also be observed in the savannah, although big fire events occur more frequently. As mentioned in the description of this biome in appendix A, wildfires are extremely important in order to maintain its typical landscape. In both locations, grasses are covering approximately 50% of the grid cells under pre-industrial CO_2 levels, and they are temporarily ruled out by trees after the instantaneous increase due to carbon fertilization.

An interesting change in vegetation composition can be found in the tropical rainforest grid cell. From 20 to 40 years after the atmospheric CO_2 increase, evergreen trees gradually rule out raingreen plants. As we have already mentioned before, plants with an evergreen seasonality are in advantage over raingreen trees under humid conditions, which is the case after an instantaneous CO_2 increase. This significant and fast change in vegetation distribution forces the carbon fluxes to switch into a new equilibrium, because of different carbon uptake and respiration properties of the two tropical tree types.

3.2 Temperature variations

Another important forcing parameter except of atmospheric CO_2 is the air temperature. As mentioned in section 2.6, the LPJ model is driven by a baseline climatology of *Leemans and Cramer* [1991] with monthly minimal and maximal temperature data for each grid cell in order to calculate monthly mean values. Apart from this, interannually variable climate data with a repetition time of 31 years are added so as to drive fire regimes (*Johns et al.* [1997], *Mitchell et al.* [1995]), resulting in the spinup temperature T_{spinup}. The sensitivity of the LPJ-DGVM to variations in temperature is examined with step-like global temperature perturbations by $+1^\circ$ C and -1° C respectively after a model spinup of 2000 years. A third experiment is a sudden temperature decrease by 1° C for all grid cells in the northern hemisphere (NH), and a simultaneous increase by 1° C in the southern hemisphere (SH). Zonally averaged mean continental air temperatures by *Leemans and Cramer* [1991] and temperature input data for the third experiment are plotted in figure 3.11. The atmospheric CO_2 concentration is set to a constant value of 280 ppmv for all three experiments, and the simulation is performed for 4000 years after the step-like temperature change.

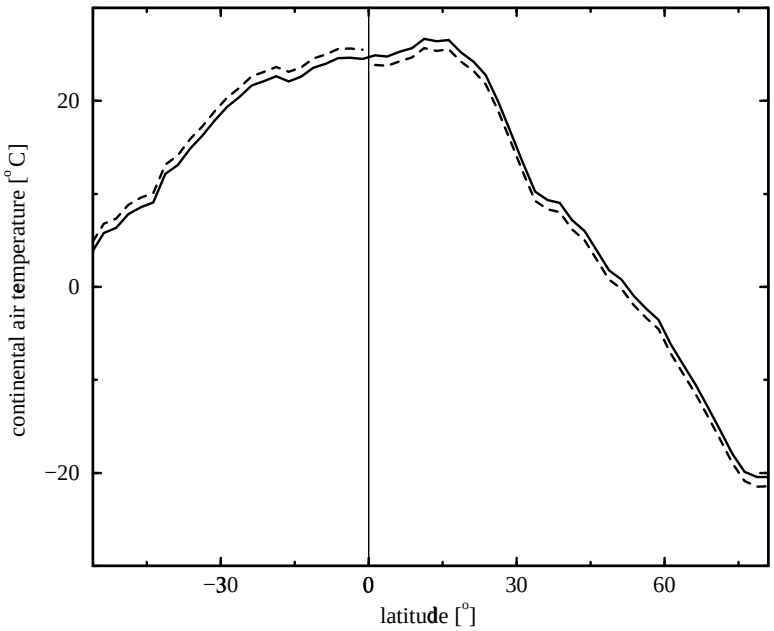

Figure 3.11: Zonally averaged mean continental air temperatures by *Leemans and Cramer* [1991] (solid line). Dashed lines show temperature input data for the experiment which distinguishes between northern and southern hemisphere, respectively (–1° C in the NH, and simultaneously +1° C in the SH).

Terrestrial carbon inventory perturbations resulting from the different temperature experiments are examined in figure 3.12. After a global increase of the air temperature by 1° C, the terrestrial biosphere loses 65 Gt carbon into the atmosphere until the new equilibrium is reached. The overshooting immediately after the temperature perturbation (the stock is reduced by 83 GtC in the year 150) and the following approach of the equilibrium state is caused by significant changes in vegetation distribution, especially in northern mid- and high latitudes (figure 3.13). Under increased air temperatures, all PFTs shift to slightly higher latitudes, where they find optimal growing conditions. Therefore, terrestrial carbon storage decreases in the southern part of boreal regions (USA and Eurasia), whereas the storage is increased in taiga regions. When the temperature is globally reduced by 1° C, the increase in carbon stock is 85 GtC. The main part of land area is in the northern hemisphere (with the LPJ resolution, 1307 grid cells are north of the equator, and only 324 in the southern hemisphere). So for the third experiment, the global carbon stock is mainly influenced by the air temperature decrease in the northern hemisphere, and the C inventory increases. The additional terrestrial carbon stock after having reached the new equilibrium is 27 GtC.

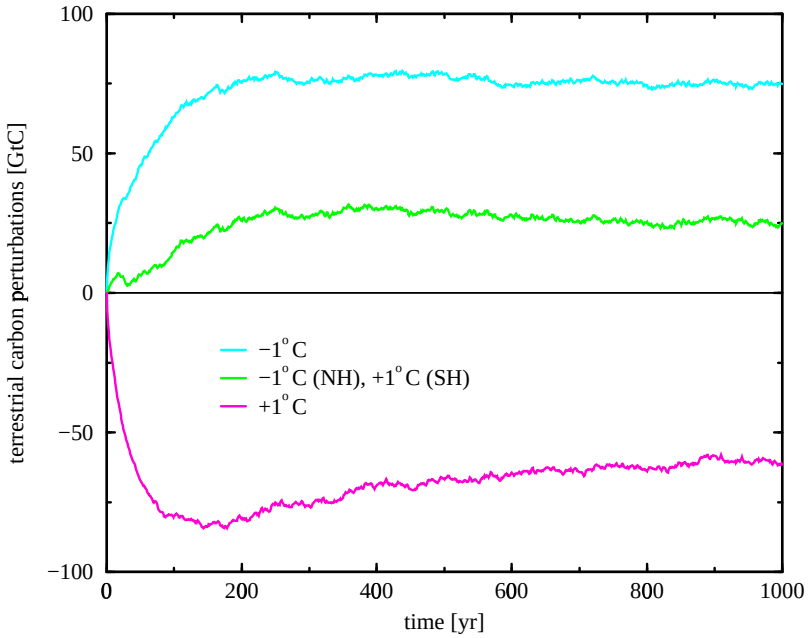

Figure 3.12: Perturbations in terrestrial carbon inventories due to air temperature steps. The red curve represents a global increase by 1° C, the blue line a decrease by 1° C, and the green line is the carbon stock after a temperature step of –1° C in the northern hemisphere and +1° C in the southern hemisphere, respectively. Atmospheric CO_2 concentrations are set to a pre-industrial value of 280 ppmv.

After an instantaneous temperature perturbation by –1° C, plants tend to open their stomatas because they lose less moisture than under elevated temperatures. This forces the gross primary production GPP to increase, and the autotrophic respiration R_a simultaneously sinks. Those effects result in an increased NPP, which is calculated as the difference between GPP and R_a (upper panel in figure 3.14). Because heterotrophic respiration R_h decreases with lower temperatures due to smaller decomposition rates, the resulting ΔNEP is evidently above zero GtC/yr immediately after the instantaneous temperature decrease, which means that carbon is taken up from the atmosphere by terrestrial pools. For a global temperature increase by 1° C, those effects are directly opposed, and resulting anomalies in carbon fluxes are reverse (lower panel in figure 3.14). Quantitatively compared, changes in vegetation are larger immediately after an increase in temperature than after a decrease (although the biosphere takes up more carbon in the long run with lower temperatures). So, ΔNEP increases by 5.3 GtC/yr immediately after a temperature perturbation by –1° C, whereas after a perturbation by +1° C, net production decreases by 6.3 GtC/yr.

Because of a larger continental area in the northern hemisphere, ΔNEP is positive after a simultaneous temperature perturbation by -1° C in the NH and $+1^\circ$ C in the SH, which means that the terrestrial biosphere takes up carbon from the atmosphere (figure 3.15). But in this experiment, higher air temperatures in the southern hemisphere reduce carbon uptake, and ΔNEP stays below 1 GtC/yr.

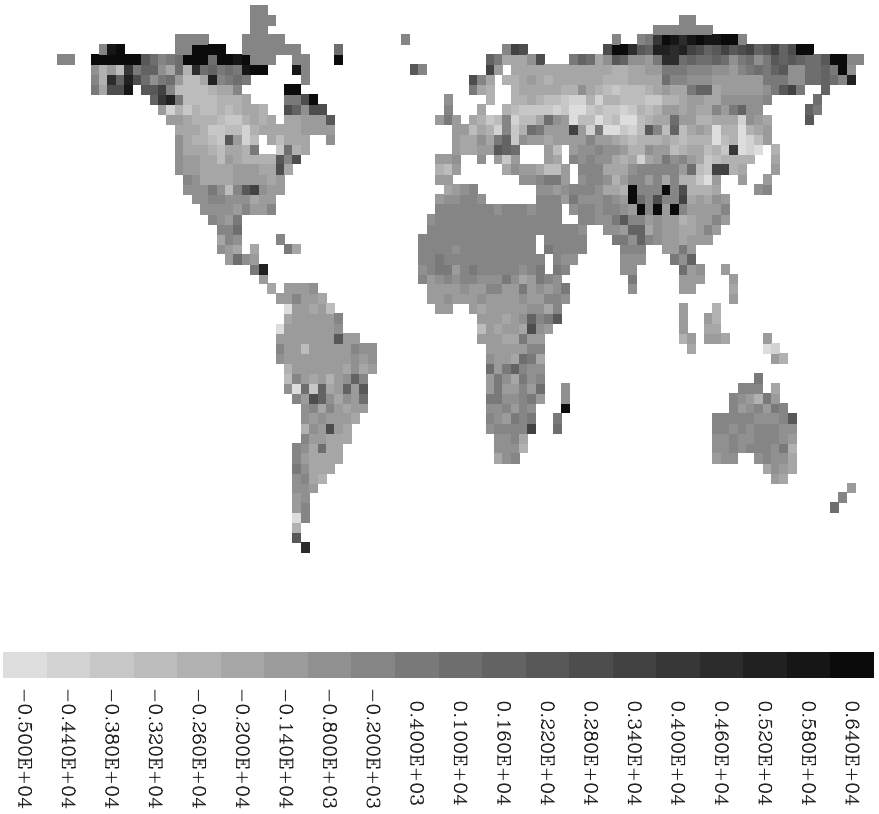

Figure 3.13: Perturbations in the terrestrial carbon storage due to a globally uniform step-like increase in air temperatures by 1° C. Carbon stock anomalies in the new equilibrium are divided into 20 classes, and the legend shows the lowest value of each class in units gC/m^2.

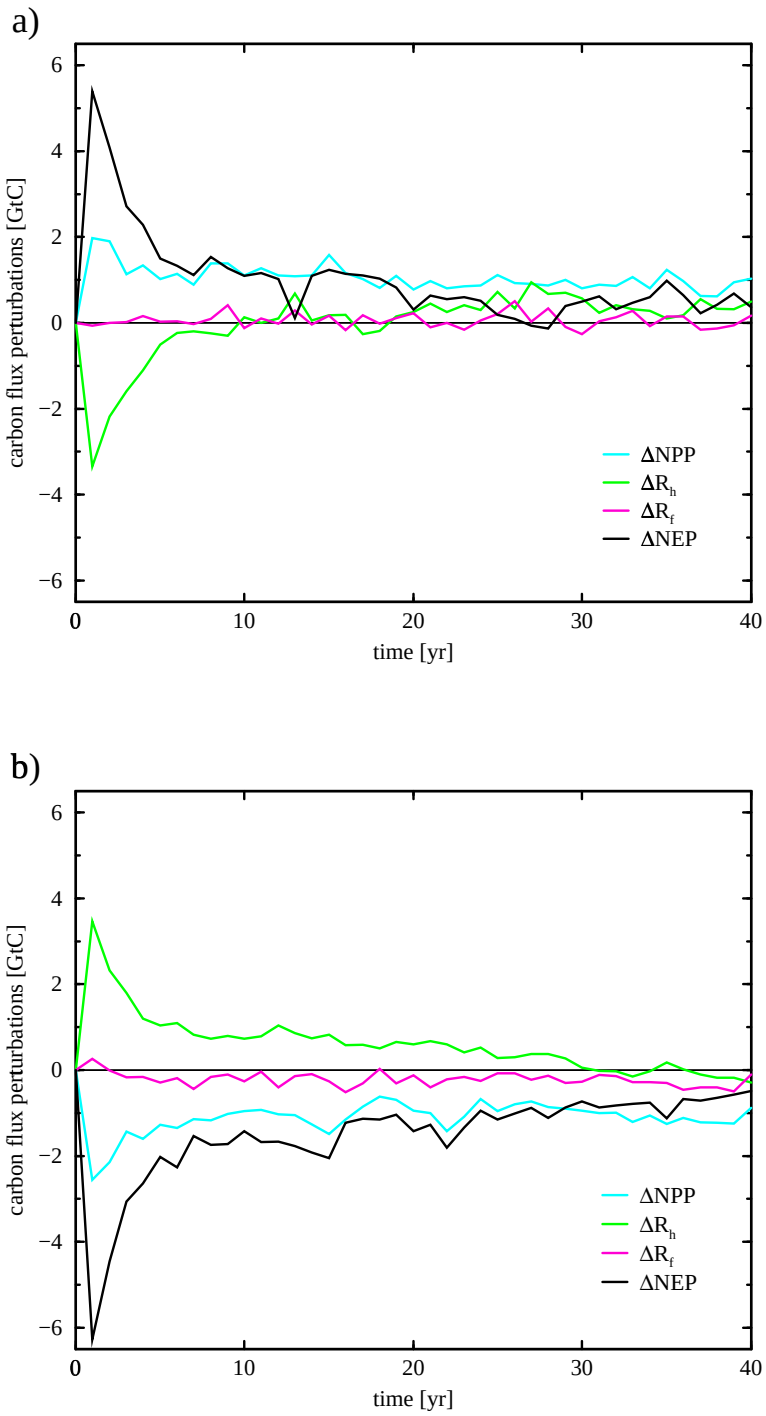

Figure 3.14: Carbon flux perturbations resulting from step-like global air temperature changes by –1° C (a) and +1° C (b), respectively. Blue curves are perturbations in net primary productions, green lines represent heterotrophic respirations, red curves stand for carbon fluxes due to fire, and black curves are the resulting net ecosystem productions.

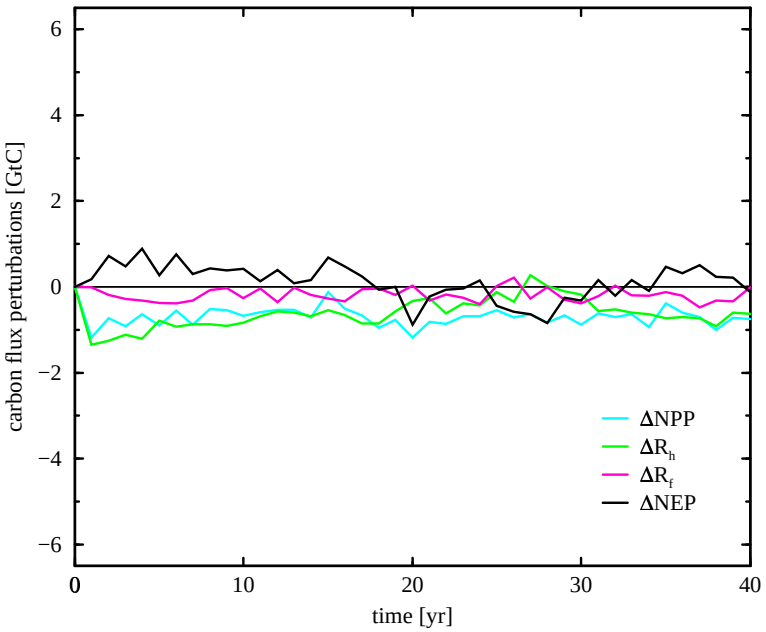

Figure 3.15: Carbon flux perturbations resulting from a step-like global air temperature change by $-1°$ C in the NH and of $+1°$ C in the SH. The blue curve is the perturbation in net primary production, the green line represents heterotrophic respiration, the red curve stands for the carbon flux due to fire, and the black curve is the resulting net ecosystem production.

In order to examine changes in vegetation distribution resulting from the experiment with an instantaneous temperature decrease in the NH and an increase in the SH, spatial coverages of the nine specific PFTs are plotted in figures 3.16, 3.17, and 3.18. Plant type coverages in the new equilibrium (450 years after the temperature perturbation) in comparison to pre-industrial conditions are plotted for latitudinal bands with the LPJ resolution of 2.5°. The vegetated area A_b of a specific latitudinal band b is calculated as follows:

$$A_b = \sum_{grid \subset b} FPC_{grid} \cdot A_{grid} \tag{3.1}$$

where FPC_{grid} is the grid cell foliar projective cover and A_{grid} the appropriate grid cell area.

In general, all plant functional types show a southward shift in both hemispheres after the temperature experiment (NH $-1°$ C, SH $+1°$ C). The reason for this is that temperatures maintaining optimal growing conditions for a certain PFT can be found in lower latitudes (figure 3.11). The global area covered by vegetation ($\sum_b A_b$) is not changed significantly by the temperature perturbation (it is only 1.1% smaller after the changes in temperature).

The geographical distribution of tropical broadleaved evergreen (a) and raingreen trees (b) shows a clear southward trend, whereas the covered area is almost constant (+1% and +3% respectively). The extent of temperate needleleaved evergreen trees (c) is decreasing by 9% after the temperature perturbation, especially between 30° N and 40° N. Decreasing temperatures and a constant water supply are an advantage for temperate deciduous trees in those latitudes, because they can adapt to cold conditions by shedding their leaves during winter, and they partly replace temperate conifers. Another part of temperate needleleaved trees is ruled out by invading boreal plants. Temperate broadleaved trees (d) and (e) show a clear southward trend, and the area of coverage is decreasing by 11% and 6% of the pre-industrial extent, respectively. All types of temperate trees are extremely sensitive to temperature decreases. In contrast to this, boreal trees (f) and (g) can keep their extent after the temperature perturbation (+2% and +1% respectively), and the only effect of the experiment on those PFTs is a displacement to lower latitudes. The distribution of grass PFTs (h) and (i) is mainly depending upon extents and locations of trees. The appropriate geographic patterns show a slight southward shift, and the covered area for C_3 grass decreases by 3%, whereas for warm grass (C_4), it increases by 3%.

The geographical PFT distribution can be examined in figure 3.19. The world maps show the PFTs with the largest foliar projective covers of every grid cell. The atmospheric CO_2 concentration is set to a constant value of 280 ppmv. The upper map shows the results for model spinup temperatures, the lower map shows the vegetation coverage in the new equilibrium after a temperature decrease by 1° C in the northern hemisphere and an increase by 1° C in the southern hemisphere.

Because of the neglect of all PFTs except of the one with the biggest FPC, changes in plant coverage are only visible if the major PFT in a certain grid cell is overruled by another plant type after the temperature perturbation. But a global southward shift can be examined for most of the PFTs, although the displacement to lower latitudes of tropical (1, 2) and of temperate broadleaved trees (4, 5) can hardly be detected. The partial replacement of temperate conifers (3) by temperate deciduous (5) and boreal needleleaved trees (6) can clearly be examined in eastern USA, western Europe, and in China.

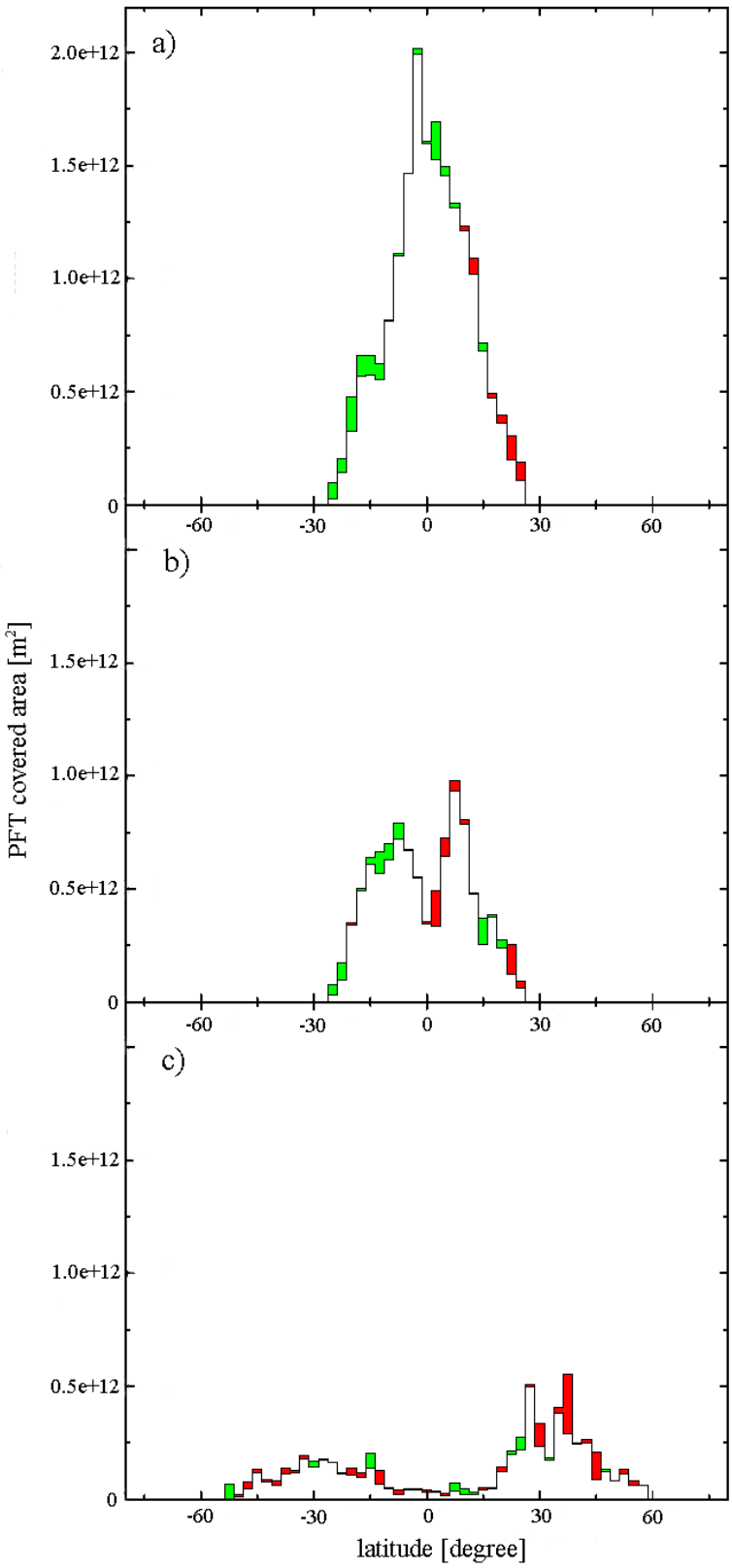

Figure 3.16: Areas covered by (a) tropical broadleaved evergreen, (b) tropical broadleaved raingreen, and (c) temperate needleleaved evergreen trees, resulting from an air temperature step of $-1°$ C in the NH, and $+1°$ C in the SH. Plant coverages (in m^2) are shown for latitudinal bands with a resolution of 2.5°. Green areas represent increased spatial coverage in the new equilibrium, red areas are decreases in vegetation.

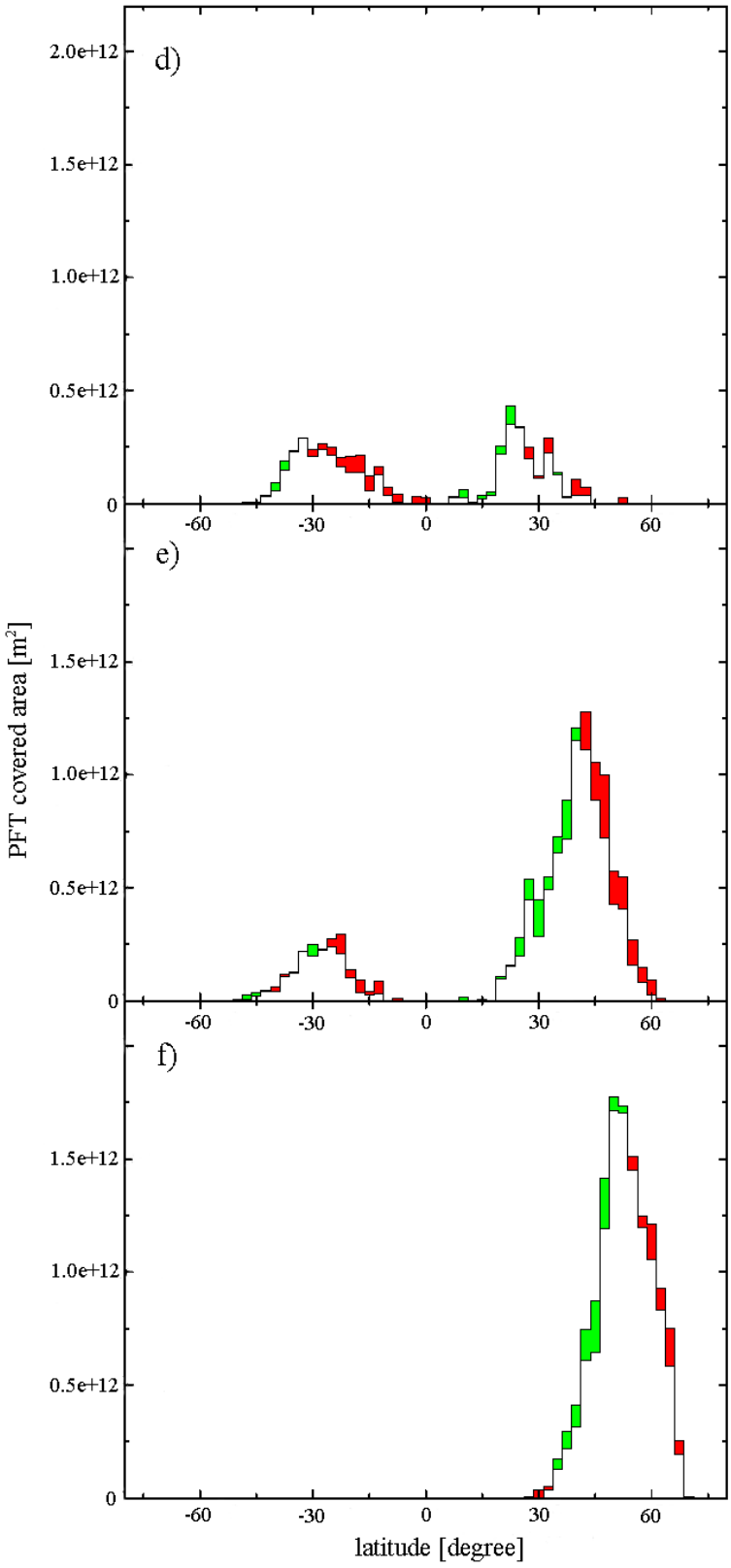

Figure 3.17: Areas covered by (d) temperate broadleaved evergreen, (e) temperate broadleaved summergreen, and (f) boreal needleleaved evergreen trees, resulting from an air temperature step of $-1°$ C in the NH, and $+1°$ C in the SH. Plant coverages (in m^2) are shown for latitudinal bands with a resolution of 2.5°. Green areas represent increased spatial coverage in the new equilibrium, red areas are decreases in vegetation.

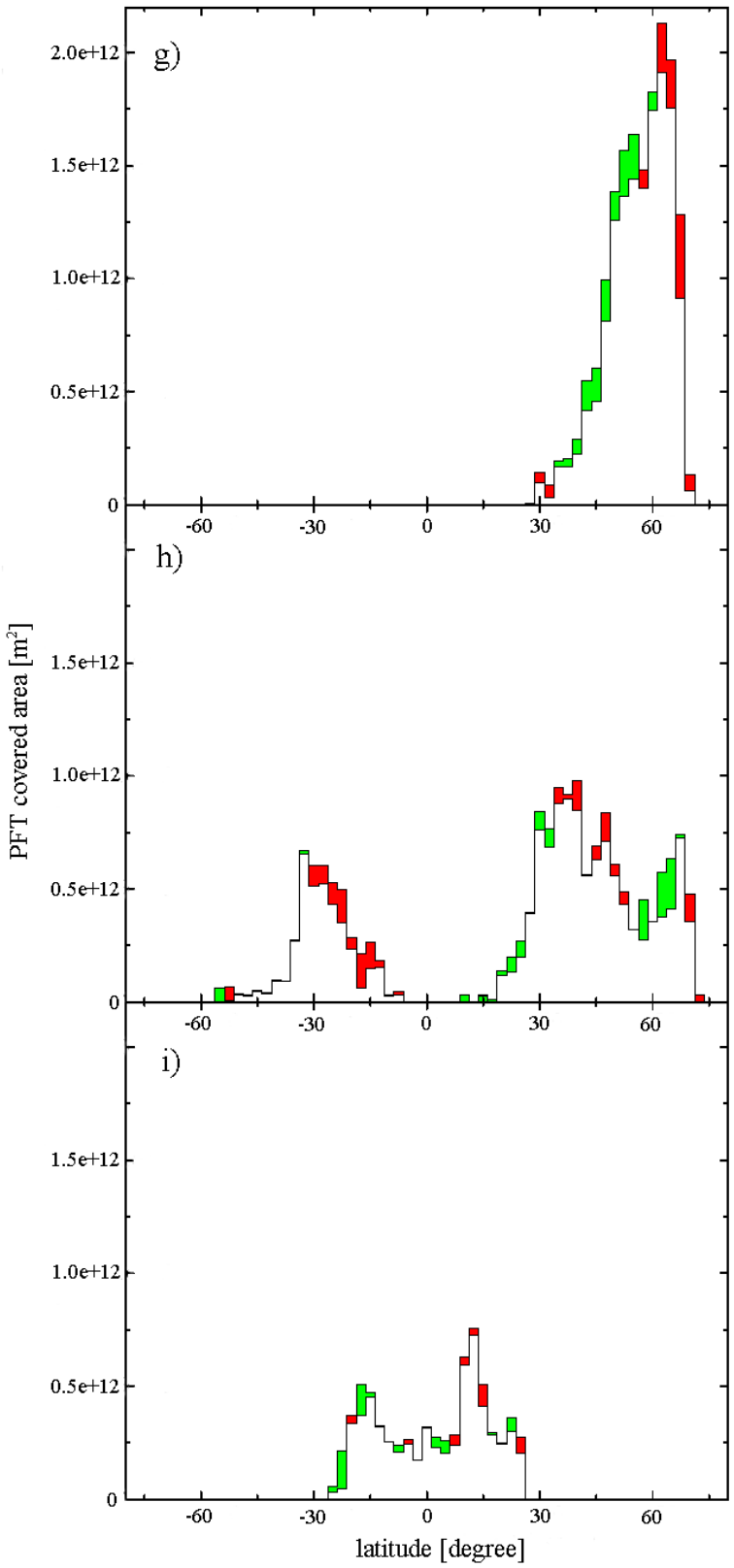

Figure 3.18: Areas covered by (g) boreal summergreen trees, (h) cool grass (C_3), and (i) warm grass (C_4), resulting from an air temperature step of –1° C in the NH, and +1° C in the SH. Plant coverages (in m^2) are shown for latitudinal bands with a resolution of 2.5°. Green areas represent increased spatial coverage in the new equilibrium, red areas are decreases in vegetation.

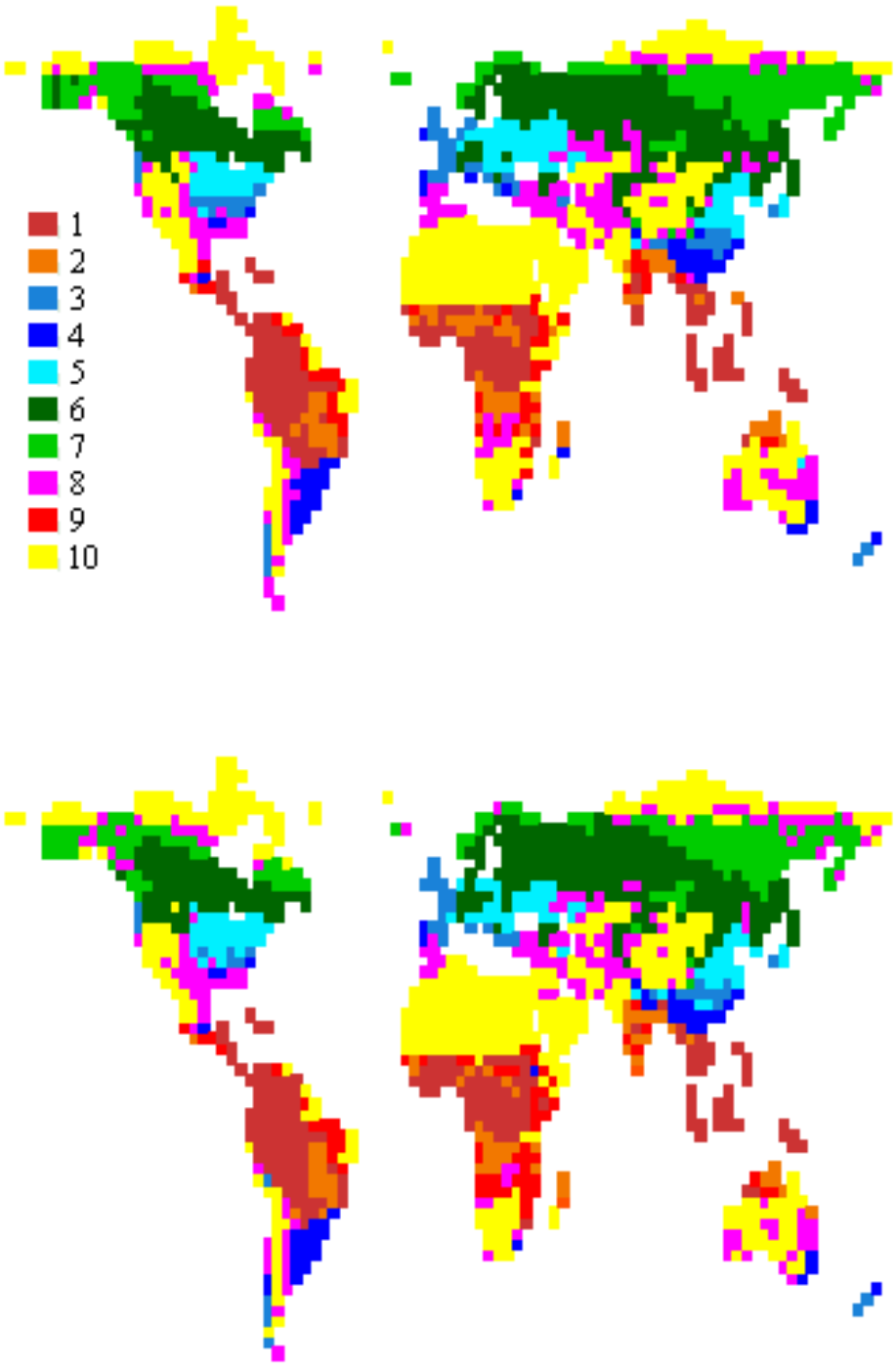

Figure 3.19: Geographical PFT distribution in the new equilibrium after an air temperature step of –1° C in the NH and of +1° C in the SH. Both maps show the major PFT for each grid cell with a constant atmospheric CO_2 concentration of 280 ppmv. For the upper map, the model was forced with baseline air temperatures, the lower map is the result of the temperature perturbation. (1) are tropical broadleaved evergreen trees, (2) tropical broadleaved raingreen trees, (3) temperate needleleaved evergreen trees, (4) temperate broadleaved evergreen trees, (5) temperate broadleaved summergreen trees, (6) boreal needleleaved evergreen trees, (7) boreal summergreen trees, (8) cool grass, (9) warm grass, and (10) bare ground.

3.2.1 Changes in seasonality

Focusing on the seasonality of air temperatures, we change the strength of inter-annual fluctuations in the following model sensitivity tests. Variations in monthly temperatures from the annual mean value are changed by +10% or –10% respectively for every individual grid cell (figure 3.20). This is only done for temperature data according to *Leemans and Cramer* [1991], whereas perturbations in temperatures from a simulation by the Hadley Centre climate model HadCM2-SUL (*Johns et al.* [1997], *Mitchell et al.* [1995]) are not changed. The model spinup is performed with the different temperature seasonalities for 2000 years (as described in section 2.6), until vegetation distribution is in equilibrium. The atmospheric CO_2 concentration is set to a constant value of 280 ppmv.

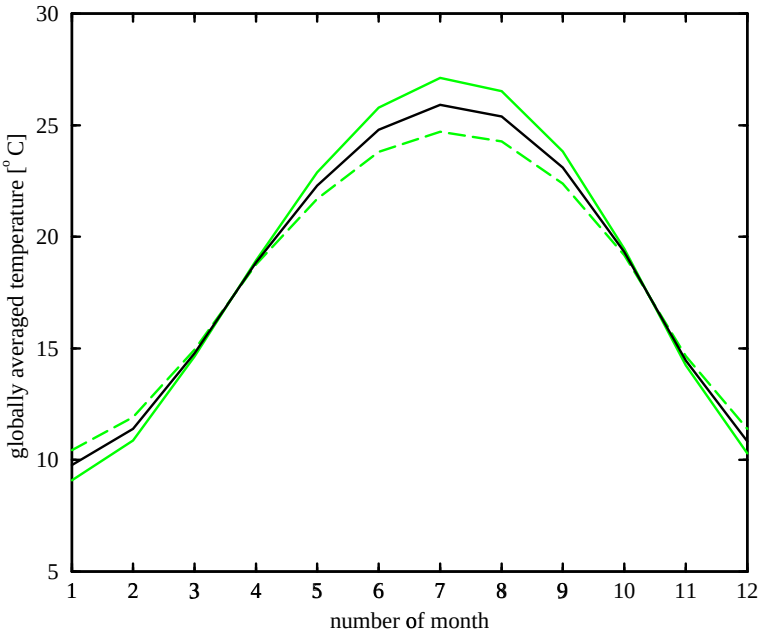

Figure 3.20: Global mean continental temperature seasonality. The black curve represents monthly air temperatures from *Leemans and Cramer* [1991], averaged over all grid cells. For the grey curves, the temperature seasonality is intensified (solid line) or attenuated (dashed line), respectively. This is done by increasing or decreasing temperature variations from the annual mean value by 10% for every grid cell.

The global carbon pool contents change by +22 GtC in the equilibrium with a weaker temperature seasonality and by –66 GtC with a stronger seasonality (table 3.2). On a global scale, the terrestrial carbon inventory is increased by 0.87% under decreased seasonality, but it is more sensitive to increasing seasonality (–2.62%) because of the significant temperature stress for most PFTs.

carbon pool	C_{spinup} [GtC]	C_{-10} [GtC]	C_{+10} [GtC]	ΔC_{-10} [%]	ΔC_{+10} [%]
vegetation	869	872	864	0.35	-0.58
litter above ground	113	114	110	0.88	-2.65
litter below ground	82	84	78	2.44	-4.88
fast soil organic matter	1002	1013	965	1.10	-3.69
slow soil organic matter	450	455	433	1.11	-3.78
sum of all pools	2516	2538	2450	0.87	-2.62

Table 3.2: Carbon uptake of the five pools after a change in seasonality by -10% or +10%, respectively. C_{spinup} are the carbon inventories in the equilibrium after the model spinup, $C_{\mp 10}$ are the C stocks in the equilibrium with weaker or stronger seasonality respectively, and the differences between $C_{\mp 10}$ and C_{spinup} are plotted as $\Delta C_{\mp 10}$ in percents of the baseline inventory.

In order to evaluate the dependency of vegetation dynamics on temperature seasonality, we examine geographical plant distributions with a decreased or increased temperature seasonality, respectively (figures 3.21 and 3.22). The world maps show the major PFT for each grid cell with a constant atmospheric CO_2 concentration of 280 ppmv. For the upper map in both figures, the model is forced with the spinup climatology described in section 2.6, for the lower maps, temperature seasonality is weaker (3.21) or stronger (3.22) by 10% for every grid cell.

As expected, the biggest changes in vegetation resulting from variations in temperature seasonality can be observed in mid- to high latitudes. In tropical regions, plant coverages are almost independent of seasonality perturbations, because in those latitudes, air temperatures only vary little throughout the year, and plants are not temperature stressed at all. In northern high latitudes, boreal conifers (6) partly rule out boreal and temperate deciduous trees with a weaker seasonality, whereas summergreen trees dominate boreal regions with increased interannual temperature variations. The reason for a decreased extent of boreal conifers with a decreased temperature seasonality (and the opposite effect for an increased seasonality) is that the mean temperature of the coldest month in a year has to be between –32 and –2° C, and the mean temperature of the warmest month has to be 23° C or warmer (see table of bioclimatic limits on page 12) in order that boreal conifers are able to regenerate. Under a weaker temperature seasonality, these conditions are fulfilled during most of the years, whereas an increased seasonality favors the growth of summergreen trees in the appropriate regions, because they are less sensitive to cold winter temperatures.

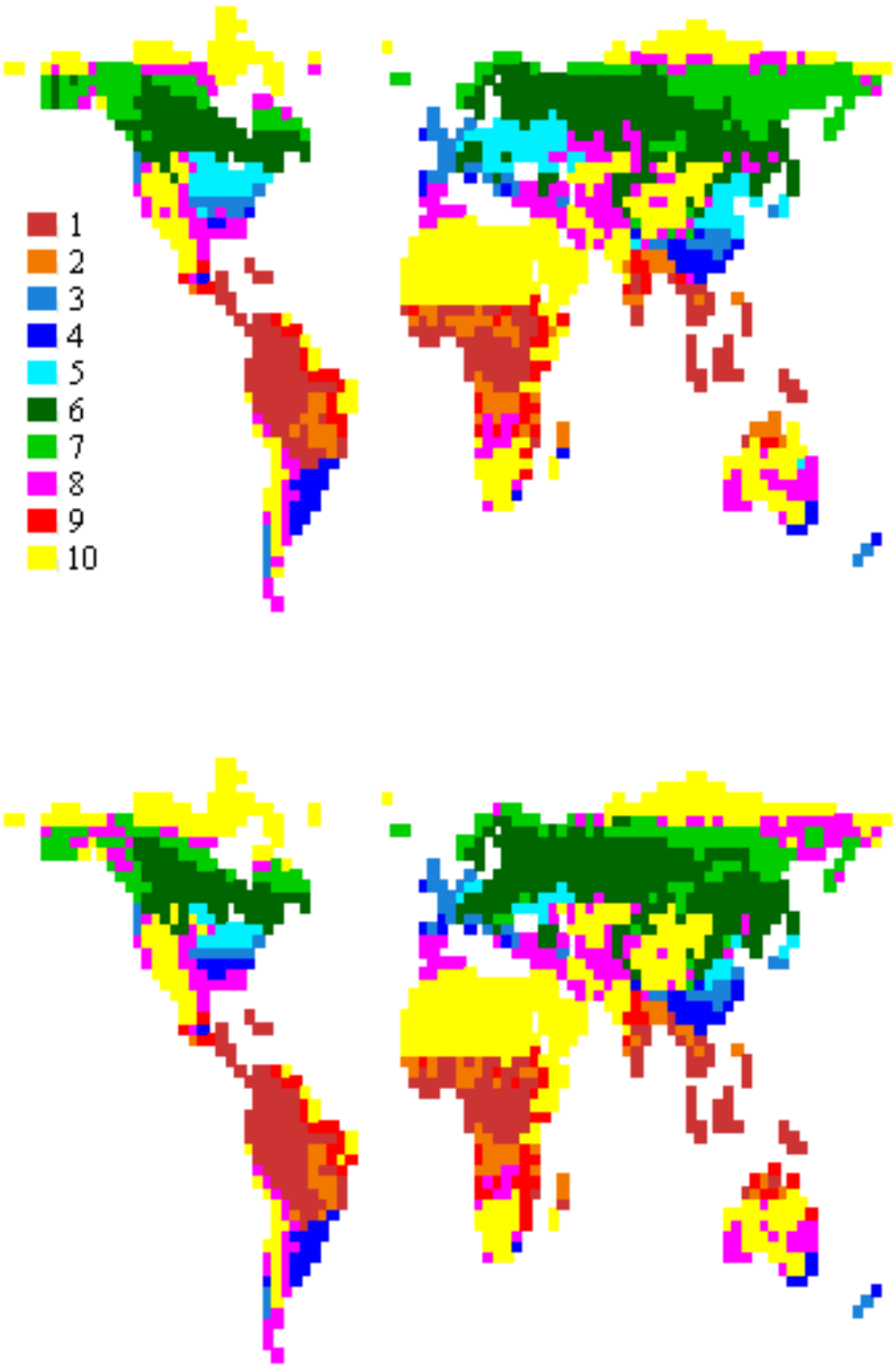

Figure 3.21: Geographical PFT distribution in the new equilibrium after a decrease in temperature seasonality by 10%. Both maps show the major PFT for each grid cell with a constant atmospheric CO_2 concentration of 280 ppmv. For the upper map, the model is forced with the spinup climatology described in section 2.6, for the lower map, temperature seasonality is decreased by 10% for every grid cell. (1) are tropical broadleaved evergreen trees, (2) tropical broadleaved raingreen trees, (3) temperate needleleaved evergreen trees, (4) temperate broadleaved evergreen trees, (5) temperate broadleaved summergreen trees, (6) boreal needleleaved evergreen trees, (7) boreal summergreen trees, (8) cool grass, (9) warm grass, and (10) bare ground.

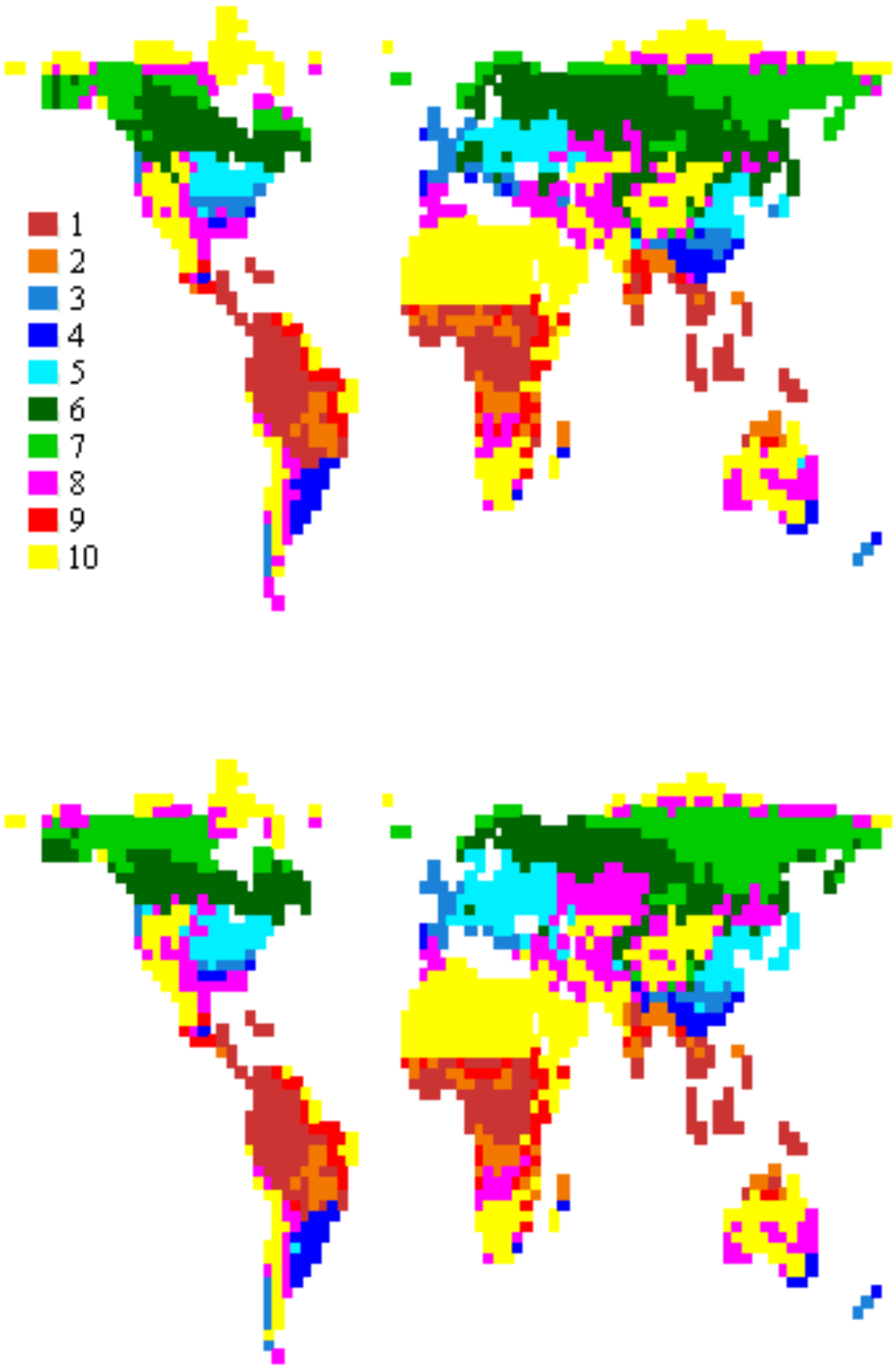

Figure 3.22: Geographical PFT distribution in the new equilibrium after an increase in temperature seasonality by 10%. Both maps show the major PFT for each grid cell with a constant atmospheric CO_2 concentration of 280 ppmv. For the upper map, the model is forced with the spinup climatology described in section 2.6, for the lower map, temperature seasonality is increased by 10% for every grid cell. (1) are tropical broadleaved evergreen trees, (2) tropical broadleaved raingreen trees, (3) temperate needleleaved evergreen trees, (4) temperate broadleaved evergreen trees, (5) temperate broadleaved summergreen trees, (6) boreal needleleaved evergreen trees, (7) boreal summergreen trees, (8) cool grass, (9) warm grass, and (10) bare ground.

Decreasing extents of boreal conifers under a stronger temperature seasonality result in generally decreasing terrestrial carbon storage in the USA and in Eurasia (figure 3.23). In northern high latitudes, where boreal summergreen trees and C_3 grass are invading taiga regions, the terrestrial storage increases.

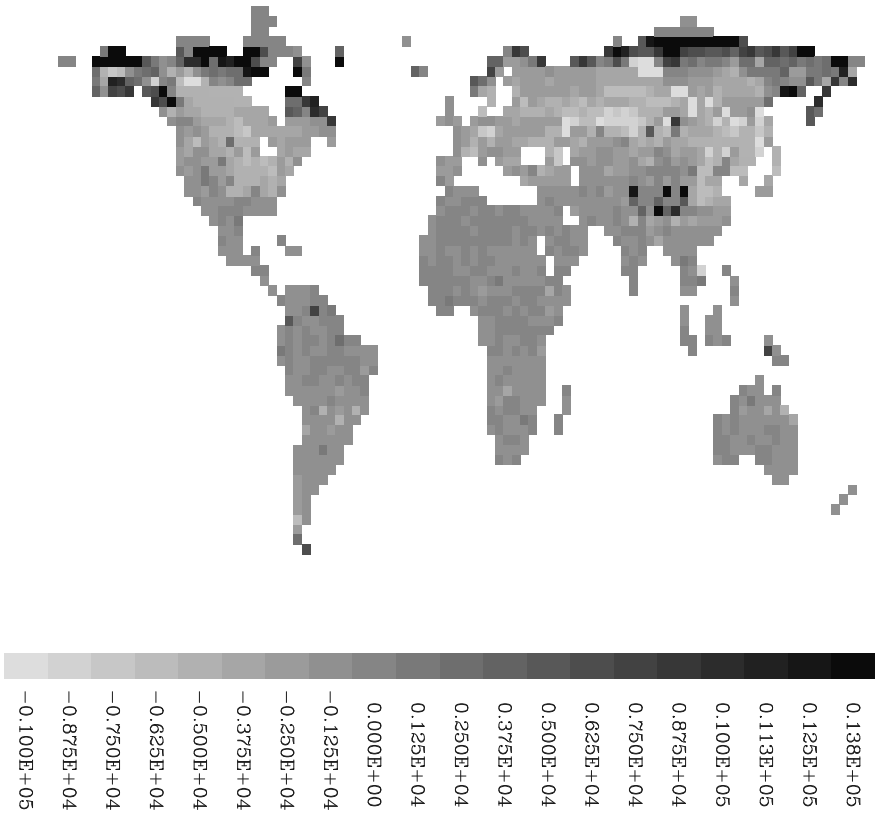

Figure 3.23: Perturbations in the terrestrial carbon storage due to a global increase in air temperature seasonality by 10%. Carbon stock anomalies in the new equilibrium are divided into 20 classes, and the legend shows the lowest value of each class in units gC/m^2.

3.3 Precipitation variations

In a similar way as temperature values, precipitation input data P_{spinup} of the LPJ-DGVM are made up of a baseline climatology of *Leemans and Cramer* [1991] with monthly mean values, and of additional interannually variable climate data (see section 2.6). In order to examine the reaction of the model to variations in precipitation, it is run until it reaches a baseline equilibrium state, and then precipitation is instantaneously increased or decreased by 20%, respectively. Rain- and snowfall

should not be changed by a globally constant value as this was done with temperatures, because this scenario would not be realistic for regions with extremely low annual precipitation values.

After a global precipitation perturbation by +20%, the terrestrial carbon inventory increases by 100 GtC in the new equilibrium which is reached after approximately 400 years (figure 3.24). If precipitation is reduced by 20%, the carbon stock decreases by 130 GtC. Those results show that the reduction in carbon uptake of the terrestrial biosphere resulting from decreasing water supply is relatively larger than the enhanced carbon storage due to an increased precipitation level.

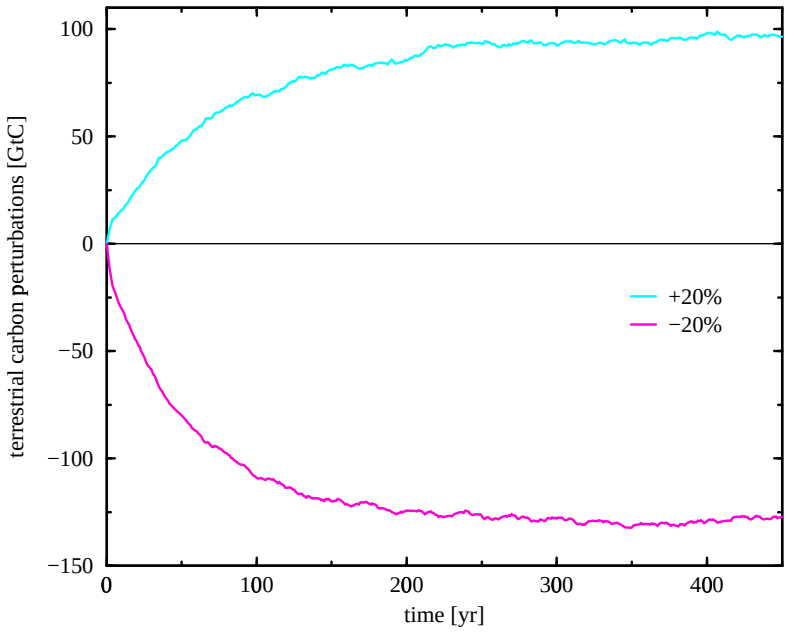

Figure 3.24: Perturbations in terrestrial carbon inventories due to precipitation variations. The blue curve represents a global precipitation increase by 20%, and the red line a decrease by 20%.

Resulting from an increase in rain- and snowfall, ΔNPP increases and stabilizes at about 5 GtC/yr in the new equilibrium (figure 3.25). Perturbations in heterotrophic respiration are as high as ΔNPP after less than 100 years. As expected, the carbon flux R_f due to fire increases with more precipitation, but it returns to the baseline state as soon as the soil water is on a normal level again due to an enhanced vegetation coverage. Qualitatively, effects of decreased precipitation to carbon fluxes are directly opposed, but changes in carbon fluxes are larger than under enhanced rain- and snowfall.

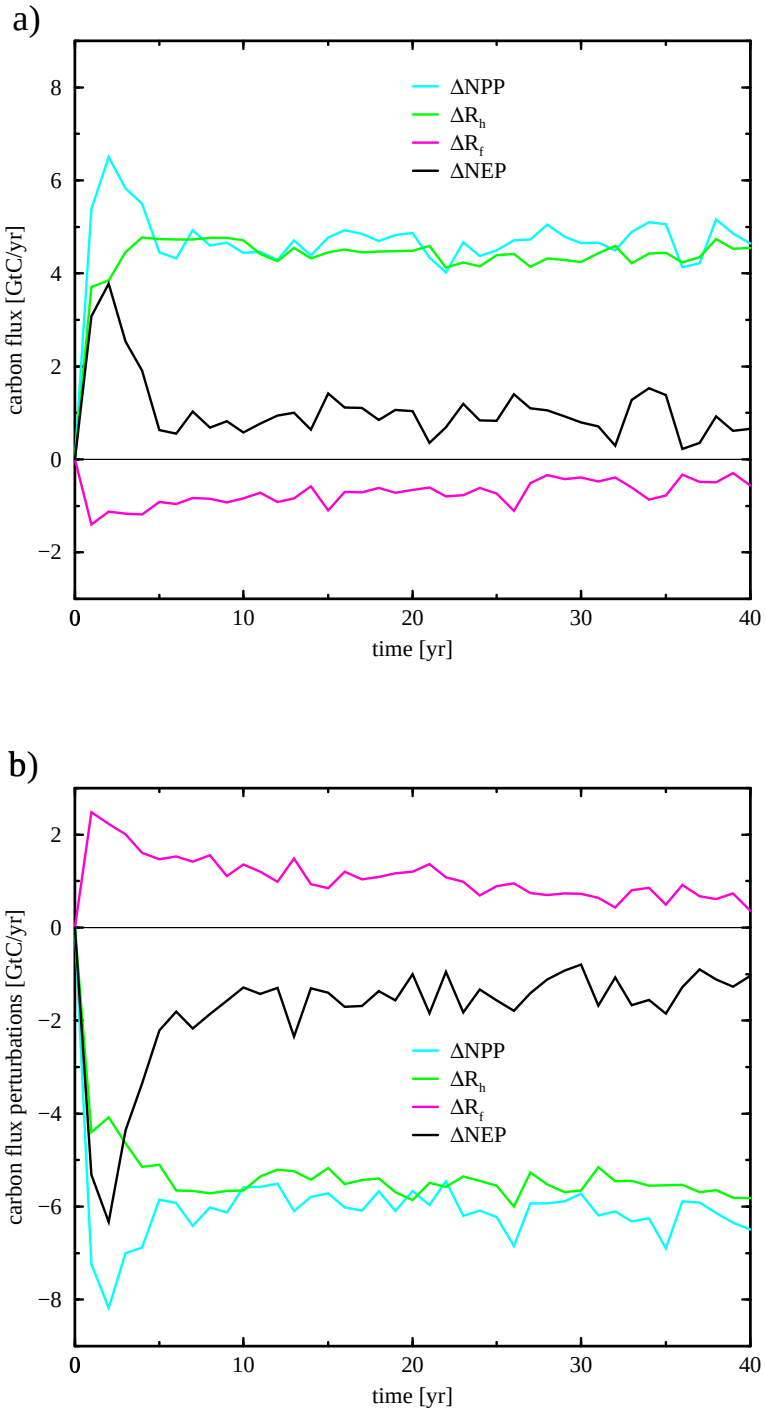

Figure 3.25: Carbon flux perturbations resulting from an increase (a) or decrease (b) in precipitation by 20%. Blue curves represent net primary productions NPP, green lines are heterotrophic respirations R_h, red curves stand for carbon fluxes R_f due to fire, and black curves are net ecosystem productions NEP.

Next, the sensitivity of terrestrial carbon storage to changes in precipitation is analyzed in detail. The LPJ model is forced with precipitation data increased or decreased by 2, 8, 14, and 20% respectively, and perturbations in terrestrial carbon inventories are examined (figure 3.26). Carbon storage shows a slightly stronger sensitivity to precipitation decreases than to increases, but apart from this effect, the dependence of terrestrial carbon inventories to changes in precipitation is approximately linear. According to *Voss and Mikolajewicz* [1999], precipitation changes by 2.42% for temperature variations by 1° C, and *Hulme et al.* [1998] predicts precipitation sensitivity to be 2.37%/° C. Combining those informations, the terrestrial carbon storage decreases by approximately 15 GtC for a temperature decrease by 1° C.

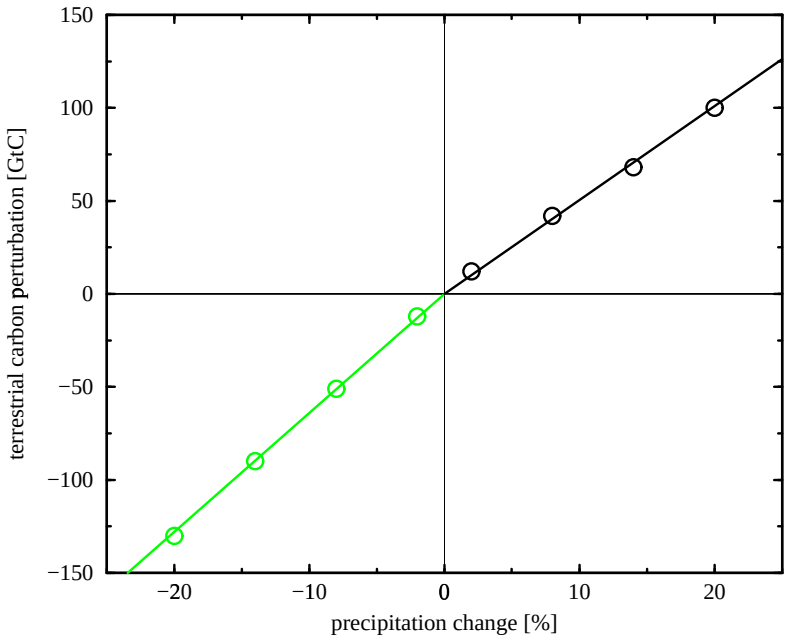

Figure 3.26: Perturbations in terrestrial carbon storage resulting from changes in precipitation. Black circles result from simulation with increased precipitation, gray circles represent decreases in precipitation. Solid lines are linear regressions of the model results.

The vegetation distribution after a global precipitation decrease by 20% is plotted in figure 3.27. The dominating plant functional type of each grid cell is plotted, whereas the model is forced with baseline data for atmospheric CO_2 concentrations and air temperatures. For the upper map, precipitation data by *Leemans and Cramer* [1991] are used, the lower map shows the vegetation coverage in the new equilibrium after a precipitation decrease by 20%.

Most plant functional types do not significantly change their geographical distribution due to lower precipitation except of a partial displacement of tropical raingreen by evergreen trees. The major effect after decreased rain- and snowfall are globally enhanced extents of deserts, because the water stress of plants growing in border regions of deserts becomes too strong after the precipitation decrease. Again, it has to be taken into account that the maps in figure 3.27 only show the PFT with the biggest foliar projective cover for each grid cell. Because of this simplification, changes in vegetation coverage are only displayed if the major plant type is another one after the precipitation decrease.

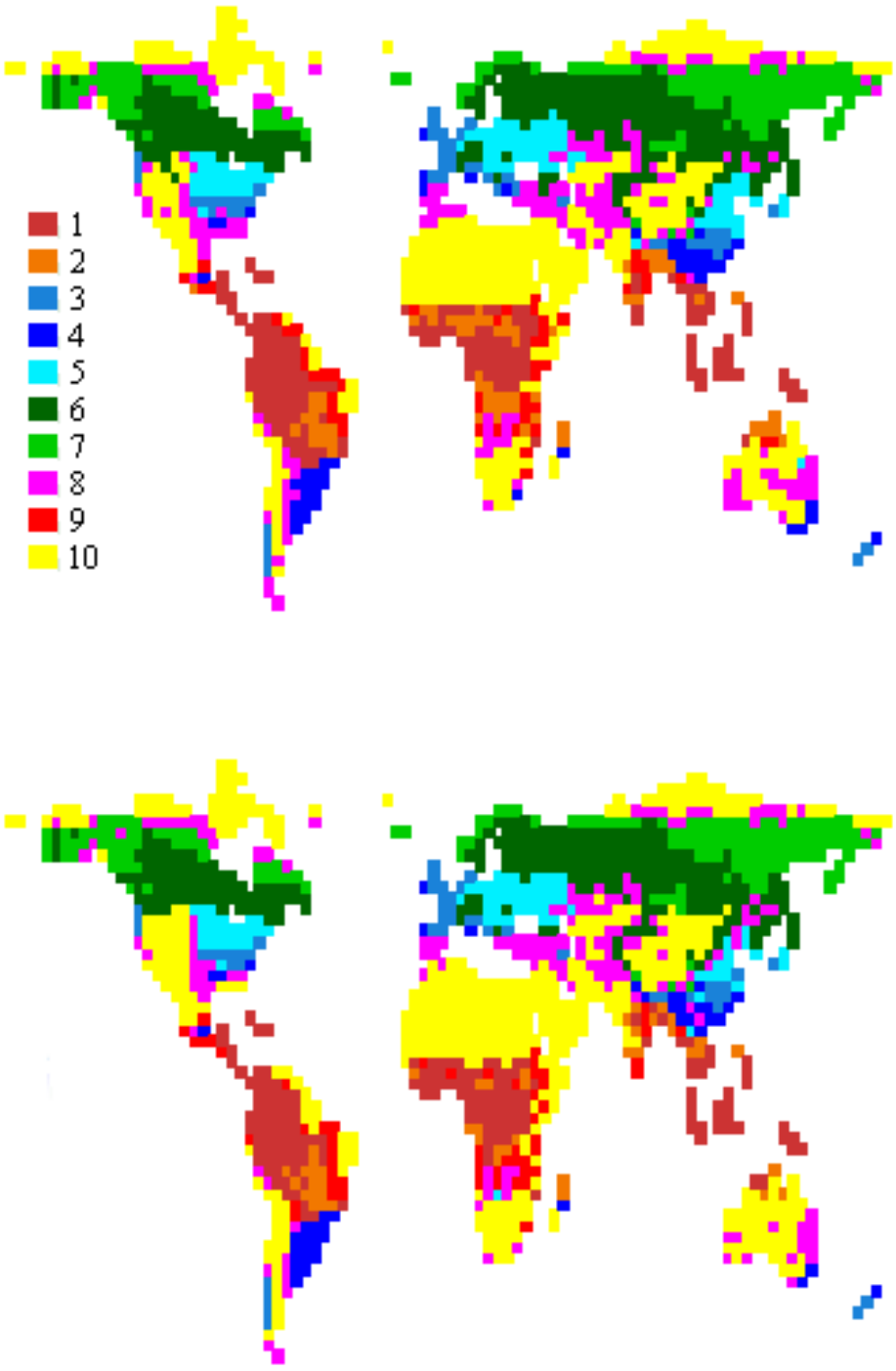

Figure 3.27: Geographical PFT distribution in the new equilibrium after a global precipitation decrease by 20%. Both maps show the major PFT for each grid cell with a constant atmospheric CO_2 concentration of 280 ppmv and baseline temperature forcing. For the upper map, precipitation data by *Leemans and Cramer* [1991] are used, the lower map shows the vegetation coverage in the new equilibrium after a precipitation decrease by 20%. (1) are tropical broadleaved evergreen trees, (2) tropical broadleaved raingreen trees, (3) temperate needleleaved evergreen trees, (4) temperate broadleaved evergreen trees, (5) temperate broadleaved summergreen trees, (6) boreal needleleaved evergreen trees, (7) boreal summergreen trees, (8) cool grass, (9) warm grass, and (10) bare ground.

Chapter 4

Terrestrial carbon storage over the last 500 years

CO_2 data reconstructed from Law Dome ice cores [*Etheridge et al.*, 1996] show that the level of CO_2 dropped by about 6 ppmv around 1550, and stayed low until about 1850. This period is around the time of reported low temperatures in Europe is often referred to as "Little Ice Age" (LIA) [*Grove*, 1988]. It should be pointed out that there is no consensus on when the LIA began or ended, and there is no evidence in temperature records of a worldwide, synchronous and prolonged cold interval [*Jones and Bradley*, 1992]. *Grove* [1988] estimates that the observed temperature decrease in parts of Europe was about 1–2° C, with frequent fluctuations rather than sustained cool temperatures.

In this chapter, we examine the hypothesis that the relatively low atmospheric CO_2 level between 1550 and 1850 was caused by an enhanced terrestrial storage. This assumption is confirmed by increased $\delta^{13}C$ values during the seventeenth and eighteenth centuries [*Trudinger et al.*, 1999]. By solving the atmospheric budget equations for CO_2 and $\delta^{13}C$ for the unknown global fluxes into the terrestrial biosphere (*double deconvolution*), the additional terrestrial storage is assumed to be about 40 GtC [*Joos et al.*, 1999] (figure 4.1).

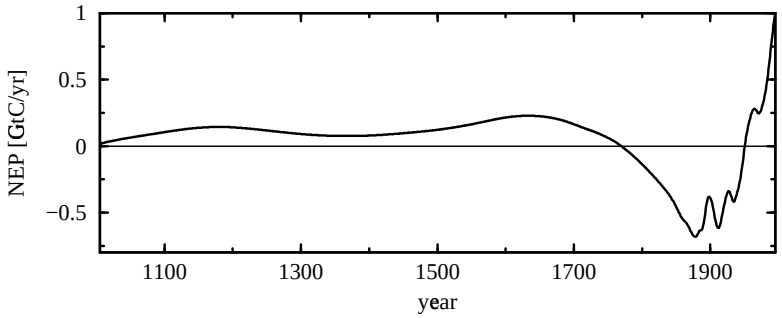

Figure 4.1: Net ecosystem production obtained by solving the atmospheric budget equations for CO_2 and $\delta^{13}C$ for the unknown global fluxes into the terrestrial biosphere [*Joos et al.*, 1999].

4.1 Data

4.1.1 CO_2 data

In this study, simulations are performed with two different CO_2 data sets (figure 4.2). Atmospheric concentrations (a) from 1006 to 1997 A.D. are values obtained from air bubbles entrapped in ice cores and direct atmospheric measurements. The three ice cores used for data reconstruction, DE08, DE08-2, and DSS, are situated in Law Dome, Antarctica, and they provide CO_2 values until 1978 [*Etheridge et al.*, 1996]. Those data overlap with the atmospheric record from measurements at South Pole [*Keeling*, 1991]. Panel (b) shows atmospheric CO_2 concentrations from the year 914 to 1992. The data points are a combination of reconstructions from the Antarctic ice cores D47 and D57, South Pole, and Siple, and of direct atmospheric measurements in Mauna Loa, Hawaii (*Barnola et al.* [1995], *Neftel et al.* [1982], *Neftel et al.* [1994], *Siegenthaler et al.* [1988]). Both data sets are spline fitted (appendix C) using cutoff periods of 300 years prior 1850 and of 40 years afterwards, resulting in evolutions $CO_2(a, b)$ [*Joos et al.*, 1999].

Atmospheric CO_2 was approximately constant at 280 ppmv during the last millennium, before it decreased to a relatively lower level during the seventeenth and eighteenth centuries. Since the beginning of the industrial period in the nineteenth century, concentrations rapidly increased to reach 366.7 ppmv in 1998 due to anthropogenic emissions such as fossil fuel burning, changes in land use, and deforestation.

For the LPJ experiments, spline fitted atmospheric concentrations $CO_2(a, b)$ from the year 1515 to 1980 are used as model input data for simulations with changing CO_2 concentrations (figure 4.3). An important distinction between the two data sets are the different evolutions between 1550 and 1850. While concentrations reconstructed from Law Dome ice cores $CO_2(a)$ decreased by up to 6 ppmv relative to pre-industrial values during this time period, data $CO_2(b)$ only decreased by 2 ppmv around the year 1700. This difference points to fundamental uncertainties in highly resolved reconstructions of pre-industrial atmospheric CO_2 concentrations. Analytical uncertainties for CO_2 reconstructions of the appropriate time period are ± 1.2 ppmv according to *Etheridge et al.* [1996]. Probable explanations for distinctions between different ice core analyses are analytical or dating uncertainties, or drilling locations with CO_2 histories which are not representative for global concentrations. In this study, simulations are performed with both data sets $CO_2(a, b)$ to examine the influence of uncertainties in atmospheric concentrations on the terrestrial carbon uptake.

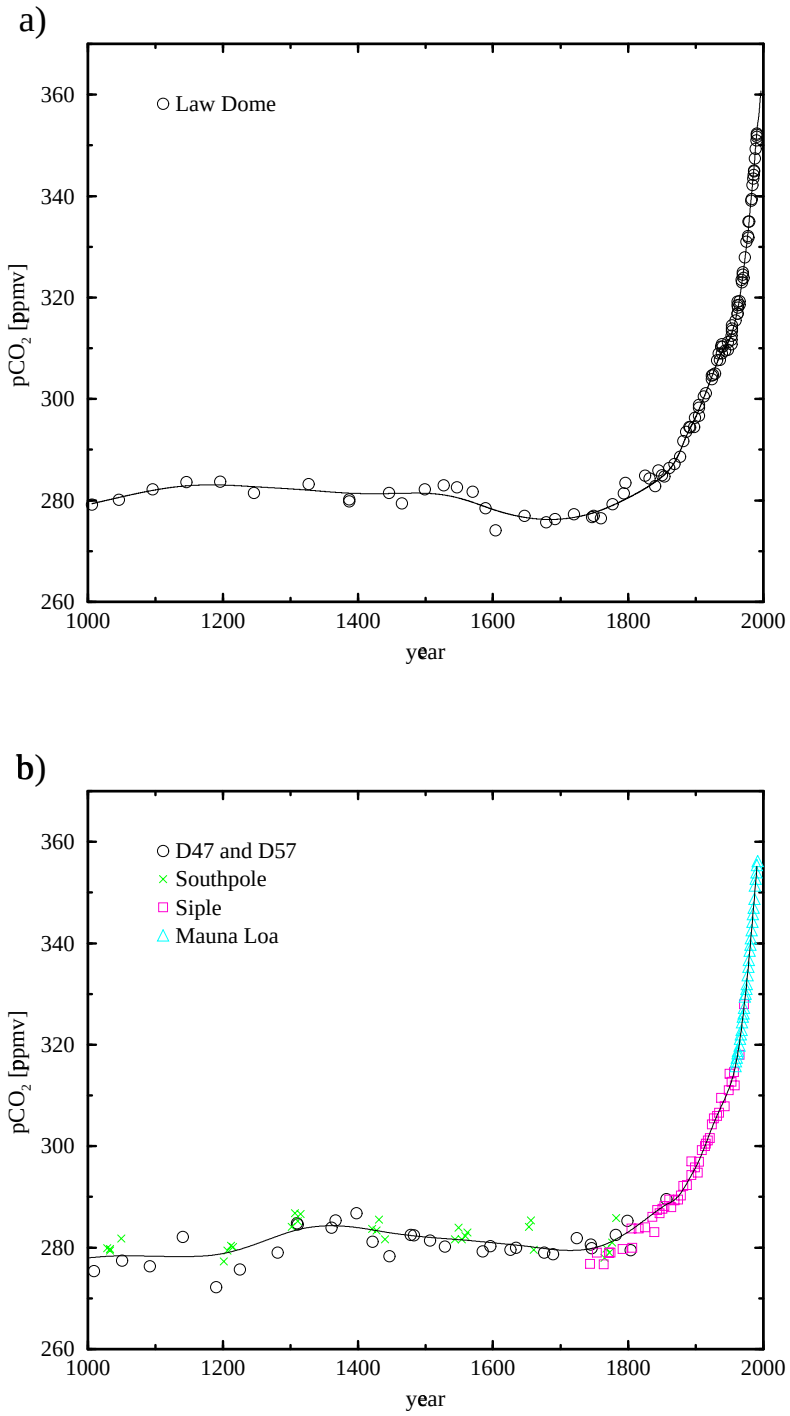

Figure 4.2: Two sets of atmospheric CO_2 concentrations reconstructed from air bubbles entrapped in Antarctic ice cores and from direct measurements. (a) Atmospheric data are obtained from ice cores DE08, DE08-2, and DSS (situated in Law Dome, Antarctica) [*Etheridge et al.*, 1996], and from direct measurements at south pole [*Keeling*, 1991]. (b) CO_2 data are obtained from ice cores D47 and D57 (Adelie Land), South Pole, and Siple, and from monthly atmospheric measurements taken at Mauna Loa (Hawaii) (*Barnola et al.* [1995], *Neftel et al.* [1982], *Siegenthaler et al.* [1988], *Neftel et al.* [1994]). Both data sets are spline fitted using cutoff periods of 300 years prior 1850 and of 40 years afterwards, resulting in evolutions $CO_2(a, b)$ (solid lines) [*Joos et al.*, 1999].

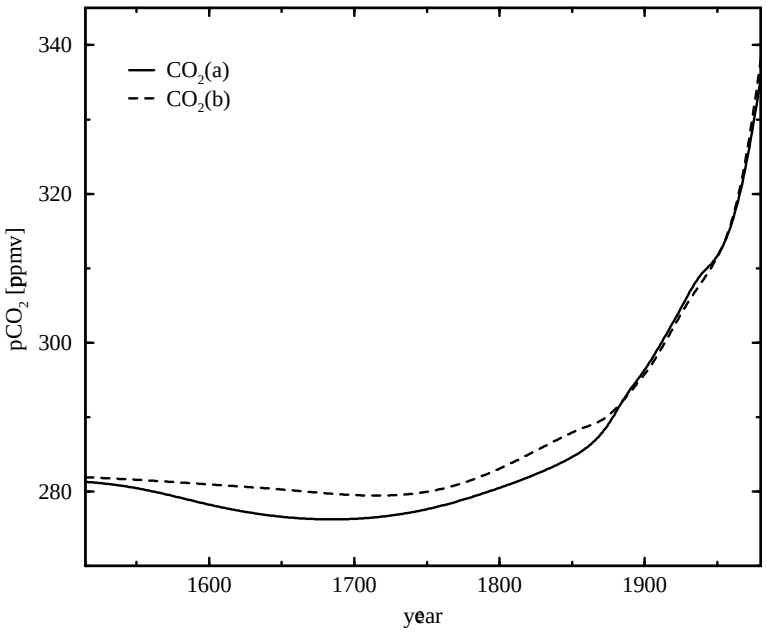

Figure 4.3: Atmospheric data sets $CO_2(a)$ and $CO_2(b)$, respectively. Values from the year 1515 to 1980 are used as input data for simulations in this study.

4.1.2 Temperature data

A set of spatially resolved air temperatures is used for LPJ simulations. The distribution of land, air and sea surface temperature gridpoint data available from 1902 onward are plotted in the upper map in figure 4.4, indicated by shading [*Mann et al.*, 1998]. The squares mark gridpoints with nearly continuous records extending back to 1854 that are used for verification. Temperature data were obtained using a multiproxy network consisting of widely distributed high-quality annually resolved proxy climate indicators, individually collected and formerly analyzed by many paleoclimate researchers. The network includes a collection of annual-resolution dendroclimatic, ice core, ice melt, and coral records, combined with long instrumental records. The lower map shows available temperature data applied to the finer resolution of the LPJ model by linear interpolation. In doing so, temperatures are only calculated for grid points completely surrounded by data of *Mann et al.* [1998].

The main problem by using those temperature data is the occurrence of notable spatial gaps in Canada and Greenland, South America, Africa, Russia, China, and Australia. The data network covers portions of the globe significant enough to maintain reliable temperature patterns if oceanic grid cells are considered, but because

LPJ model simulations are limited to land areas, temperature values are only available for 47% of the 1631 continental grid cells. Especially missing data in tropical regions are a big problem.

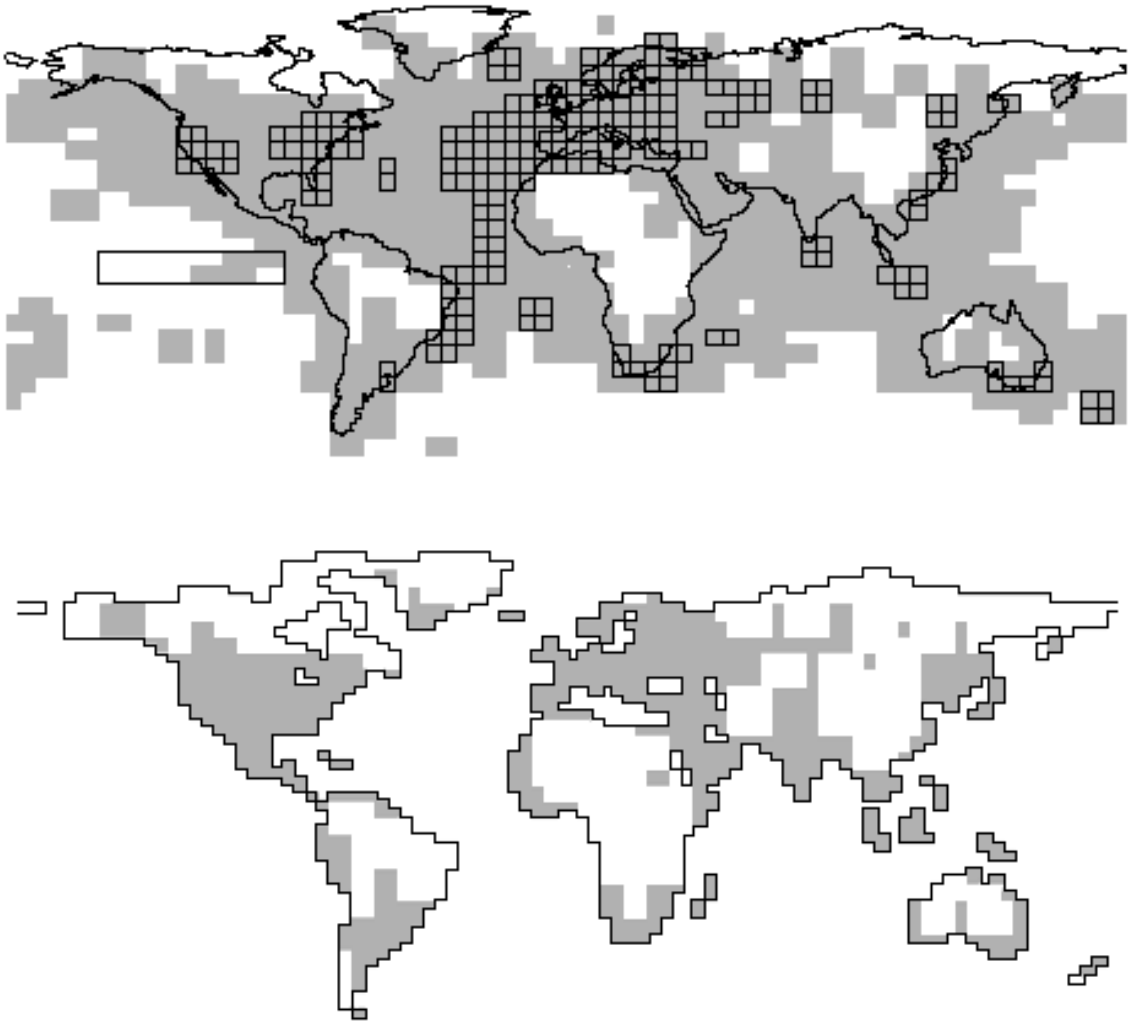

Figure 4.4: Upper panel: Distribution of the 1082 available land air and sea surface temperature gridpoint data from 1902 onward indicated by shading [*Mann et al.*, 1998]. The squares indicate the subset of 219 gridpoints with nearly continuous records extending back to 1854 that are used for verification.
Lower panel: Grid points with available temperature data by *Mann et al.* [1998] applied to the resolution of the LPJ model by linear interpolation (shaded areas). Temperature values are only available for 47% of the 1631 continental grid cells.

In order to reconstruct spatially resolved temperature evolutions, the dominant patterns of the instrumental surface temperature data are isolated by *Mann et al.* [1998] with empirical orthogonal function analysis (see appendix B). EOF analysis provides a natural smoothing of the temperature field in terms of a small number of dominant

patterns of variability or *empirical eigenvectors*. Each of these eigenvectors is associated with a characteristic spatial pattern or *empirical orthogonal function* EOF and its characteristic evolution in time or *principal component* PC. The ranking of the eigenvectors orders the fraction of variance they describe in the multivariate data during the calibration period. The first five of these eigenvectors describe a fraction of 93% of the global mean temperature variations, and 85% of the northern hemisphere mean variations. The first eigenvector, associated with the significant global warming trend of the past century, describes 88% of the variability in the global mean. The second eigenvector is the dominant ENSO-related component, describing 41% of the variance in the NINO3 index. This eigenvector shows a modest cooling trend in the eastern tropical Pacific, which opposes warming in the same region associated with the global warming pattern of the first eigenvector (figure 4.5) [*Mann et al.*, 1998].

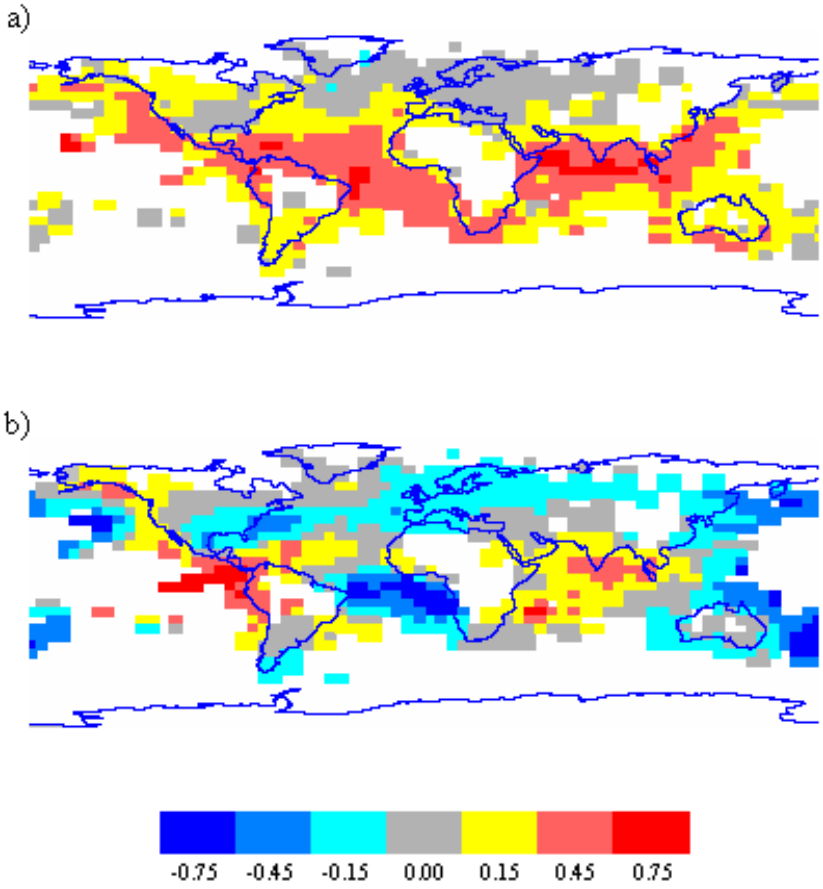

Figure 4.5: Empirical orthogonal functions for the two leading eigenvectors of the global temperature data from 1902-1980 (calibration period). (a) shows the pattern of the first, (b) of the second EOF, respectively. The gridpoint areal weighting factor has been removed from the EOFs so that relative temperature anomalies can be inferred from the patterns [*Mann et al.*, 1998].

The temporal evolutions of the first five eigenvectors are plotted in figure 4.6. The zero line corresponds to the 1902-1980 calibration mean of the quantity. The positive trend in the first PC during the twentieth century is clearly exceptional in the context of the long-term variability in the associated eigenvector, and indeed describes much of the unprecedented warming trend evident in the reconstruction of northern hemisphere temperatures. The negative trend in PC no.2 during the past century is also anomalous in the context of the longer-term evolution of the associated eigenvector. The recent negative trend is associated with a pattern of cooling in the eastern tropical Pacific which may be modulating negative feedback on global warming. PC no.5 shows notable multidecadal variability throughout both the modern and pre-calibration interval, associated with a wavelike trend of warming and subsequent cooling of the North Atlantic this century [*Mann et al.*, 1998].

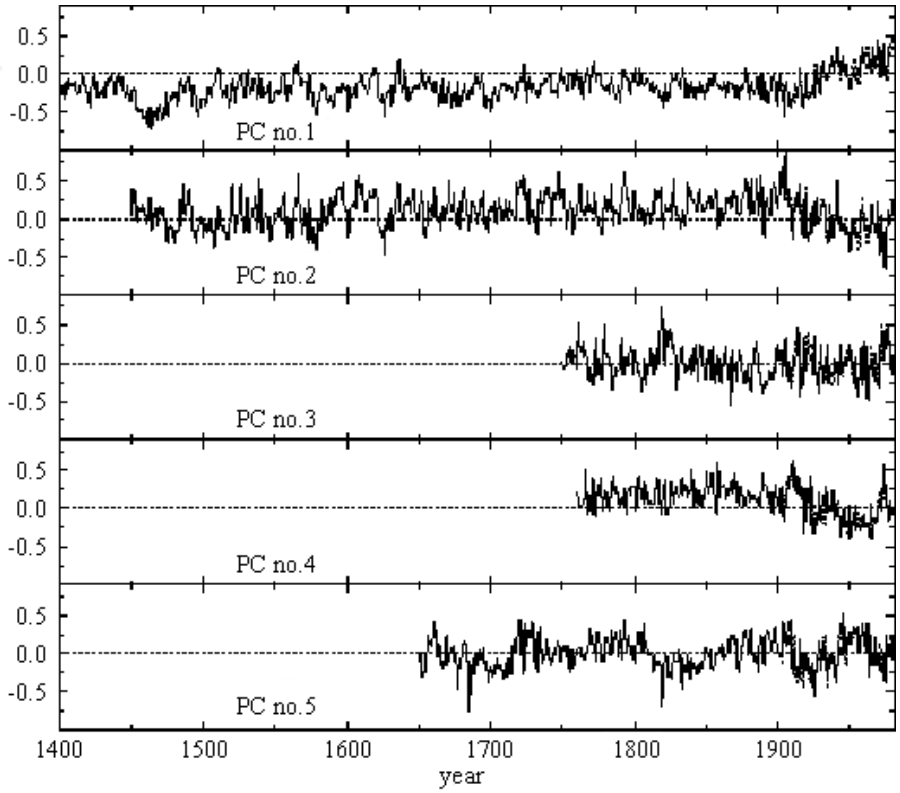

Figure 4.6: The first five principal component time series according to *Mann et al.* [1998]. The zero line corresponds to the 1902-1980 calibration mean of the quantity.

In order to reconstruct temperature data of the last 500 years, the first two principal component time series are spline fitted and shifted so as to serve as LPJ model input data (figure 4.7). The reason for spline fitting is that we are only interested in temperature trends on a long time scale, because interannual temperature fluctuations are provided by data from a simulation by the Hadley Centre climate

model HadCM2-SUL (*Johns et al.* [1997], *Mitchell et al.* [1995]). The fitting of the curves is performed with a Fortran program by Michele Bruno which calculates cubic smoothing spline functions according to *de Boor* [1978] (see appendix C for a short description of the method), where different cutoff periods are used. The PCs (1515-1980) are vertically shifted so that the mean value of the first 10 years (1515 to 1525) is zero. This ensures that there is no significant temperature step in the first year after the model spinup, when reconstructed temperature data are added.

Because the first few pairs of eigenvectors $\vec{c_i}$ and principal component time series $\vec{a_i}$ explain most of the variability of a specific data set (see appendix B), we can reconstruct spatially and temporally resolved temperature perturbation values ΔT_0 from the first two EOF/PC pairs (figure 4.8):

$$\Delta T_0 = \vec{a_1}\vec{c_1} + \vec{a_2}\vec{c_2} \tag{4.1}$$

Temperature anomalies ΔT_0 are set to zero for grid cells with missing data (figure 4.4). Temperatures $\Delta T_{0,10}$ are reconstructed from the leading two PCs spline fitted with a cutoff period of 10 years, $\Delta T_{0,30}$ are based on splined PCs with a cutoff period of 30 years, respectively.

The global mean evolution of reconstructed temperature perturbations ΔT_0 is fluctuating on the order of 0.2° C until 1900 (figure 4.8). Afterwards, a global warming trend of up to 0.4° C is indicated. The long-term trend in the annual mean temperature series shows pronounced cold periods during the late sixteenth and seventeenth and in the early twentieth centuries, and somewhat warmer intervals during the mid-seventeenth and late eighteenth centuries. Analyzing global mean temperature reconstructions does not show generally cooler temperatures between 1550 and 1850. Temperature anomalies calculated from splined PCs nicely approximate the evolution of ΔT_0.

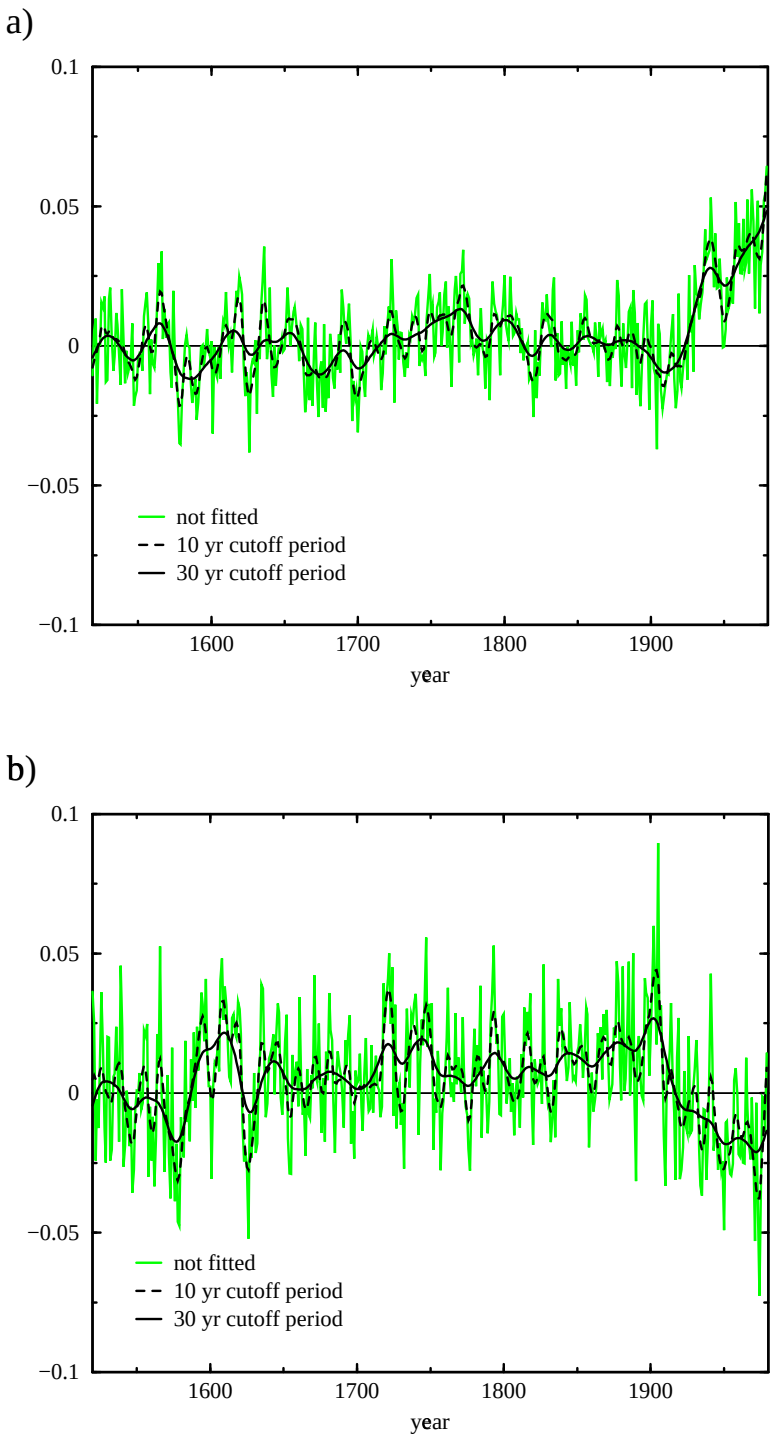

Figure 4.7: Spline fitted and shifted first (a) and second (b) principal component time series (1515-1980). Gray curves are non spline fitted data, black lines are spline functions with cutoff periods of 10 and 30 years, respectively. All curves are vertically shifted so that the mean value of the first 10 years is zero.

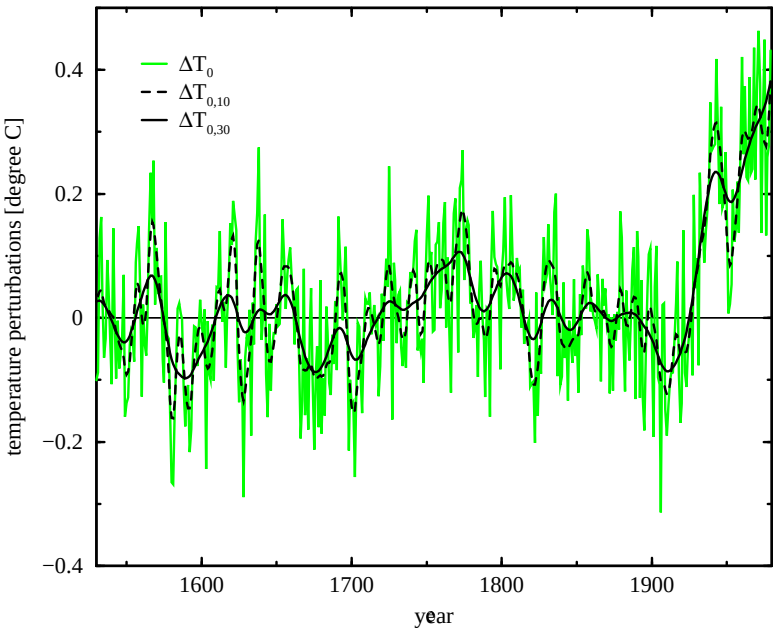

Figure 4.8: Global mean temperature perturbations reconstructed from first two PC/EOF pairs by *Mann et al.* [1998]. The gray curve stands for temperature data ΔT_0, and black lines are based on spline fitted PCs with cutoff periods of 10 and 30 years, respectively. Temperature perturbations are set to zero for grid cells with missing data.

In order to examine the potential influence of spatial gaps in air temperature perturbations (figure 4.4) on the reconstructed uptake, missing temperature data are replaced by zonally averaged values. Therefore, mean continental air temperatures of latitudinal bands (with the LPJ-DGVM resolution of 2.5°) are assigned to grid cells with missing temperature values, resulting in the temperature data set ΔT_z. The effect of using zonally averaged values is an approximate doubling of global mean temperature anomalies (figure 4.9). In the year 1700 for example, the mean temperature change ΔT_0 is –0.14° C, whereas the averaged temperature perturbation ΔT_z is –0.33° C. It is obvious that the use of zonal averages is a rough approximation, especially gaps in the tropics are difficult to reconstruct with this method. Nevertheless, temperature anomalies ΔT_0 resulting from this approach are decidedly more realistic than setting temperature changes in grid cells with missing values to 0° C. Taking into account that changes in continental temperatures are generally larger than oceanic air temperature perturbations, representing inner continental temperatures by temperatures of coastal regions is a rather conservative approach. For those reasons, simulations in this study are performed using temperature perturbations ΔT_z.

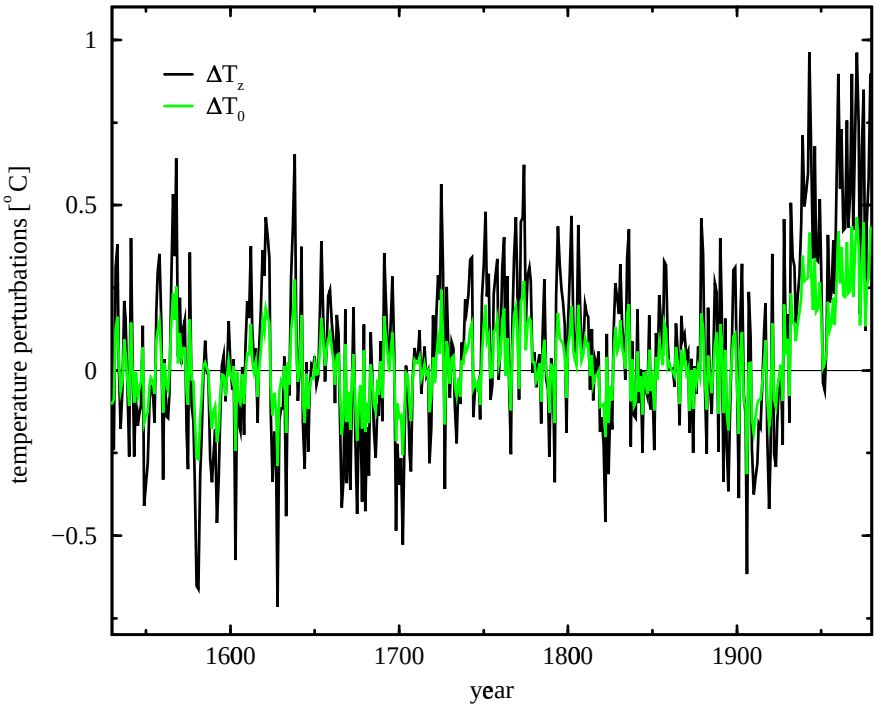

Figure 4.9: Global mean temperature perturbations $\Delta T_{0,z}$ reconstructed from first two PC/EOF pairs by *Mann et al.* [1998]. For the data set ΔT_z, represented by the black line, temperatures of grid cells with missing values are set to zonal averages. The gray curve represents temperature data ΔT_0, where spatial gaps are uniformly set to 0° C.

Mean temperature anomalies between 1550 and 1850 point out that according to data by *Mann et al.* [1998], the cooling trend during this time period was not a global event (figure 4.10). Whereas in the eastern USA, Europe, and China, temperatures decreased by –0.1 to –0.4° C, mean temperatures in tropical regions increased by up to 0.4° C. The following web page maintains a Java animation of temperature patterns by *Mann et al.* [1998] from the year 1730 to 1980:
www.ngdc.noaa.gov/paleo/class/AnniMann/AnniMann.html

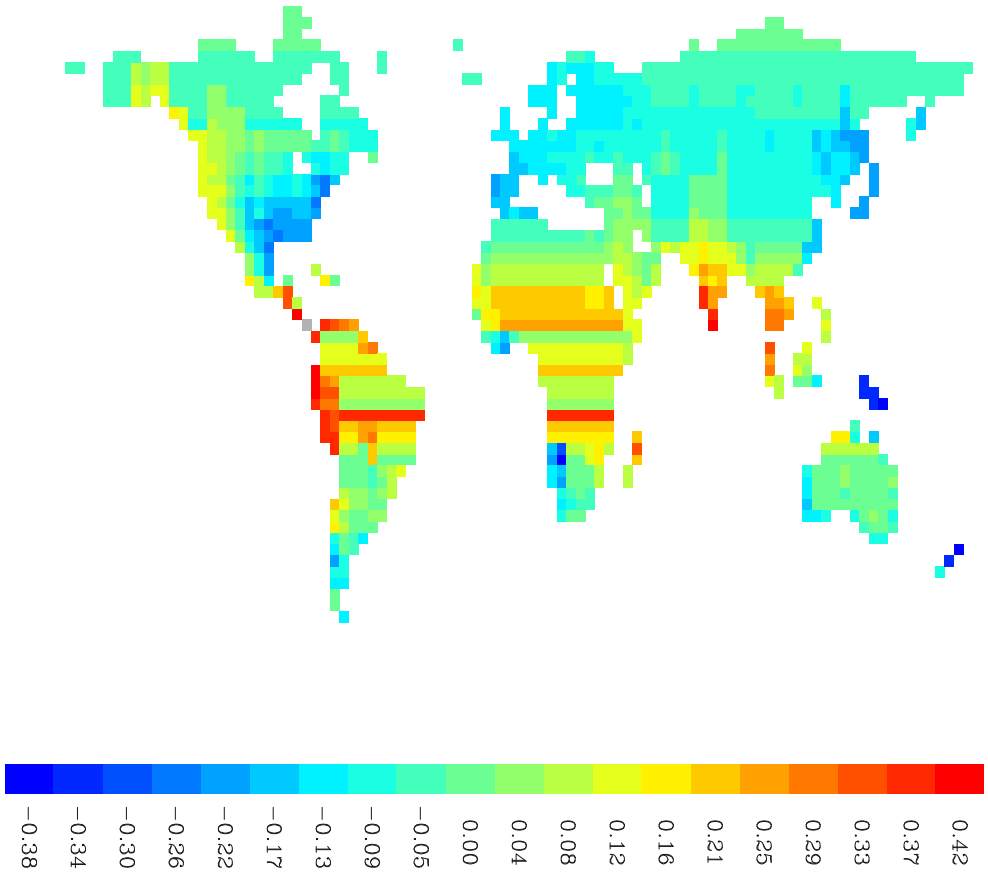

Figure 4.10: Geographical pattern of mean temperature anomalies ΔT_z averaged over the period from the year 1550 and 1850 relative to temperatures around 1515 (in units $^\circ$C). The legend indicates the lowest value of each class represented by different colors.

It has to be pointed out that the reliability of temperature reconstructions by *Mann et al.* [1998] is limited. Because widespread instrumental climate data are available for only about one century, reconstructions reaching further back are based on proxy climate indicators combined with some long instrumental records. The full record of 112 indicators is only available back to 1820, calibrations back to 1760 are based on 93 indicators, the network available back to 1700 consists of 74 indicators (including only two instrumental or historical indicators), 57 indicators (one historical record) reach back to 1600, and only 24 proxy indicators are available back to 1450. The limited availability and reliability of the multiproxy network is to be taken into account interpreting pre-industrial temperature reconstructions.

4.2 Results

Several experiments are performed with different combinations of model input data in order to examine connections between temperatures, atmospheric CO_2 concentrations and terrestrial carbon uptake (table 4.1). During the model spinup of 2000 years (see section 2.6), the LPJ-DGVM is forced with pre-industrial CO_2 concentrations (280 ppmv) and temperatures T_{spinup} for all experiments. Transient simulations start in the year 1515, and the model is run for 465 years until 1980.

experiment	CO_2 concentrations	air temperatures
C(a)	$CO_2(a)$	T_{spinup}
C(b)	$CO_2(b)$	T_{spinup}
T(0)	280 ppmv	$T_{spinup} + \Delta T_0$
T(0,10)	280 ppmv	$T_{spinup} + \Delta T_{0,10}$
T(0,30)	280 ppmv	$T_{spinup} + \Delta T_{0,30}$
T(z)	280 ppmv	$T_{spinup} + \Delta T_z$
C(a)T(z)	$CO_2(a)$	$T_{spinup} + \Delta T_z$
C(b)T(z)	$CO_2(b)$	$T_{spinup} + \Delta T_z$

Table 4.1: Air temperature input data and atmospheric CO_2 concentrations of different model experiments. Major simulations are emphasized. Atmospheric carbon dioxide concentrations $CO_2(a, b)$ are described in section 4.1.1, T_{spinup} are spinup temperature data (2.6), ΔT_0, $\Delta T_{0,10}$, and $\Delta T_{0,30}$ are temperature perturbations according to equation 4.1 basing on different PC splines and with temperature anomalies of grid cells with missing values set to zero, and ΔT_z are temperature perturbations with missing values set to zonal averages.

4.2.1 Simulations with varying CO_2

In order to examine the evolution of terrestrial carbon storage under atmospheric concentrations $CO_2(a)$ and $CO_2(b)$ respectively, and with pre-industrial air temperatures T_{spinup}, simulations C(a,b) are performed. After the sixteenth century, the terrestrial carbon inventories resulting from both simulations continuously decreased, until in the eighteenth century, the perturbation in carbon stock was 7 GtC below zero for the experiment C(a) and 15 GtC below zero for the simulation C(b), respectively (figure 4.11). During the industrial period, the terrestrial biosphere was acting as a carbon sink, and the storage was increasing by up to 90 GtC (1980). The discrepancy of up to 8 GtC between terrestrial inventories of the two simulations in the seventeenth, eighteenth, and nineteenth centuries is caused by differences in the appropriate CO_2 data sets of up to 4 ppmv during this period. Results of both simulations show that the carbon stock was sinking evidently below the baseline carbon storage C_{spinup} during the seventeenth century with constant climatic conditions. The terrestrial biosphere being a carbon source between 1600 and 1700 A.D. is a fundamental inconsistence to the hypothesis of enhanced terrestrial carbon storage

between 1550 and 1850 A.D., although we have to take into account that temperatures are kept constant in the appropriate simulations.

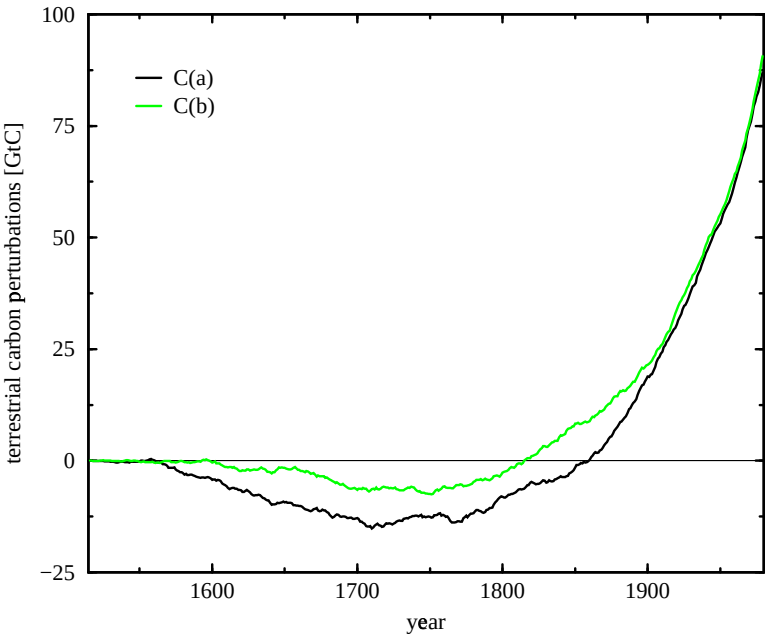

Figure 4.11: Perturbations in terrestrial carbon inventories resulting from simulations C(a,b) with pre-industrial temperatures T_{spinup} and atmospheric CO_2 concentration sets $CO_2(a)$ and $CO_2(b)$ during the last 500 years.

Perturbations in carbon fluxes from the atmosphere to the terrestrial biosphere are analyzed examining results of simulation C(a) (figure 4.12). The temporal evolutions of the fluxes show that terrestrial pools acted as carbon sources during the seventeenth century and as sinks afterwards. Between 1600 and 1700, ΔNPP decreased by 0.8 GtC/yr, before the flux rapidly increased by 7.5 GtC/yr under industrial CO_2 concentrations. Taking into account that perturbations in heterotrophic respiration R_h were slightly smaller than changes in NPP and that carbon fluxes caused by fire events decreased under relatively lower CO_2 concentrations, ΔNEP was approximately 0.1–0.2 GtC/yr below zero during the seventeenth century.

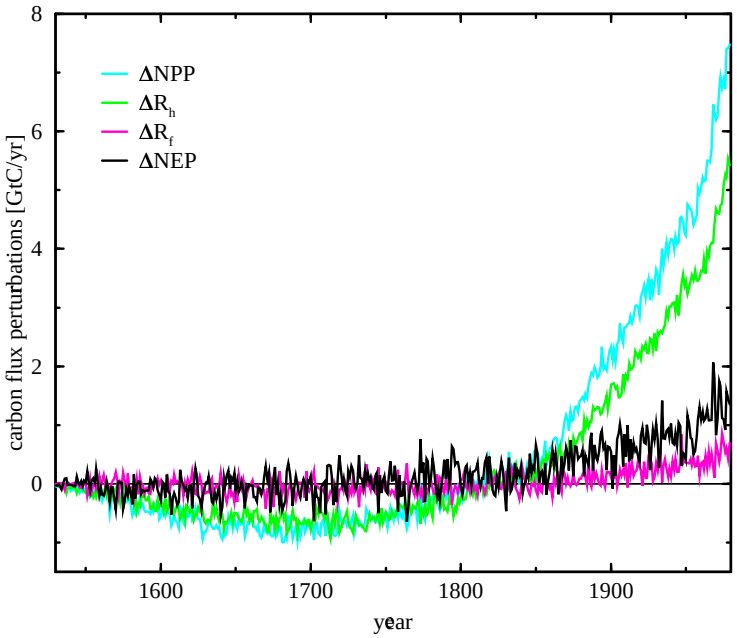

Figure 4.12: Perturbations in carbon fluxes resulting from simulation C(a).

4.2.2 Simulations with varying temperatures

Model simulations T(0), T(0,10), and T(0,30) are performed in order to investigate the influence of interannual variability on terrestrial carbon storage. The evolutions of carbon stocks related to spline fitted PCs show significant discrepancies to the C inventory resulting from temperatures ΔT_0, calculated with non fitted principal component time series (figure 4.13). Terrestrial carbon inventories are in nice accordance until approximately 1650, but afterwards, values related to fitted PCs are 4 to 7 GtC lower than in simulation T(0). The neglect of transient fluctuations of the principal component time series leads to a different vegetation distribution, because years with extremely high or low annual mean temperatures are missing. Because of this dependency of terrestrial carbon uptake on interannual temperature fluctuations, the LPJ model is forced with air temperatures ΔT_0 reconstructed from non-fitted PCs in the following experiments.

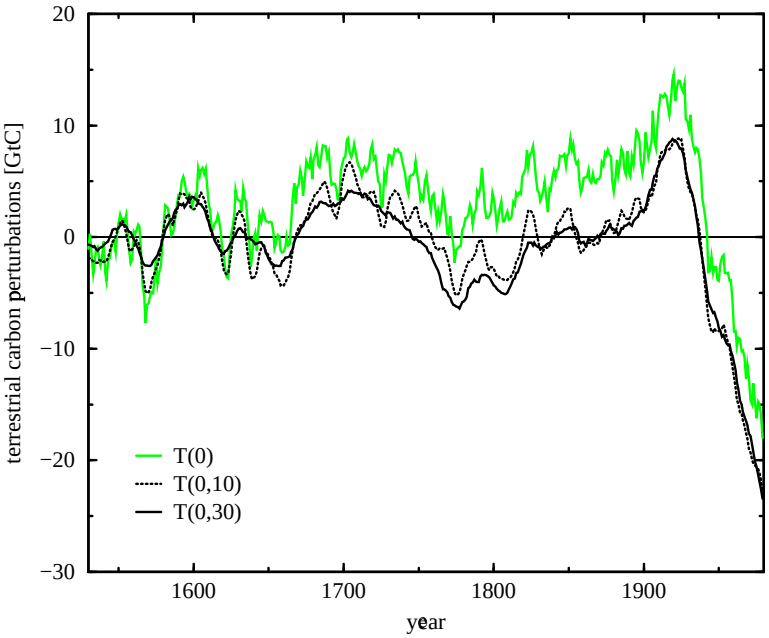

Figure 4.13: Terrestrial carbon inventory perturbations resulting from simulations T(0), T(0,10), and T(0,30). Gray curves stands for carbon stock anomalies resulting from temperature data ΔT_0 (calculated from non-splined PCs), and black lines show results for temperature data based on spline fitted PCs with cutoff periods of 10 and 30 years, respectively. Temperatures of grid cells with missing values are set to 0° C, and the atmospheric CO_2 concentration is 280 ppmv.

The comparison between evolutions of temperature changes ΔT_0 and perturbations in terrestrial carbon inventories shows a fundamental temperature dependency of terrestrial carbon storage (figure 4.14). With decreasing air temperatures, the heterotrophic respiration R_h decreases because of smaller decomposition rates, and NPP is simultaneously increased because plants tend to open their stomatas. These reactions result in enhanced carbon storage under decreased air temperatures and reduced carbon storage with higher temperatures. Therefore, major decreases in ΔT_0 in the late sixteenth and seventeenth and in the early twentieth centuries result in pronounced increases in terrestrial carbon storage. Around 1600, the carbon inventory is increased by approximately 5 GtC, and from 1670 to 1750, the terrestrial storage is enhanced by 5–8 GtC relative to the baseline carbon inventory C_{spinup}. Specific transient fluctuations in the evolutions of temperatures and carbon inventory can hardly be related, but trends on longer time scales show that the carbon cycle reacts to temperature variations within decades.

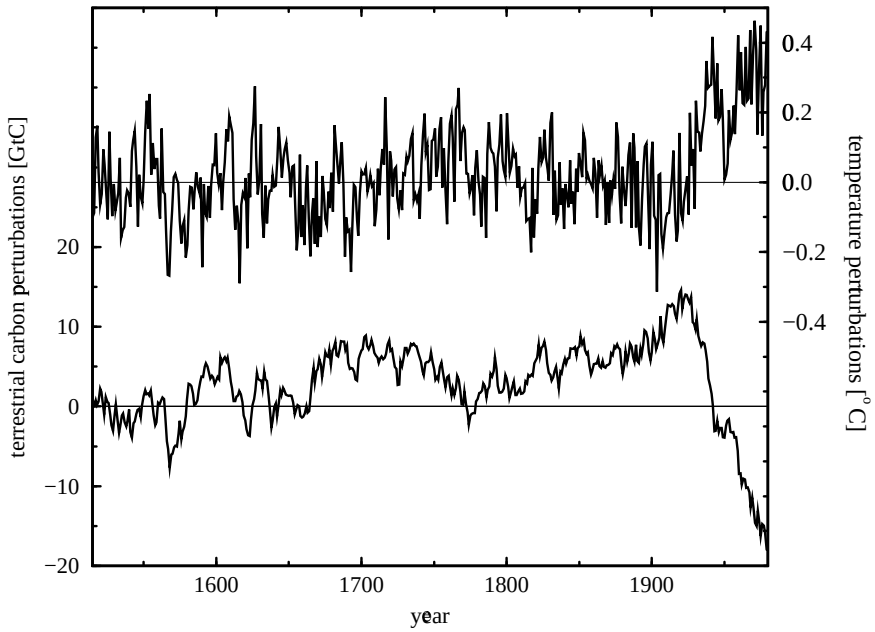

Figure 4.14: Changes in terrestrial carbon inventory resulting from air temperature perturbations ΔT_0. The upper curve indicates global mean temperature perturbations, and the lower curve represents carbon stock anomalies.

Now, the potential influence of missing temperature data on the reconstructed terrestrial uptake is examined. Therefore, simulation T(z) is compared with experiment T(0) (figure 4.15). Perturbations in terrestrial carbon inventories are generally stronger if the model is forced with temperatures ΔT_z supplemented by zonally averaged values than with ΔT_0. Especially storage anomalies lasting several decades are amplified in the simulation T(z). Hence the most significant effects of using zonally averaged temperatures are a higher increase in carbon storage in 1600 and reinforced decreases of the terrestrial carbon stock between 1725 and 1900 A.D. and after 1940. After a major decrease in terrestrial carbon inventory during the eighteenth century, simulation T(z) results in a perturbation in carbon storage of –12 GtC around 1775, whereas according to experiment T(0), the storage is only perturbed by –1 GtC.

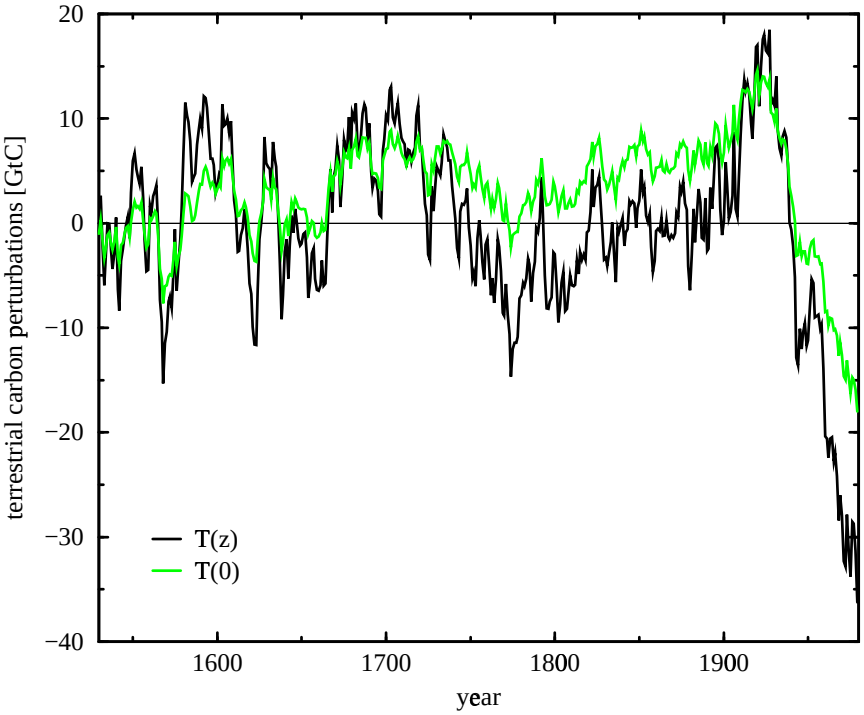

Figure 4.15: Perturbations in terrestrial carbon inventories resulting from model runs with air temperature data $\Delta T_{0,z}$ reconstructed from values by *Mann et al.* [1998]. For the simulation represented by the black curve, grid cells with missing temperatures are set to zonally averaged temperatures. The gray curve represents an experiment where spatial temperature gaps are uniformly set to 0° C.

4.2.3 Simulations with varying CO_2 and temperatures

Now, terrestrial carbon inventories resulting from simulations with changing CO_2 concentrations and temperatures are examined, and the coupling of CO_2 and temperature effects is analyzed. The comparison between carbon stocks resulting from simulations C(a,b) and the appropriate C inventories according to experiments C(a,b)T(z) shows that during the pre-industrial period, changes in carbon storage resulting from CO_2 perturbations were of about the same magnitude as changes due to temperature anomalies (figure 4.16). During the industrial period, the evolution of the terrestrial carbon stock was dominated by the atmospheric CO_2 increase. Results of the simulation C(a) show that during the seventeenth century, the terrestrial biosphere was acting as a carbon source, until the perturbation in C stock was −15 GtC in 1700. Afterwards, the biosphere continuously took up carbon from the atmosphere. Simultaneously forcing the model with temperature anomalies ΔT_z results in further decreases of the carbon inventory in the mid-seventeenth and late

eighteenth centuries and increases around 1600 and 1700. In the year 1600, the carbon storage was 7 GtC above the model spinup level, but afterwards, perturbations in carbon inventory were negative until 1850. Forcing the LPJ model with atmospheric concentrations $CO_2(b)$ leads to a slightly enhanced carbon storage, but the pre-industrial terrestrial carbon content was only exceeded by 7 GtC around the year 1700. Therefore, the simulations C(a,b)T(z) do not confirm the hypothesis that approximately 40 GtC entered the terrestrial biosphere from the year 1550 to 1850.

In order to examine how effects of changing temperatures and CO_2 concentrations on terrestrial carbon uptake are coupled, we compare the simulations T(z) and C(a,b) with combined experiments C(a,b)T(z) (figure 4.17). In general, there is more carbon in terrestrial stocks resulting from simulations C(a,b)T(z) than resulting from the sum of experiments T(z) and C(a,b). Although we can observe this tendency for both atmospheric concentrations $CO_2(a, b)$, distinctions are only up to 7 GtC. So, the superposition of temperature and carbon effects is approximately linear.

Absolute temperature anomalies and the influences on carbon storage are significantly stronger in lower latitudes (figure 4.18). Between 30° N and 30° S, mean air temperatures decrease by more than 1° C during the late sixteenth and mid-seventeenth centuries. Relative to simulation C(a), the terrestrial carbon storage resulting from simulation C(a)T(z) increases by 150 – 250 gC/m^2 around the years 1600 and 1700 in low latitudes. In higher latitudes, the appropriate perturbations in carbon storage are only up to 50 gC/m^2, because decreases in air temperatures are not higher than 0.3° C.

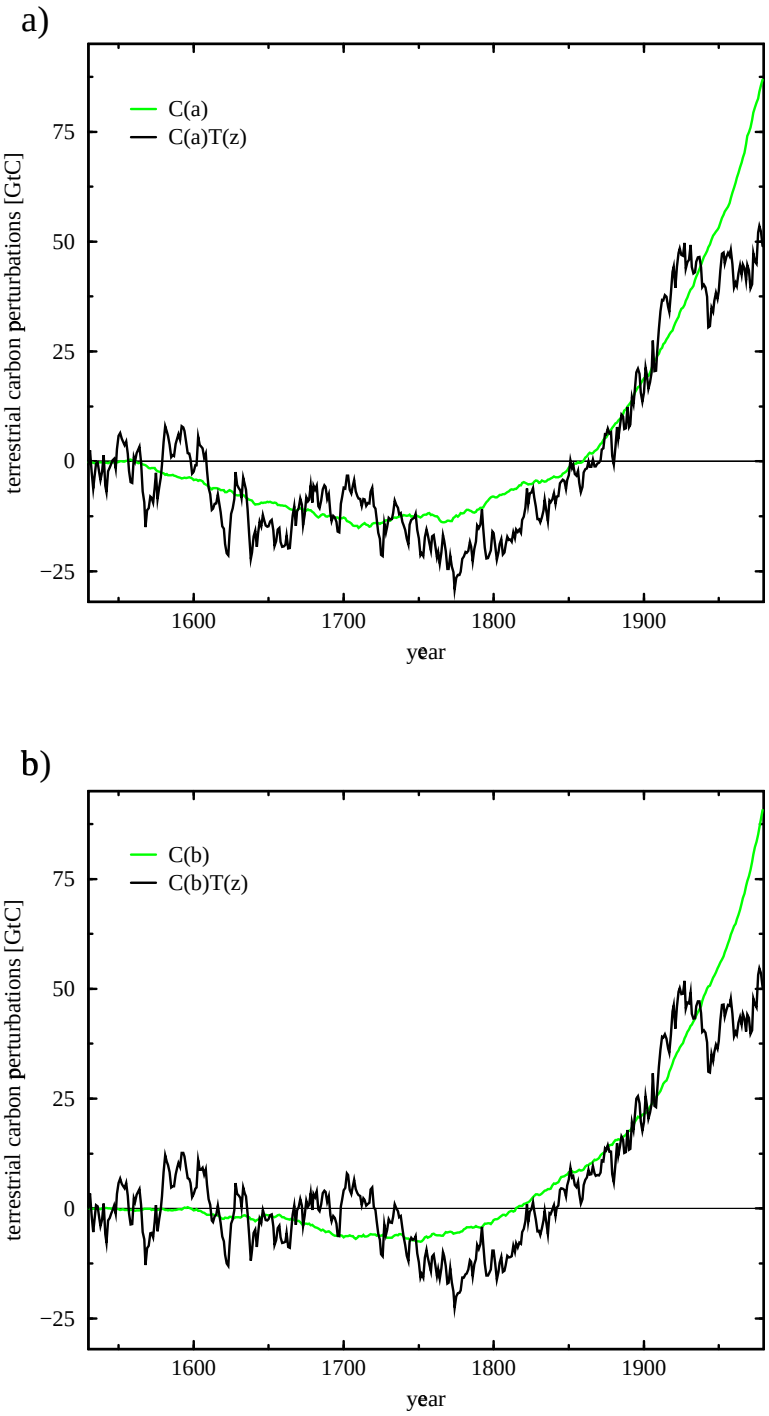

Figure 4.16: Perturbations in terrestrial carbon inventories for experiments C(a,b) with pre-industrial air temperatures (gray curves) and for C(a,b)T(z) with additional temperature data ΔT_z (black curves). For simulations in panel (a), atmospheric data $CO_2(a)$ were applied, whereas for experiments indicated in panel (b), the model was forced with carbon dioxide concentrations $CO_2(b)$.

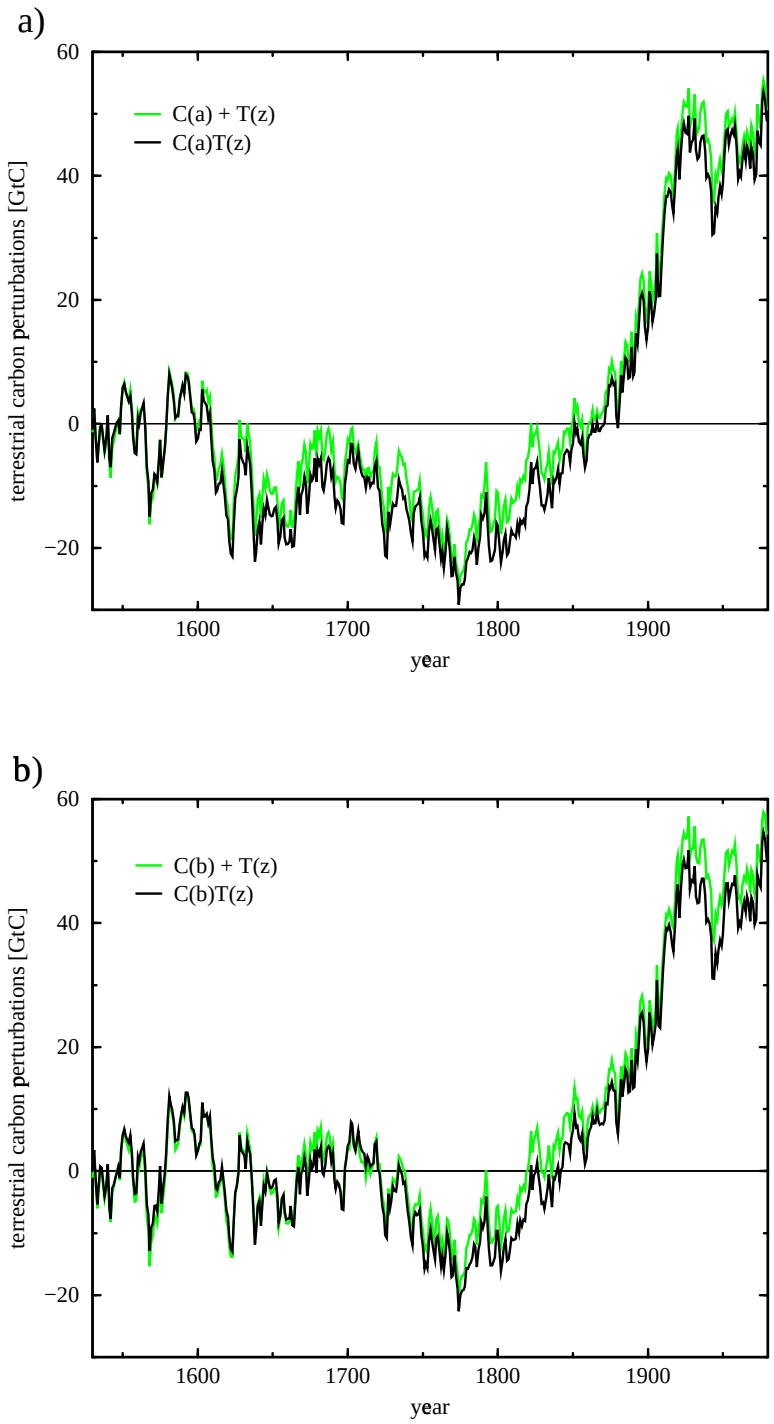

Figure 4.17: Perturbations in terrestrial carbon inventories resulting from temperature and CO_2 change simulations. Panel (a) shows results from simulations with the forcing of atmospheric concentrations $CO_2(a)$, panel (b) represents experiments with the data set $CO_2(b)$. Black lines indicate results of experiments C(a,b)T(z), whereas gray curves show carbon stocks for linear superpositions of simulations T(z) and C(a,b).

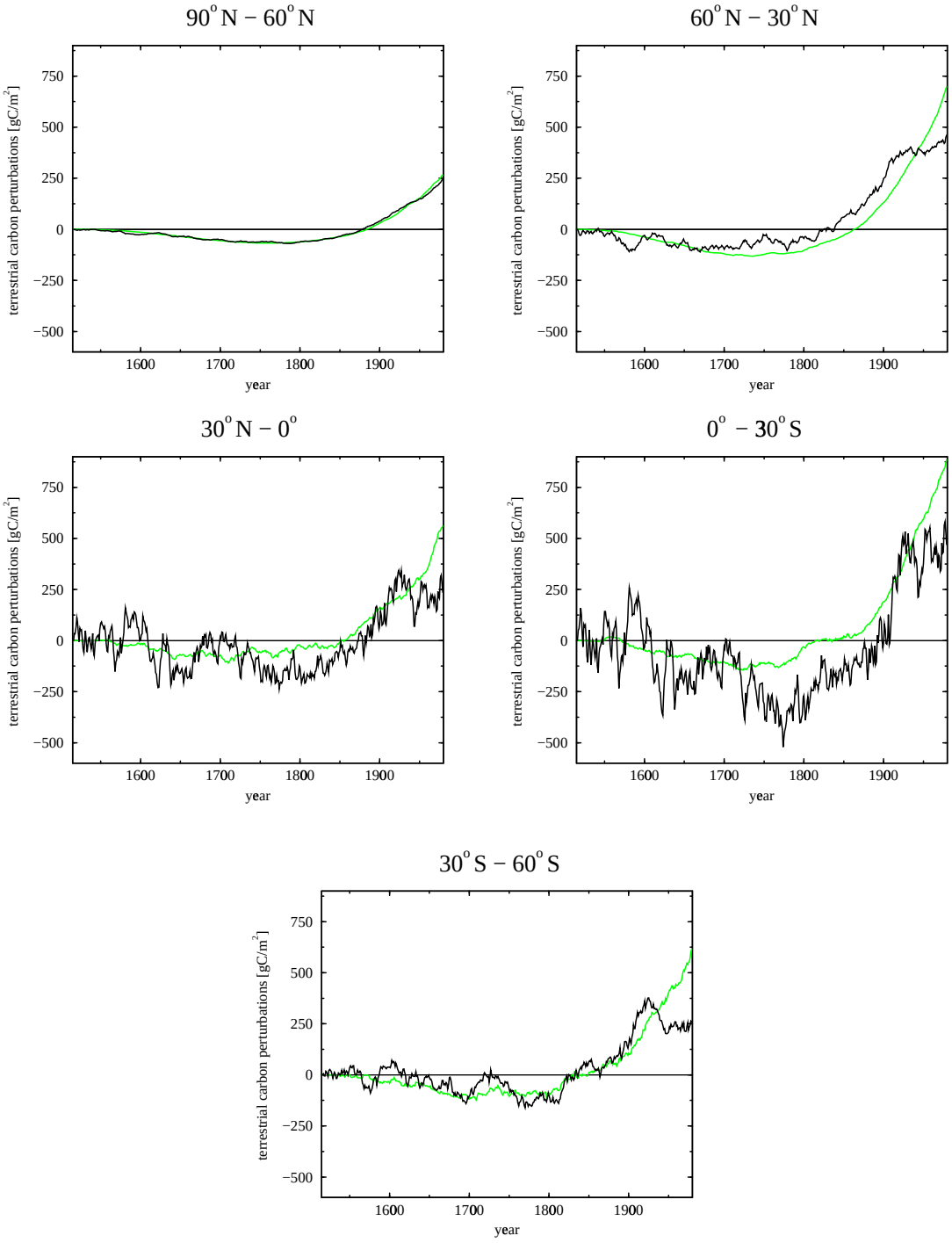

Figure 4.18: Mean terrestrial carbon storage in latitudinal bands for simulations C(a) (gray) and C(a)T(z) (black), respectively. The stock is indicated in units gC/m^2, so that bands with different continental areas are comparable. Areas of latitudinal bands in units m^2: $1.36 \cdot 10^{13}$ (90°N–60°N), $4.69 \cdot 10^{13}$ (60°N–30°N), $3.85 \cdot 10^{13}$ (30°N–0°), $2.84 \cdot 10^{13}$ (0°–30°S), and $6.20 \cdot 10^{12}$ (30°S–60°S).

Chapter 5

Conclusions and discussion

5.1 Model sensitivity analyses

The sensitivity of the vegetation distribution and the terrestrial carbon storage to atmospheric CO_2 concentrations and climatic variables is favoredanalyzed with step-like perturbations of the appropriate variable. CO_2 concentrations and temperatures are changed by globally uniform absolute values, whereas precipitation is perturbed by globally uniform relative values.

In order to examine the sensitivity of the terrestrial biosphere to atmospheric CO_2 concentrations, simulations with step-like CO_2 increases are performed, whereas climate is kept constant. An immediate doubling of atmospheric CO_2 concentrations results in an increase in terrestrial carbon storage by approximately one third, and when the CO_2 concentration is tripled, the carbon stock is increased by 50%. Half of the additional carbon enters the vegetation pools because of increased plant growth rates under elevated CO_2 concentrations (carbon fertilization effect), whereby tropical rainforests play a key role for the terrestrial carbon storage. In vegetation dynamics, woody PFTs are over grasses due to their competitive advantage for light over understory vegetation. Because soil organic matter pools have extremely long turnover times, the terrestrial biosphere is not in an equilibrium state until approximately 4000 years after a CO_2 increase by 500 ppmv.

The temperature sensitivity of the terrestrial biosphere is analyzed with instantaneous air temperature perturbations by 1° C. With decreasing temperatures, plants tend to open their stomatas because moisture loss is reduced. The enhanced NPP and the simultaneous decrease in R_h because of smaller decomposition rates result in an increased terrestrial carbon storage. If temperatures are globally increased by 1° C, the perturbation in carbon storage is –65 GtC in the new equilibrium, whereas after a globally uniform temperature decrease by 1° C, the biosphere takes up 85 GtC. The terrestrial carbon storage is more sensitive to temperature decreases, but the

reaction to increased temperatures is larger immediately after the perturbation. If air temperatures are simultaneously decreased by 1° C in the NH and increased by 1° C in the SH, all PFTs show a southward shift, because temperatures maintaining optimal growing conditions can be found in lower latitudes. If the strength of inter-annual temperature variations is increased by 10%, the terrestrial carbon inventory decreases by 66 GtC, and if the seasonality is reduced by 10%, the additional carbon storage is 22 GtC. Major changes in vegetation resulting from seasonality variations are in northern mid-latitudes.

The sensitivity of terrestrial carbon uptake to a global uniformly global relative precipitation decrease is slightly stronger than to an increase in precipitation. The terrestrial carbon inventory changes by −130 GtC after a precipitation decrease by 20%, and by 100 GtC resulting from increased precipitation by 20%. But apart from this effect, perturbations in carbon inventories are linearly related to relative changes in precipitation. Most PFTs do not significantly change their geographical distribution after a global decrease in precipitation by 20%. The major effect due to decreased snow- and rainfall is a globally enhanced extent of deserts.

5.2 "Little ice age" hypothesis

Several records of atmospheric CO_2 concentrations reconstructed from air bubbles entrapped in ice cores show that the level of CO_2 decreased around 1550, and stayed low until about 1850. This period is around the time of reported low temperatures in Europe is often referred to as "little ice age" (LIA) [*Grove*, 1988].

The major purpose of this study is the analysis of the hypothesis that the relatively low atmospheric CO_2 level during the appropriate time period was caused by an enhanced terrestrial carbon storage (*Trudinger et al.* [1999], *Joos et al.* [1999]). According to our simulations, this hypothesis can not be validated. Although the terrestrial carbon storage is temporally increased under lower air temperatures between 1550 and 1850, the effect of decreasing CO_2 concentrations is clearly dominating. As a consequence, the terrestrial biosphere is a carbon source during the whole seventeenth century, and the carbon storage is mostly below the level of the year 1500 during the time period with decreased CO_2 concentrations.

We now try to estimate the stability of our simulation results by summarizing limitations and uncertainties of input data and model parameters. A major problem is that our input data are limited by various reasons. Reconstructed atmospheric CO_2 concentrations show clear decreases between 1550 and 1850, but there is a significant discrepancy between the two data sets used in this study. Whereas concentrations $CO_2(a)$ [*Etheridge et al.*, 1996] decrease by up to 6 ppmv between 1550 and 1850,

atmospheric CO_2 in data set $CO_2(b)$ (*Barnola et al.* [1995], *Neftel et al.* [1982], *Neftel et al.* [1994], *Siegenthaler et al.* [1988]) only decreases by 2 ppmv between the year 1550 and 1700. This significant difference clearly shows that there are major uncertainties in reconstructing highly resolved atmospheric CO_2 concentrations from ice core measurements. Problems may be related to uncertainties in analyzing and dating ice core measurements and to overlaid regional effects resulting from specific drilling locations.

Temporal and spatial evolutions of temperature anomalies by *Mann et al.* [1998] are dominated by strong fluctuations. So, global mean temperatures only show pronounced cool periods during a few decades in the late sixteenth and seventeenth centuries, and averaged temperature perturbations between 1550 and 1850 A.D. are only below zero in some specific regions of the world (i.e. eastern USA, Europe, and China). The reliability of those temperature reconstructions is clearly limited, because only few long instrumental records are available, and the reconstruction from proxy climate indicators is associated with significant uncertainties. Another problem are spatial gaps of temperature patterns in large continental regions of the world. Using zonally averaged values as temperature anomalies of grid cells with missing data is a rough approximation, and especially temperatures of tropical regions are difficult to reconstruct with this approach.

Unfortunately, temperatures are the only spatially resolved climate data available back to the sixteenth century. Therefore, for climatic parameters such as cloud cover or precipitation patterns, the same data are used for transient simulations as during the model spinup. According to our sensitivity analyses, perturbations in global carbon storage are almost linearly dependent on uniform changes in precipitation. According to simulations by *Voss and Mikolajewicz* [1999], precipitation changes by 2.42% for temperature variations by 1° C, and *Hulme et al.* [1998] predicts precipitation sensitivity to be 2.37%/° C. Combining these informations, the terrestrial carbon storage would approximately decrease by 15 GtC for a globally uniform temperature decrease by 1° C. This suggests that a consideration of the precipitation anomalies would rather tend to reduce the magnitude of the simulated carbon storage induced by temperature changes only.

Except of model simplifications such as the reduction of PFTs to average individuals or the spatial resolution of 2.5×3.75 degrees, there are several further restrictions and simplifications in the LPJ-DGVM. A general uncertainty by simulating vegetation dynamics is the choice of reasonable vegetation sensitivities to atmospheric CO_2 concentrations and air temperatures. Another problem of the LPJ model is the strong sensitivity of the vegetation to interannual climatic perturbations.

Summarizing our analyzes, the hypothesis of enhanced terrestrial carbon storage due to lower air temperatures is not validated by LPJ-DGVM simulations. Major problems are limited availabilities and reliabilities of climate data and atmospheric CO_2 concentrations. Dynamic vegetation models are important tools in order to understand reactions of the terrestrial biosphere to climate perturbations or changes in CO_2 concentrations. But in order to analyze pre-industrial climatic events, more reliable data with higher temporal and spatial resolutions will be necessary.

Chapter 6

Acknowledgments

First of all I would like to thank Prof. Dr. Thomas Stocker for giving me the opportunity to write my diploma thesis in the Department of Climate and Environmental Physics, and for our valuable discussions which have helped to clarify this work.

I cordially thank PD. Dr. Fortunat Joos for his excellent support and advice during my diploma thesis. He was always there to lend an ear and to provide me with countless suggestions and hints.

In particular, I thank Dr. Stephen Sitch and his group for providing me with the LPJ-DGVM and the draft version of the model description [*Sitch et al.*, 2000].

I am indebted to Dr. Robert Meyer for patiently introducing me to the world of climate modeling and for providing me with ingenious methods to debug Fortran programs.

Furthermore, I gratefully acknowledge the positive and comfortable working atmosphere Dr. Marc Blatter helped to create, and I appreciate his friendship and his professional technical assistance.

To Kasper Plattner and Michael Aeberhardt I am grateful for their careful review of the manuscript, and for many valuable and helpful comments.

Renato Nanni deserves special mention for his professional support regarding plant properties and complex biological processes.

Last but not least, I would like to thank my parents for their valuable moral and financial support during my studies. Especially, I am grateful to my family, to Simone, and to all my friends for their friendship and support.

Appendix A

Major world biomes

Structurally and functionally distinct ecosystem complexes, known as biomes, occur in different climates. There are several global biome classifications, and in this study, we distinguish the major world biomes tundra, taiga, temperate forest, temperate grassland, desert, savannah, and tropical rainforest. The following short descriptions of those biological communities are written based on the following web page: *www.ucmp.berkeley.edu/glossary/gloss5/biome*.

Tundra is the coldest of all the biomes, and it occupies the world in the highest northern latitudes. The expression *tundra* comes from the Finnish word *tunturia*, meaning treeless plain. Trees can hardly survive in those regions because of the harsh climatic conditions (temperatures between –34 and 12° C, and precipitation of 150 to 250 mm/yr), and therefore the vegetation is dominated by small plants and grasses. Tundra is covered in snow and ice for most of the year.

The taiga, also known as boreal or northern coniferous forest, is the largest biome in the world. It covers big parts of Canada, Europe, and Asia. The cold climate mainly supports coniferous trees with long, waxy needles. In order not to waste energy to grow new leaves every year, most trees in this biome are evergreen plants. Precipitation, primarily in the form of snow, is between 400 and 1000 mm/year, and boreal plants resist the loss of moisture with their thick bark and with a small stomatal conductance.

The temperate forest biome, also called deciduous forest, is found in the middle latitudes in eastern North America, western Europe, and eastern Asia. In the southern hemisphere, smaller areas of temperate forest can be found in South America, southern Africa, and Australia. In all those regions, there are four definite seasons with temperatures between -30 and 30° C and with evenly distributed precipitation throughout the year (750 to 1500 mm/yr). Most of the trees in temperate forests are summergreen plants, and they shed their leaves during winters in order to survive under cold and drought conditions.

The major manifestations of temperate grasslands are the plains and prairies of central North America, the pampas of Argentina and Uruguay, the Puszta of Hungary, and the steppes of Russia. Precipitation and temperature are both varying extremely strong over the course of the year. Seasonal droughts and occasional fires prevent most woody shrubs and trees from invading and becoming established, and this biome is characterized by having grasses as the dominant vegetation. Regions with tall grasses are called prairies, and steppes are areas with rather short grasses.

Deserts cover about one fifth of the Earth's land surface. Although most deserts, such as the Sahara of North Africa and the deserts of the southwestern USA, Mexico, and Australia, occur at low latitudes, so called cold deserts can be found in the basin and range area of Utah and Nevada and in parts of western Asia. Deserts are in regions where rainfall is less than 500 mm/yr, so only some few specialized plants are able to survive under those drought conditions.

Savannahs dominate the continent of Africa, and they are also found in India and in the northern part of South America, mostly located at the edges of tropical rainforests. The rainfall from 500 to 1300 mm/yr is concentrated in about six months of the year, followed by a long period of drought. Wildfires which occur in those seasons are very important in order to maintain savannahs. Although most parts of the vegetation are consumed by fire, savannah plants retain some moisture in their deep roots in order to survive the dry season. The seasonal fires and grazing of animals maintain the typical savannah landscape: Deciduous trees, palms and shrubs that are scattered across open grassland.

Tropical rainforests occur near the equator, and the largest remaining areas can be found in Central and South America, West Africa, and Southeast Asia. With temperatures between 20 and 25° C and rainfall of more than 2000 mm/yr, those regions are the hottest and wettest places on earth. The tropical climatic conditions provide rapid decomposition, a very high primary productivity, and a great diversity of plant and animal species. Trees mostly have an evergreen seasonality, and the tallest of them, the so called giant trees, may tower 60 m in height.

Appendix B

Empirical orthogonal function analysis

This chapter gives a brief summary of a widely used method for analyzing the spatial and temporal variability of a data field. It is the method of empirical orthogonal functions (EOFs), also known as principal component analysis (PCA). Two important references for the EOF method are *Preisendorfer* [1988] and *von Storch and Navarra* [1993]. Those books contain a wealth of information about the method, ranging from practical examples and applications to detailed mathematical explanations.

The EOF analysis is an excellent tool to reduce the amount of variables of a huge data set without losing too much information about the variability of the field. This can be done by removing the correlation of the original variables, which is redundant information. Therefore, the data are separated into uncorrelated spatial patterns of variability (EOFs) and their time variations (PCs). In addition, the EOF method gives a measure of the relative importance of each spatial pattern for the total variation.

We assume that the data set to be analyzed consists of measurements of a variable x at different locations i $(i = 1, ..., p)$ taken at times t_j $(j = 1, ..., n)$. Those data are arranged in a matrix F of size n by p, so that each of the p columns can be interpreted as a time series of a given location. The time series are centered on their averages, so that each column has zero mean. With this normalized matrix we form the so called *covariance matrix*

$$R = F^T F \tag{B.1}$$

The covariance matrix R is symmetric, its diagonal elements are the sample variances of the variables x_i, and the other elements are the covariances among those variables.

Now we solve the eigenvalue problem

$$RC = \Lambda C \tag{B.2}$$

where Λ is a diagonal matrix containing the eigenvalues λ_i of R. The column vectors $\vec{c_i}$ of C are the eigenvectors of R corresponding to the eigenvalues λ_i. These eigenvectors are the EOFs we were looking for. We define the first EOF ($\vec{c_1}$) as the vector associated with the biggest eigenvalue, the one associated with the second biggest eigenvalue is $\vec{c_2}$, etc. Each eigenvalue λ_i is a measure of the fraction of the total variance in R explained by the corresponding mode. This fraction is found by dividing λ_i by the trace of Λ. An important property of the eigenvector matrix C is that $C^T C = CC^T = I$, which means that the EOFs are uncorrelated over space and therefore orthogonal to each other.

If we are interested in the temporal evolution of a specific EOF $\vec{c_i}$, we calculate the corresponding principal component time series $\vec{a_i}$ by projecting F onto $\vec{c_i}$:

$$\vec{a_i} = F\vec{c_i} \tag{B.3}$$

For each calculated EOF, we can find a corresponding PC. Just as the EOFs were uncorrelated in space, the expansion coefficients are uncorrelated in time.

Finally, and most importantly, the original centered data set can exactly be reconstructed from the EOFs and the principal component time series in the following way:

$$F = \sum_{i=1}^{p} \vec{a_i} \cdot \vec{c_i} \tag{B.4}$$

A common use of EOFs is to extract the fraction of data which only contain elements producing the largest correlations. Implicit assumption is that this provides an indication of the dominant processes that characterize the appropriate data set. Therefore the sum in equation B.4 is truncated at some $i = N \ll p$, and only the EOFs of the largest N eigenvalues are considered.

Appendix C

Cubic smoothing splines

In this section, the use of smoothing splines in the analysis of climate data is summarized showing the behavior of spline fitting as a low-pass filter. Smoothing splines are particularly suitable for interpolating irregularly spaced data, since the filtering properties are only weakly dependent on the data density. We are mainly following *Enting* [1987] and *de Boor* [1978].

A set of data consisting of values $z_i = z(t_i)$ for times t_i and associated weights δ_i, where $i = 1$ to N, is fitted by a function $\hat{y}(t)$, which is constructed on the basis of a trade-off between minimizing both

$$S = \sum_{i=1}^{N} \frac{(z_i - \hat{y}(t_i))^2}{{\delta_i}^2} \tag{C.1}$$

$$Q = \int_{t_1}^{t_N} \left(\frac{d^2}{dt^2} \hat{y}(t) \right)^2 dt \tag{C.2}$$

In any analysis procedure one seeks to extract a signal representing a particular class of variations, and all other variation must be regarded as noise that should be suppressed. This relation is expressed as

$$z(t) = y(t) + \epsilon(t) \tag{C.3}$$

where the observed variation $z(t)$ is the sum of a signal $y(t)$ and the noise $\epsilon(t)$. The aim in analyzing a data set in this way is to produce an estimate $\hat{y}(t)$ of the unknown signal $y(t)$. As mentioned above, smoothing splines are particularly suitable for producing a continuous function $\hat{y}(t)$ from a discrete data record z_i, even if the times t_i are not uniformly spaced. The analyses of smoothing splines address the minimization problem by introducing a scaling factor λ, and minimizing the cost function

$$\theta(\lambda) = S + \lambda Q \tag{C.4}$$

Within the set of functions with continuous first derivatives, the function that minimizes θ is a piecewise cubic polynomial, with discontinuities in the third derivative at each point t_i and all lower derivatives continuous everywhere. Of course, actual computational procedures for obtaining $\hat{y}(t)$ exploit this knowledge of the form of the solution and minimize θ over the set of such cubic splines. The division between high and low frequencies depend on the purpose of the investigation, and it determines the choice of λ.

List of Tables

2.1 PFT specific parameters 10

2.2 PFT bioclimatic limits 12

2.3 Carbon pool properties 20

3.1 Carbon uptake of the C pools after an instantaneous atmospheric CO_2 increase by 500 ppmv 30

3.2 Carbon uptake of the five pools after a change in seasonality by -10% or +10%, respectively 56

4.1 Air temperature input data and atmospheric CO_2 concentrations of different model experiments 77

List of Figures

2.1 Comparison between geographical plant distributions of LPJ model runs and satellite data 15

2.2 Water fluxes between the two soil layers and the atmosphere. 17

2.3 Carbon fluxes between model compartments and the atmosphere . . . 19

2.4 Temperature and moisture response functions for calculations of decomposition rates 21

2.5 Proportion of a specific grid cell affected by fire as a function of the fire index 24

2.6 Geographical pattern of air temperatures 25

2.7 Geographical pattern of precipitation 26

2.8 Geographical pattern of cloud cover 27

3.1 Perturbations in terrestrial carbon inventory due to step-like increases of atmospheric CO_2 concentrations 31

3.2 Relation between perturbations in terrestrial carbon stock heights of step-like atmospheric CO_2 increases 32

3.3 Carbon flux perturbations resulting from a step-like increase by 500 ppmv in atmospheric CO_2 concentration 33

3.4 Perturbations in the terrestrial carbon inventory due to a step-like atmospheric CO_2 increase by 500 ppmv 34

3.5 Foliar projective cover of tropical broadleaved evergreen and raingreen trees, and temperate needleleaved evergreen trees 36

3.6 Foliar projective cover of temperate broadleaved evergreen and summergreen trees, and boreal needleleaved evergreen trees 37

3.7 Foliar projective cover of boreal summergreen trees, cool grass, and warm grass 38

3.8 Location of six chosen grid cells representing different biomes 40

3.9 Perturbations in carbon fluxes and foliar projective covers of tundra, taiga, and temperate forest after an instantaneous atmospheric CO_2 increase by 500 ppmv 41

3.10 Perturbations in carbon fluxes and foliar projective covers of temperate grassland, savannah, and tropical rainforest after an instantaneous atmospheric CO_2 increase by 500 ppmv 42

3.11 Zonally averaged mean continental air temperatures 45

3.12 Perturbations in terrestrial carbon inventories due to air temperature steps 46

3.13 Perturbations in the terrestrial carbon storage due to a globally uniform step-like increase in air temperatures by 1° C. 47

3.14 Carbon flux perturbations resulting from step-like global air temperature changes by –1° C and +1° C, respectively 48

3.15 Carbon flux perturbations resulting from a step-like air temperature change by –1° C in the NH and of +1° C in the SH 49

3.16 Areas covered by tropical broadleaved evergreen, tropical broadleaved raingreen, and temperate needleleaved evergreen trees, resulting from an air temperature step of –1° C in the NH, and +1° C in the SH . . . 51

3.17 Areas covered by temperate broadleaved evergreen and summergreen, and boreal needleleaved evergreen trees, resulting from an air temperature step of –1° C in the NH, and +1° C in the SH 52

3.18 Areas covered by boreal summergreen trees, cool and warm grass, resulting from an air temperature step of –1° C in the NH, and +1° C in the SH 53

3.19 Geographical PFT distribution resulting from an air temperature step of –1° C in the NH and of +1° C in the SH. 54

3.20 Global mean continental temperature seasonality 55

3.21 Geographical PFT distribution resulting from a decrease in temperature seasonality by 10% 57

3.22 Geographical PFT distribution resulting from an increase in temperature seasonality by 10% 58

3.23 Perturbations in the terrestrial carbon storage due to a global increase in air temperature seasonality by 10%. 59

3.24 Perturbations in terrestrial carbon inventories due to precipitation variations 60

3.25 Carbon flux perturbations resulting from perturbations in precipitation by 20% 61

3.26 Perturbations in terrestrial carbon storage resulting from changes in precipitation 62

3.27 Geographical PFT distribution resulting from a global precipitation decrease by 20%. 64

4.1 Net ecosystem production obtained by double deconvolution 65

4.2 Two sets of atmospheric CO_2 concentrations reconstructed from ice cores and direct measurements. 67

4.3 Atmospheric data sets $CO_2(a)$ and $CO_2(b)$, respectively 68

4.4 Distribution of available temperature gridpoint data. 69

4.5 Empirical orthogonal functions for the two leading eigenvectors of the global temperature data 70

4.6 The first five principal component time series. 71

4.7 Spline fitted and shifted first two principal component time series. . . 73

4.8 Global mean temperature perturbations. 74

4.9 Global mean temperature perturbations $\Delta T_{0,z}$. 75

4.10 Geographical pattern of mean temperature anomalies averaged over the period from the year 1550 to 1850 76

4.11 Perturbations in terrestrial carbon inventories resulting from simulations C(a,b) 78

4.12 Perturbations in carbon fluxes resulting from simulation C(a) 79

4.13 Terrestrial carbon inventory perturbations resulting from simulations T(0), T(0,10), and T(0,30) 80

4.14 Changes in terrestrial carbon inventory resulting from air temperature perturbations ΔT_0 81

4.15 Perturbations in terrestrial carbon inventories resulting from model runs with air temperature data $\Delta T_{0,z}$ 82

4.16 Perturbations in terrestrial carbon inventories resulting from experiments C(a,b) and C(a,b)T(z), respectively 84

4.17 Perturbations in terrestrial carbon inventories resulting from temperature and CO_2 change simulations 85

4.18 Mean terrestrial carbon storage in latitudinal bands for simulations C(a) and C(a)T(z), respectively 86

Bibliography

Barnola, J. M., M. Anklin, J. Procheron, D. Raynaud, J. Schwander, and B. Stauffer, CO_2 evolution during the last millennium as recored by Antarctic and Greenland ice, *Tellus, Ser. B, 47*, 264–272, 1995.

Collatz, G. J., M. Ribas-Carbo, and J. A. Berry, A coupled photosynthesis – stomatal conductance model for leaves of c_4 plants, *Australian Journal of Plant Physiology, 19*, 519–538, 1992.

de Boor, C., *A Practical Guide to Splines*, Springer, New York, USA, 1978.

DeFries, R. S., and J. R. G. Townshend, NDVI-derived land cover classifications at a global scale, *International Journal of Remote Sensing, 15 (17)*, 3567–3586, 1994.

Enting, I. G., On the use of smoothing splines to filter CO_2 data, *J. Geophys. Res., 92*, 10977–10984, 1987.

Etheridge, D. M., L. P. Steele, R. L. Langenfelds, R. J. Francey, J.-M. Barnola, and V. I. Morgan, Natural and anthropogenic changes in atmospheric CO_2 over the last 1000 years from air in Antarctic ice and firn, *J. Geophys. Res., 101*, 4115–4128, 1996.

FAO, The digitized soil map of the world, *Food and agriculture organization of the United Nations, Tech. Rep.*, 1991.

Farquhar, G. D., S. von Caemmerer, and J. A. Berry, A biochemical model of photosynthetic CO_2 assimilation in leaves of C_3 species, *Planta, 149*, 78–90, 1980.

Foley, J. A., An equilibrium model of the terrestrial carbon budget, *Tellus, 47B*, 310–319, 1995.

Foley, J. A., and I. C. Prentice, An integrated biosphere model of land surface processes, terrestrial carbon balance, and vegetation dynamics, *Global Biogeochemical Cycles, 10(4)*, 603–628, 1996.

Grove, J. M., *The Little Ice Age*, Methuen, New York, USA, 1988.

Haxeltine, A., and I. C. Prentice, BIOME 3: an equilibrium terrestrial biosphere model based on ecophysiological constraints, resource availability and competition among plant functional types, *Global Biogeochem. Cycles, 10*, 693–703, 1996.

Hulme, M., T. Osborn, and T. Johns, Precipitation sensitivity to global warming: Comparison of observations with hadcm2 simulations, *Geophysical Research Letters, 25*, 3379–3382, 1998.

Jackson, R. B., and J. Canadell, A global analysis of root distributions for terrestrial biomes, *Oecologia, 108*, 389–411, 1996.

Johns, T. C., R. E. Carnell, J. F. Crossley, J. M. Gregory, J. F. B. Mitchell, C. A. Senior, S. F. B. Tett, and R. A. Wood, The second Hadley Centre coupled ocean-atmosphere GCM: model description, spinup and validation, *Climate Dynamics, 13*, 103–134, 1997.

Jones, P. D., and R. S. Bradley, Climatic variations over the last 500 years, in *Climate since AD 1500*, edited by R. S. Bradley and P. D. Jones, pp. 649–665, Routledge, New York, USA, 1992.

Joos, F., R. Meyer, M. Bruno, and M. Leuenberger, The variability in the carbon sinks as reconstructed for the last 1000 years, *Geophysical Research Letters, 26*, 1437–1441, 1999.

Keeling, C. D., Atmospheric CO_2 - modern record, south pole, in *Trends '91: A Compendium of Data on Global Change*, edited by T. Boden, D. Kaiser, R. Sepanski, and F. Stoss, pp. 24–27, Carbon Dioxide Inf. Anal. Cent., Oak Ridge, Tenn., 1991.

Keeling, C. D., and T. P. Whorf, Atmospheric CO_2 records from sites in the SIO air sampling network, *Oak Ridge National Laboratory, U.S. Department of Energy, Compendium of data on global change,*, 1999.

Kicklighter, D. W., M. Bruno, S. Doenges, G. Esser, M. Heimann, J. Helfrich, F. Ift, F. Joos, J. Kaduk, G. H. Kohlmaier, A. D. McGuire, J. M. Melillo, R. Meyer, B. Moore III, A. Nadler, I. C. Prentice, W. Sauf, A. L. Schloss, S. Sitch, U. Wittenberg, and G. Wuerth, A first order analysis of the potential role of CO_2 fertilization to affect the global carbon budget: A comparison study of four terrestrial biosphere models, *Tellus, Ser. B, 51*, 343 – 366, 1999.

Leemans, R., and W. Cramer, The IIASA climate database for land areas on a grid with 0.5^o resolution. research report rr -91-18., *International Institute for Applied System Analysis, Tech. Rep.*, 1991.

Lloyd, J., and J. A. Taylor, On the temperature dependence of soil respiration, *Functional Ecology, 8*, 315–323, 1994.

Mann, M. E., R. S. Bradley, and M. K. Hughes, Global-scale temperature patterns and climate forcing over the past six centuries, *Nature, 392*, 779–787, 1998.

McMurtrie, R. E., and Y.-P. Wang, Mathematical models of the photosynthetic response of tree stands to rising CO_2 concentrations and temperatures, *Plant Cell Environ., 16*, 1–13, 1993.

Mitchell, J. F. B., T. C. Johns, J. M. Gregory, and S. F. B. Tett, Climate response to increasing levels of greenhouse gases and sulphate aerosols, *Nature, 376*, 501–504, 1995.

Monteith, J. L., Accomodation between transpiring vegetation and the convective boundary layer, *Journal of Hydrology, 166*, 251–263, 1995.

Neftel, A., H. Friedli, E. Moor, H. Lötscher, H. Oeschger, U. Siegenthaler, and B. Stauffer, Historical CO_2 record from the Siple station ice core, in *Trends '93: A Compendium of Data on Global Change*, edited by T. Boden, D. Kaiser, R. Sepanski, and F. Stoss, pp. 11–14, Carbon Dioxide Inf. Anal. Cent., Oak Ridge, 1994.

Neftel, A., H. Oeschger, J. Schwander, os B. Stauffer, and R. Zumbrunn, Ice core sample measurements give atmospheric CO_2 content during the past 40'000 yr, *Nature, 295*, 220–223, 1982.

Preisendorfer, R. W., *Principal component analysis in meteorology and oceanography*, Elsevier, Amsterdam, 1988.

Siegenthaler, U., H. Friedli, H. Loetscher, E. Moor, A. Neftel, H. Oeschger, and B. Stauffer, Stable-isotope ratios and concentration of CO_2 in air from polar ice cores, *Ann. Glaciol., 10*, 1–6, 1988.

Sitch, S., I. C. Prentice, B. Smith, and J. O. Kaplan, 2000, LPJ — a coupled model of vegetation dynamics and the terrestrial carbon cycle.

Trudinger, C. M., I. G. Enting, R. J. Francey, D. M. Etheridge, and P. J. Rayner, Long-term variability in the global carbon cycle inferred from a high precision CO_2 and δ^{13}c ice core record, *Tellus, Ser. B, 51*, 233 – 248, 1999.

von Storch, H., and A. Navarra, *Analysis of climate variability*, Springer, Hamburg, Germany, 1993.

Voss, R., and U. Mikolajewicz, Long-term climate changes due to increased CO_2 concentration in the coupled atmosphere-ocean general circulation model ECHAM3/LSG, *Max-Planck Institut für Meteorologie, Hamburg, Tech. Rep. 298*, 1999.

Zobler, L., A world soil file for global climate modelling, *NASA, Technical Memorandum,*, 1986.